CONTROLLED LASER CLEANING OF ARTWORKS VIA LOW RESOLUTION PLASMA SPECTROSCOPY AND LINEAR CORRELATION

Cover image: 18th century parchment book cover

Controlled laser cleaning of artworks via low resolution
plasma spectroscopy and linear correlation
Marco Lentjes
ISBN: 978-90-365-2559-6

Printed by Datawyse, Maastricht, the Netherlands

CONTROLLED LASER CLEANING OF ARTWORKS VIA LOW RESOLUTION PLASMA SPECTROSCOPY AND LINEAR CORRELATION

PROEFSCHRIFT

ter verkrijging van
de graad van doctor aan de Universiteit Twente,
op gezag van de rector magnificus,
prof. dr. W.H.M. Zijm,
volgens besluit van het College voor Promoties
in het openbaar te verdedigen
op vrijdag 7 december 2007 om 16.45 uur

door

Marco Lentjes

geboren op 24 maart 1979
te Schiedam

Dit proefschrift is goedgekeurd door de promotoren
Prof. dr. ir. J. Meijer
en
Prof. dr.-ing. K. Dickmann

Contents

Acronyms and symbols ..... **IX**

1 Introduction **1**
1.1 Research definition 2
1.2 Outline of the thesis 3

2 State of the art **5**
2.1 Laser cleaning of artworks 5
2.1.1 Conservation examples *7*
2.1.2 Laser cleaning models *11*
2.1.3 Self limiting processes *13*
2.1.4 Monitoring and controlling laser cleaning *14*
2.2 Laser induced breakdown spectroscopy 17
2.2.1 Instrumentation *18*
2.2.2 Plasma creation and emission *19*
2.3 Linear correlation 21
2.3.1 Linear correlation to compare LIB-spectra *22*
2.3.2 Parameters influencing the magnitude of the correlation coefficient *22*
2.3.3 Rank order and modified correlation method *23*

3 Experimental set-up **25**
3.1 Lasers and optics 25
3.1.1 Excimer Laser *25*
3.1.2 Nd:YAG cleaning laser *28*
3.2 Spectrometers 30

3.2.1 HR2000 ... 30
3.2.2 SpectraPro-500i ... 33
3.3 In-process and post-process sample observation ... 34

4 Layer identification during laser ablation ... 35
4.1 Linear correlation ... 35
4.2 Reference spectrum ... 36
4.3 Delay time ... 37
4.4 Layer identification experiments ... 38
4.4.1 Artificial multi layer arrangement ... 38
4.4.2 Polluted parchment ... 41
4.5 Pre-conditions for process control ... 44
4.6 Conclusions and discussion ... 46

5 Influence of process parameters on the distribution of correlation coefficients ... 47
5.1 Experimental setup and applied method ... 48
5.2 Results and discussion ... 48
5.2.1 Influence of S/N ratio ... 49
5.2.2 Influence of pulse energy ... 50
5.2.3 Influence of delay time ... 51
5.2.4 Influence of integration time ... 52
5.2.5 Influence of the spectrometer resolution ... 54
5.2.6 Influence of object-lens distance deviation ... 54
5.2.7 Influence of irradiation angle ... 56
5.2.8 Influence of crater depth ... 59
5.2.9 Influence of the upper layer thickness ... 60
5.3 Conclusions ... 61

6 Calculation and optimization of sample identification ... 63
6.1 Experimental ... 64
6.2 Single shot distribution ... 65
6.3 Probability of identification ... 66
6.3.1 Gamma distribution ... 67
6.3.2 Normal distribution ... 68
6.4 Identification by averaging ... 68
6.4.1 Gamma distribution ... 69
6.4.2 Normal distribution ... 69

6.5 Results and discussion ... 71
6.5.1 Single shot analysis ... 72
6.5.2 Averaged correlation analysis ... 73
6.5.3 Averaging correlation coefficients or spectra ... 74
6.6 Probability calculation and laser cleaning ... 75
6.6.1 Probability of successful process control ... 75
6.6.2 Probability trees ... 77
6.7 Conclusions ... 78

7 Plasma emission collecting arrangements ... 79
7.1 Beam - collimator - optical fibre couple efficiency ... 80
7.2 Collecting arrangements, excimer laser ... 81
7.2.1 Model ... 81
7.2.2 Numerical calculations ... 83
7.2.3 Experimental validation ... 85
7.3 Collecting arrangements, Nd:YAG cleaning laser ... 89
7.3.1 Model ... 89
7.3.2 Numerical calculations ... 91
7.3.3 Experimental validation ... 93
7.4 Conclusions and discussion ... 96

8 Controlled laser cleaning in practice ... 97
8.1 KrF-excimer system with translation stage ... 97
8.1.1 Experimental set-up ... 98
8.1.2 Software and control ... 100
8.1.3 Results ... 101
8.1.4 Conclusions and side effects ... 115
8.2 Nd:Yag system with articulated arm ... 116
8.2.1 Experimental set-up ... 119
8.2.2 Results and side effects ... 119

9 Conclusions and discussion ... 121

References ... 123

Appendix A: Influence of a linear variation on the linear correlation coefficient ... 131

Appendix B: Refraction indexes and focal lengths ... 135

Summary **137**

Samenvatting **139**

Acknowledgment **141**

About the author **143**

List of publications 144

Acronyms and symbols

Character(s)	Unit	Description
AES		Atomic Emission Spectroscopy
CCD		Charged Coupled Devices
C		Comparing criterion
E	J	Energy
f	m	Focal length
f_c	m	Focal length collimator
ICCD		Intensified Charged Coupled Device
IR		Infra Red
lc	m	Lens collimator distance
LIBS		Laser Induced Breakdown Spectroscopy
ll	m	Lens lens distance
MCP		Multi Channel Plate
NA		Numerical aperture
Ø	m	Diameter
ol	m	Object lens distance
P		Probability
r		Linear correlation coefficient
r_{bc}	m	Beam radius at the collimator entrance
r_c	m	Collimator radius
r_e	m	Radius point source
r_{fc}	m	Beam radius at the fibre entrance
r_{fi}	m	Fibre core radius
r_l	m	Effective lens radius
r_{mod}		Modified correlation coefficient
r_{pc}	m	Radius beam passing through the collimator
r_{pe}	m	Plasma emission half sphere radius
RSD		Relative standard deviation
r_t	m	Radius of the beam passing through both lenses at the first lens

Character(s)	Unit	Description
R_x		Rank of x
S		Estimated standard deviation
S/N		Signal to noise ratio
S^2		Estimated variance
UV		Ultra Violet
x_i	a.u.	Intensity of pixel i in the current spectrum
$\overline{x}$		Mean of all x_i-data
$\underline{x}$		Random variable x
y_i	a.u.	Intensity of pixel i in the reference spectrum
z	m	Coordinate
α		Absorption coefficient
α_{bc}	rad	Angle outer rays at the collimator entrance plane
α_{el}	rad	Angle outer rays passing through the first lens
α_{new}	rad	New starting angle
α_{pc}	rad	Angle outer rays passing through the collimator
β		Scale parameter (Gamma function)
Γ		Gamma function
γ		Shape parameter (Gamma function)
δ	m	Optical absorption length
η		Efficiency
$\eta_{b\text{-}c\text{-}f}$		Beam – collimator – optical fibre couple efficiency
η_c		Collimator couple efficiency
η_{el}		Collecting efficiency of the projection lens
η_{fi}		Optical fibre couple efficiency (area)
η_{NA}		Optical fibre couple efficiency (NA)
η_t		Relative collecting efficiency of the telescope
λ	nm	Wavelength
μ		Expected value
σ		Standard deviation
σ^2		Variance

1 Introduction

The first investigations of the laser as cleaning tool in the conservation of artworks can be ascribed to the 1970s. J. Asmus [1] had successfully tested the applicability of a pulsed ruby laser to remove black encrustation from a white marble sculpture in Venice in 1972 (Fig. 1.1). The selectivity can accredit to the strong absorbing black encrustation and the high reflectivity of the white marble to the applied laser radiation. The following years Asmus and co-workers had spent in studying the applicability of laser radiation to treat different cleaning problems in the conservation of artworks. In spite of the positive results, it took a long time before laser cleaning would be applied in practice. This was mainly due to the fact that at that time: the applicable lasers had a very low repetition rate, the beam delivery was not suitable for practical application, the applicable laser systems were not adapted for continuous usage and the high investment costs of the laser systems suitable for cleaning.

Nowadays, laser cleaning is applied, besides the already established stone cleaning with Nd:YAG laser, in a lot of different conservation fields, e.g. paper, metals, bird feathers, paintings, parchments, glass, etc. That laser cleaning has gained interest in the conservation of artwork can be seen at the contributions of the six LACONA conferences [2-5] (Laser in the Conservation of Artworks) and the amount of publications in scientific journals and conservation magazines.

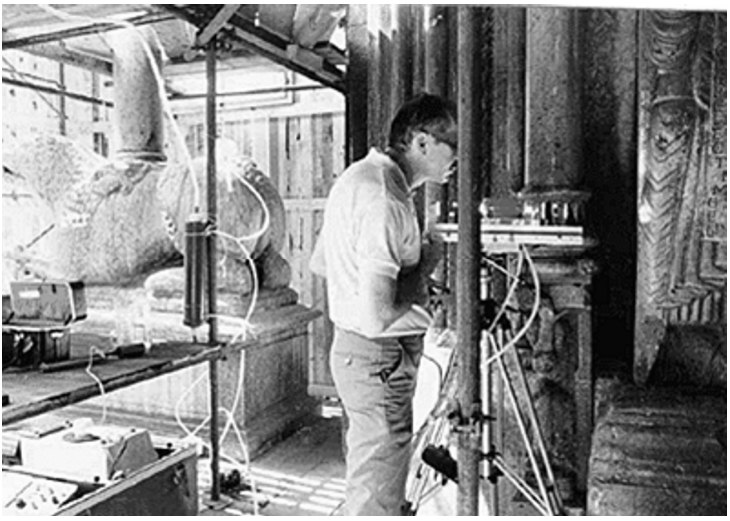

Fig. 1.1 J. Asmus experimenting on the removal of black encrustation from a white marble sculpture with a pulsed ruby laser (Venice, 1972) [source: J. Asmus]

Due to the increasing application of laser cleaning in various conservation fields the diversity of laser cleaned artworks still increases. Whereas, the cleaning process of encrusted marble by Nd:YAG laser is natural selective (when using proper parameters), this is not the case for all polluted artworks. This means that in these cases, on time stopping of the cleaning process is essential to avoid over-cleaning. Without intervention the ablation process just continuous on the surface to be preserved. In general the pollution layers of contaminated artworks are non-uniform. Therefore, the number of laser pulses at a certain position has to be adapted to the pollution degree of this position to ensure an appropriate cleaning of the object.

In this thesis a low cost and easy to handle online monitoring/controlling system has been developed to prevent over-cleaning. This system is based on spectroscopic analysis of the induced plasma emission during laser cleaning.

1.1 Research definition

In the past different sensor systems have been developed to support the restorer during laser cleaning of artworks. As one of these methods, LIBS (Laser Induced Breakdown Spectroscopy) has proved its applicability to monitor laser cleaning processes in praxis. In the European CRAFT project (ENV4-

CT98-0787) the LIBS technique was integrated into a system for controlled laser cleaning of paintings [6, 7].

Developments in spectrometer technology have resulted in rugged fibre optical spectrometer systems (suitable for LIBS experiments) with reduced cost, size and complexity. In combination with proper evaluation procedures these novel systems can be operated by restorers without specific LIBS experience. The research definition for this thesis is described as follows:

Development of a monitoring/controlling system for implementation in laser systems applied for laser cleaning of artworks to avoid over-cleaning. This system should be low cost and easy to handle by restorers without much previous knowledge about plasma spectroscopy.

In case of closed loop laser cleaning of areas with laser systems equipped with a translation stage or scanner, this system should automatically stop the laser cleaning process when the layer to be preserved is locally reached. Subsequently, the translation stage moves the sample to a new position and the cleaning process resumes until the layer to be preserved is reached etc. When working with cleaning lasers with hand guided beam delivery this system should support the restorer during the cleaning process by indicating the local cleaning results on a screen.

1.2 Outline of the thesis

Chapter 2 is about the mechanism thought to be happening during laser cleaning of artworks. An overview is presented of the methods applied to monitor / control laser cleaning processes. Besides, the basics of laser induced breakdown spectroscopy are described and the correlation method is introduced. In chapter 3 the applied set-ups and used equipment is circumscribed. Chapter 4 describes the layer identification process during laser cleaning by correlation analysis and low resolution plasma spectroscopy. Chapter 5 presents a systematic study of the influence of process parameters on the distribution of correlation coefficients. Chapter 6 presents a method for estimating the probability of identification by single shot correlation analysis. A method for calculating the number of spectra to be averaged for a 99.9% probability of identification is evaluated. In chapter 7 basic plasma emission ray

propagation models are introduced to simulate the influence of the collecting optics alignment on the detection efficiency. In chapter 8 automatic laser cleaning and the results of the automatic laser cleaning experiments with a KrF-excimer laser are described. A method for monitoring laser cleaning processes with manual guided beam delivery systems is introduced. The final conclusions and discussions are presented in chapter 9.

2 State of the art

2.1 Laser cleaning of artworks

The laser as cleaning tool in the field of conservation of artworks is still gaining interest and is still in process to be accepted by a larger group of conservation experts. The aim of laser cleaning is to remove an unwanted layer without affecting the original surface. Laser cleaning has the following advantages over conventional chemical or mechanical techniques:

- no other waste material than the removed material
- contact free process
- locally restricted, the laser only works on the irradiation position
- temporary restricted, after the laser pulse there is no further physical reaction
- direct feedback, the result is directly visible after the laser pulse
- direct control, the cleaning process directly stops when the laser is stopped
- selective, in case of a self limiting situation the laser ablation process automatically stops when the unwanted layer is reached.

At the moment the laser systems usually applied for laser cleaning of artworks are pulsed Nd:YAG (natural frequency, frequency doubled and frequency tripled) and KrF-excimer lasers. These lasers exhibit ns pulses and pulse energies up to 1.5 J. For stone cleaning also lasers with µs / ms pulse duration are used. The beam delivery to the objects depends on the laser systems and the objects to be cleaned. Since intense UV-radiation (excimer laser) cannot be transported by an optical fibre these systems are mostly seen with stationary

optics while the object to be cleaned is shifted (with translation stages). The Nd:YAG systems are mostly equipped with an optical fibre or articulated mirror arm. The latter is used for lasers with high pulse peak power. The beam profile of “cleaning” lasers generally demonstrates a tophat profile since a uniform ablation over the spot size is intended. Fig. 2.1 and Fig. 2.2 show two typical Nd:YAG laser systems used for laser cleaning of artworks. The laser in Fig. 2.1 is equipped with an optical fibre and the laser in Fig. 2.2 with an articulated mirror arm to transport the laser radiation to the object.

Fig. 2.1 Laser cleaning system for conservation equipped with an optical fibre. Lambda Scientifica, type Artlight [source: Lambda Scientifica]

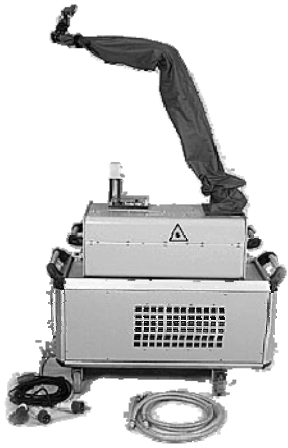

Fig. 2.2 Laser cleaning system for conservation equipped with an articulated mirror arm. Quanta Systems, type Palladio [source: Quante Systems]

A special system was developed for cleaning valuable paintings in the European CRAFT project (ENV4-CT98-0787) [6, 7]. Fig. 2.3 shows a photograph of this system which is designed by the Dutch company Art Innovation in close collaboration with the Fo.R.T.H.-institute. This UV-excimer laser system is equipped with a special designed optical arm in combination with a xy-frame for accurate beam manipulation. It has a working area of 3 m^2.

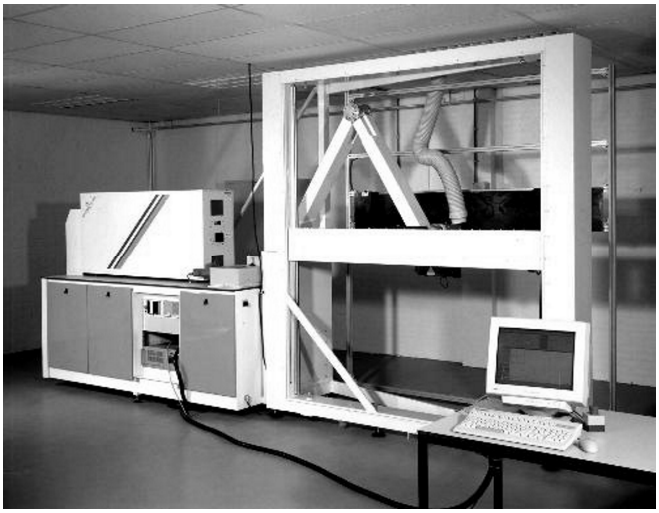

Fig. 2.3 Photograph of the "Advanced workstation for controlled laser cleaning of artworks" [source: Art Innovation]

2.1.1 Conservation examples

Removal of encrustation from stone

Stone cleaning is the most established field of laser cleaning in the conservation of artworks [8-12]. Different commercial stone conservators already own laser systems which they use to remove encrustation from complex or valuable stone objects. Fig. 2.4 shows a partially laser cleaned encrusted sandstone angel.

Fig. 2.4 Angel figure of the Cologne cathedral (Germany). The left half is laser cleaned with a Nd:YAG laser. The right half is untreated [source: Bauhütte Naumburg]

Reduction of varnish on paintings

The Fo.R.T.H.-institute in Greece and the Dutch company Art Innovation are specialist in the field of reduction of varnish on paintings by laser radiation [6, 7, 13, 14]. For example they developed the already described system which is specially designed for the cleaning of paintings. Over the years the varnish layer on paintings becomes less translucence through a chemical reaction (photochemical degradation). Laser cleaning of paintings is based on the selective removal of a well defined layer of varnish. Complete removal of the varnish layer will result in a discoloration of the pigments and therewith to a distortion of the painting [15]. After reduction of the old varnish layer a new varnish layer is applied by a restorer. Fig. 2.5 shows an example of a partially laser cleaned oil painting.

Fig. 2.5 Fraction of an oil painting with aged varnish layer. The left side is laser cleaned with a KrF-excimer laser [source: J. Hildenhagen, LFM]

Reduction of stamp ink on paper

Migration of stamp ink from the verso to the recto side is a well known problem within different art collections (s. Fig. 2.6). This also concerns drawings of the illustrator Jan Heesters within the collection of the Jan Heestershuis museum (Schijndel, Netherlands). In the past these stamps (6 x 2 cm^2), consisting of water solvable blue ink, were placed as an ownership mark on the verso side of the drawings.

When the applied pulse energy density is lower than the paper modification threshold, stamp ink can be reduced by green (532 nm) laser radiation without affecting the paper fibres [16-18]. Paper reflects, transmits and absorbs laser radiation at the wavelength 532 nm. Hence, it is not only possible to remove stamp ink from the paper surface but also to remove stamp ink between the paper fibres. Complete removal of the stamps without damaging the paper is not possible, since a percentage of the stamp ink is deeply soaked into the paper fibres. Nevertheless, a reduction of the stamp ink results in a decrease of the translucence of the stamp and reduces the migration into the paper.

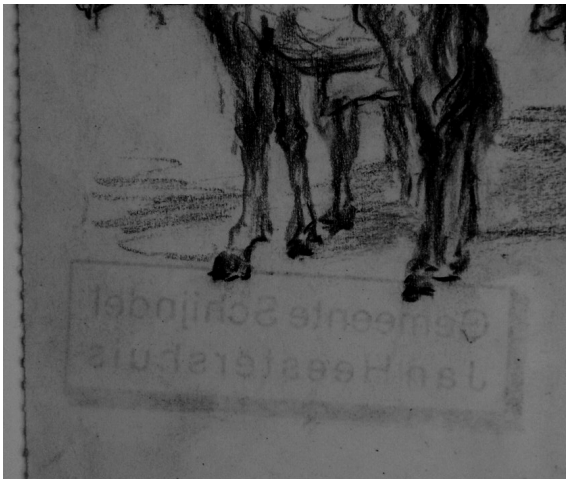

Fig. 2.6 Stamp ink migrated from the verso to the recto side on a drawing of the illustrator Jan Heesters (1893-1982, NL)

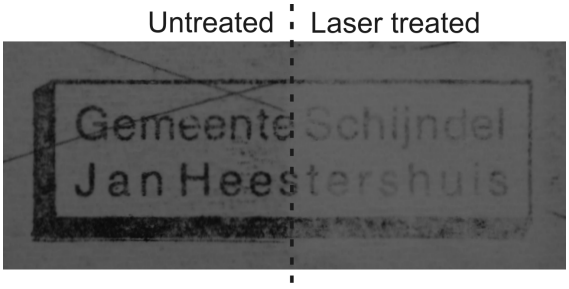

Fig. 2.7 Stamp ink before and after laser treatment, a reduction of the ink is clearly visible

The stamp ink on the verso side of several artworks on paper of the illustrator Jan Heesters was successfully reduced. In individual cases the stamp ink was even completely not observable at the recto side after laser treatment. Fig. 2.7 shows a photo of the typical stamp placed on the verso side of the drawings, the right half is treated with laser radiation. A clear reduction of the stamp ink is observable.

Metallic objects

Copper and bronze artworks or archaeological iron work are often covered by corrosion layers. These layers are conventionally removed by chemical agents. Laser cleaning showed to be a good environmentally friendly alternative [19, 20]. Even the usability of femtosecond lasers for the laser cleaning of metallic antique artworks is a research topic on this moment [21]. Fig. 2.8 shows a partially laser cleaned bronze pommel of an iron sword.

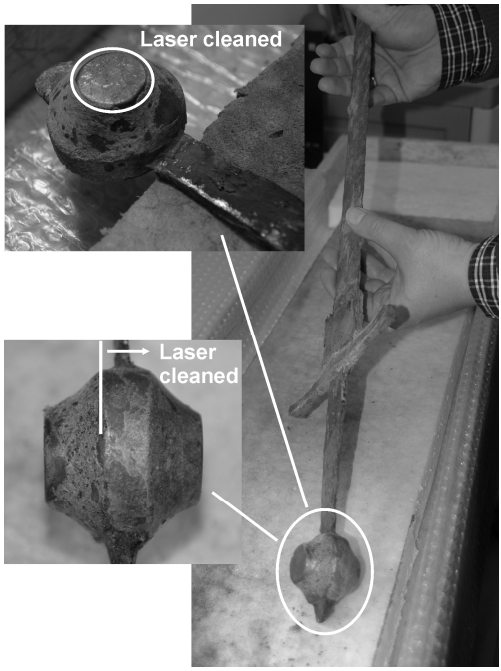

Fig. 2.8 Iron sword of the high middle ages, this sword was found in a river. The bronze encrusted pommel of the sword is laser cleaned by a Nd:YAG cleaning laser [source: J. Hildenhagen, LFM]

2.1.2 Laser cleaning models

When a laser pulse with energy E meets a material the pulse energy is partly reflected (R), transmitted (T) and absorbed (A). The ratio between R, T and A depends on the laser and material parameters. The law of energy says:

$$R + T + A = 1 \tag{2.1}$$

For opaque materials like metals $T = 0$. In absorbing materials the pulse energy (E_0) propagating into the material decreases with distance z according to the Beer-Lambert law:

$$E(z) = E_0 e^{-\alpha z} \tag{2.2}$$

where α is the absorption coefficient of the material. The distance over which the incident energy is reduced by a factor $1/e$ is defined as the optical absorption length; $\delta = 1/\alpha$. The optical penetration depth for visible and near infrared wavelengths is typically several nanometers for metals, 10 - 100 µm for homogeneous black crusts or brown patination and several millimeters for calcite or gypsum [22].

The laser radiation is absorbed in a layer with thickness δ by interactions with free electrons, bound electrons, the material lattice or any combination of these. Which mechanism occurs, depends on the physical characteristics of the absorption layer and of the electromagnetic radiation. The electrons absorb (multiple) photons by inverse bremsstrahlung, whereby the free electrons gain kinetic energy and bound electrons are excited to higher energy states. The lattice can absorb photons with the radiation frequency equal to the natural frequencies of the lattice. The energetic and excited electrons transfer their energy to the lattice by collisions. Due to the fact that the mean time between collisions is about 10^{-13} s it can be assumed that the absorbed energy is directly converted into heat in the absorption volume (except for femtosecond lasers) [23].

In case of high energetic photons the energy of one photon can directly break covalent chemical bonds. This results in a volume explosion and material ablation attended with minor heat formation. This is called a “cold ablation”. Table 2.1 shows different lasers with corresponding photon energies and the dissociation energies of several chemical bonds.

The ablating mechanisms as involved in the laser cleaning of artworks are complex processes since multiple layers are concerned and the pollution layer is usually inhomogeneous. The following mechanisms are thought to be found

during ablating of pollution layers with pulsed lasers [8, 22, 24, 25], when the energy is transferred into heat as described above:

- Evaporation: at energy densities of 10 - 100 J/cm^2 and pulse durations of 200 - 500 µs the ablation mechanism is evaporation of the irradiated material. At lower energy densities 1 - 20 J/cm^2 but shorter pulse lengths 20 - 100 µs the ablation process is thought to be fast evaporation.
- Spallation: the ablation mechanism with short pulses of 5 - 100 ns and energy densities of 0.1 - 4 J/cm^2 is fast evaporation in combination with spallation. With these laser parameters a plasma is generated at the irradiated surface (see section 2.2.2). The high plasma pressure (1 - 100 kbar) results in a shockwave leading to high compressing stresses on the surface. After the laser pulse the surface relaxes. It results in a thin surface layer (1 - 100 µm) to be removed (spallation).
- Thermal expansion: below the evaporation threshold, ablation can occur due to a rapid thermal expansion of the heated material layer or particles. If the generated thermal forces are high enough to overcome cohesion or adhesion forces, the heated material layer or particles are ejected away from the surface.

Table 2.1 Photon energies from different laser sources and required dissociation energies for several chemical bonds (source: J. Meijer [26])

Laser	Wavelength [nm]	Photon energy [eV]	Chemical bond	Bond energy [eV]
CO_2	10600	0.12		
Nd:YAG	1064	1.16		
XeF	351	3.53	Si–Si, Cl–Cl	1.8-3
XeCl	308	4.03	C–N, C–C	3-3.5
Nd:YAG 4ω	266	4.65		
KrF	248	5.00	C–H, O–H	4.5-4.9
KrCl	222	5.50		
ArF	193	6.42		
F_2	157	7.43	C=C	7

2.1.3 Self limiting processes

In the 1960s, the idea of the “laser eraser” had been proposed by Arthur Schawlow which resulted in a patent [8, 24]. The laser eraser prototype (small ruby laser) was invented to remove black ink from white paper without affecting the paper. This worked while, the black ink absorbed the laser radiation and the white paper reflected the laser radiation (Fig. 2.9). J. Asmus and co-workers [1] demonstrated in Venice (1972) that this principle also works when ablating black encrustation from white marble. This means that the surface to be preserved was not damaged by the laser irradiation, a natural selective procedure, in this field called: “self limiting process”.

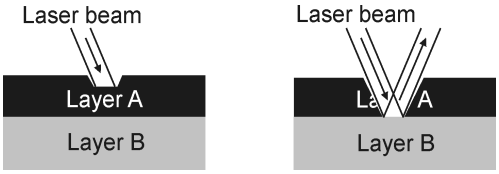

Fig. 2.9 The laser beam is absorbed in layer A and reflected at the transition layer B

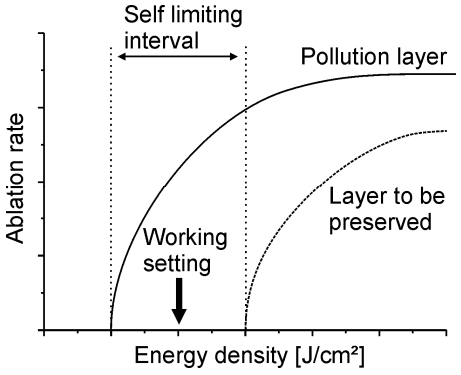

Fig. 2.10 Self limiting process, the ablation threshold of the layer to be preserved is higher than the ablation threshold of the unwanted layer

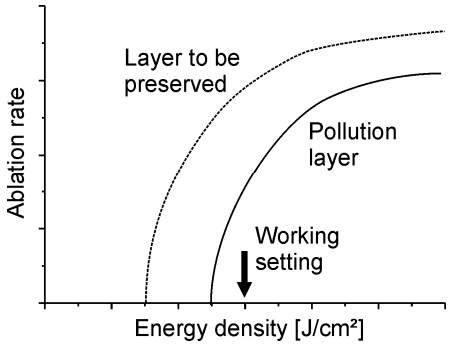

Fig. 2.11 Non self limiting process, the ablation threshold of the layer to be preserved is lower than the ablation threshold of the unwanted layer

A self limiting interval also exists when the ablation threshold of the unwanted layer is lower than the ablation threshold of the layer to be preserved, see Fig. 2.10. For a self limiting process the working setting must be chosen in between.

In case the ablation threshold of the unwanted layer is higher (Fig. 2.11) than the ablation threshold of the layer to be preserved, there exists no self limiting interval.

2.1.4 Monitoring and controlling laser cleaning

Through the wide variation of pollution on sensitive artworks laser cleaning is not self limiting in all cases. Since the pollution layer on artworks generally exhibit a non-uniform thickness, local over-cleaning may occur if the complete object is cleaned with the same laser irradiation parameters (in the case of non self limiting processes). To avoid over-cleaning the number of laser pulses at a certain position has to be adapted to the pollution degree at this position. Fig. 2.12 shows different methods which have been invented to avoid over-cleaning during laser cleaning of artworks. Not every method can be used for every object to be cleaned.

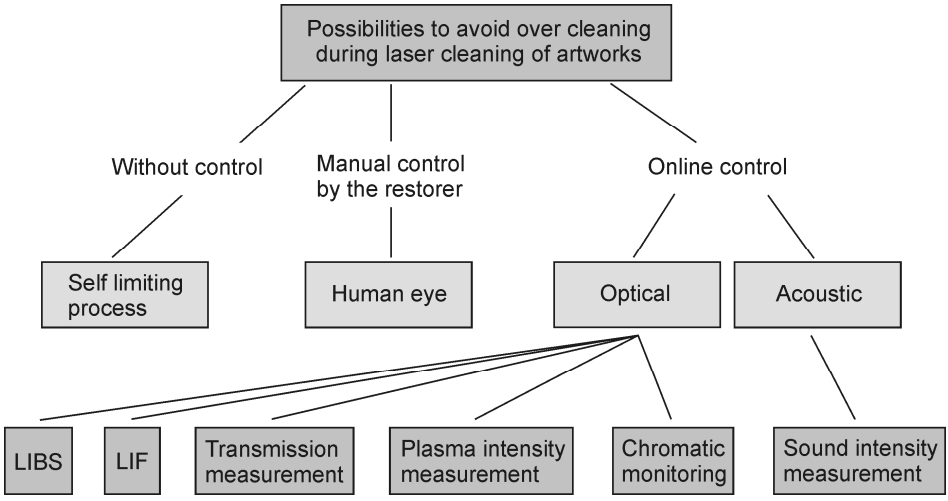

Fig. 2.12 Diagram with applied and researched techniques to monitor and control laser cleaning process of artworks

The existing methods are:

- Self limiting process: see section 2.1.3 Self limiting processes.
- Human eye: at most practical laser cleaning projects the ablation process is manually controlled by the restorers. They observe the laser cleaning

process through a laser safety goggle and stop the laser manually if the pollution is removed.

- LIBS: laser induced breakdown spectroscopy has been successfully applied to control different kind of laser cleaning processes, e.g. stone, glass [27-29] and paintings [6, 7]. Spectroscopic analysis of the plasma emission induced during laser cleaning is used to identify the ablated material in process. The emission spectrum is characteristic for the ablated material / layer and can be used to identify the qualitative and quantitative elemental configuration of the ablated material. This will be explained in more detail in section: 2.2 Laser induced breakdown spectroscopy.
- LIF: laser induced fluorescence has been applied to identify the ablation layer in process. The induced fluorescence emission is also material specific. However, it can not be used to identify the elemental constituents of the material. A disadvantage is that a second laser is generally used for exciting. [29, 30]
- Transmission measurement: in case of cleaning transparent materials, the process can be monitored by measuring the transmitted laser radiation. This method has been applied with and without additional light source [31].
- Plasma intensity measurement: monitoring the plasma emission intensity by a simple fast photodiode (wavelength integrated) in combination with an oscilloscope or DAQ-card is in some cases sufficient to monitor [32] or to control [33] the laser cleaning process. This method requires a significant difference between the plasma intensity belonging to the unwanted layer and the layer to be preserved.
- Chromatic monitoring: angular irradiating of the processing area with a polychromatic light source and measuring the reflected radiation with RGB-sensors has been applied to obtain the irradiated layer in-process [34, 35]. For this method is assumed that the chromatic reflectance varies per layer.
- Sound intensity measurement: acoustic monitoring of the snapping sound during laser cleaning, induced by rapid ejection of particles and expansion of the plasma plume has been used to monitor laser cleaning processes [34, 36]. M. Jankowska and G. Śliwiński [36] found that the amplitude of the snapping sound was proportional to the crust thickness of encrusted sandstone.

- Within the European project “Paper Restoration using Laser Technology” (PARELA, EVK4-CT-2000-30002) [17] a system, which can locally treat flat paper objects has been developed. The objects are photographed and subsequently the areas to be treated are indicated by digital image processing in this photo. By means of a scanner optic only the predefined areas are laser treated. Fig. 2.13 shows the set-up of this system. An example is given in Fig. 2.14: the left photograph shows the object before laser cleaning, whilst the image in the middle shows the mask of the area to be treated, the right photograph shows the object after partial laser cleaning.

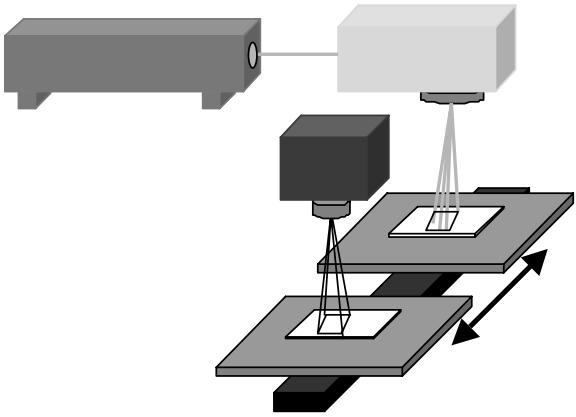

Fig. 2.13 Diagram of the set-up for locally treating flat paper objects, consisting of a laser (532 nm) with scanning head and a digital camera (source: [17])

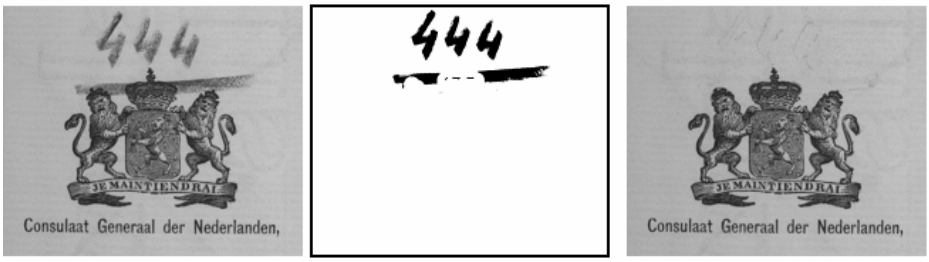

Fig. 2.14 Selective removal of chalk from paper, (left) object before cleaning, (middle) digital mask, (right) object after partial laser cleaning (source: [17])

2.2 Laser induced breakdown spectroscopy

Laser induced breakdown spectroscopy (LIBS) is an atomic emission spectroscopy (AES) method generally applied for qualitative and also quantitative element analysis. This technique is used in various fields of application and is still gaining interest which can be seen in the growing amount of articles, reviews [37-46] and books [47-49] about this technique. The advantage of the LIBS-technique over other element identification techniques is the possibility of analyzing all types of materials in every aggregate condition without the need of sample preparation. In general an intense pulsed laser beam is focused onto the sample and heats and evaporates a small volume of this target resulting in a transient plasma above the irradiated area. The spectral composition of the light emitted by this plasma plume depends on the elemental composition of the ablated material. The emitted plasma light is analyzed by a spectrometer.

LIBS as a diagnostic tool has found a lot of practical applications from lateral and in-depth elemental analysis [50] up to the detection of biological aerosols [51, 52]. LIBS is also used in process control e.g. on-line sorting [53] and controlling the composition of molten alloys [54, 55].

In cultural heritage LIBS is mostly applied as a diagnostic tool to identify the elemental configuration (qualitative and quantitative), in and without combination of laser cleaning [44]. Examples are: the identification of pigments by elemental configuration [56-59], contamination analysis of historical paper documents [60], surface and in-depth element analysis of encrusted historic stones [61-63], stratigraphic analysis of corroded glasses [64], chronocultural sorting of archaeological bronze object by their metal content [65] and recognition of archeological materials underwater [66].

A different approach is to consider the LIB-spectra of different materials as unique fingerprints with differences in spectrum and intensity. Gornushkin and coworkers [67-70] applied this method in combination with linear/rank correlation to identify plastic, solid, particulate and archaeological materials. Jurado-López and Luque de Castro [71] applied rank correlation for the identification of alloys used in jewelry manufacturing. Both compared the spectrum of the “unknown” sample with a library of reference spectra and identified the sample by the weight of correlation (see 2.3 Linear correlation). The correlation method can be applied for sorting and identifying of “unknown”

samples on the condition that a reference spectrum of the samples is present in the library. Reference spectra are formed by averaging multiple spectra or just by a single significant spectrum of the sample. An advantage of the correlation method is that there is no need of spectral emission tables for identifying.

2.2.1 Instrumentation

The set-up for LIBS experiments generally exist of a pulsed laser for inducing a plasma, plasma emission collecting optics, a spectrometer for analyzing the collected plasma emission and timing electronics for adjusting the delay between laser pulse and acquiring the plasma emission, see Fig. 2.15.

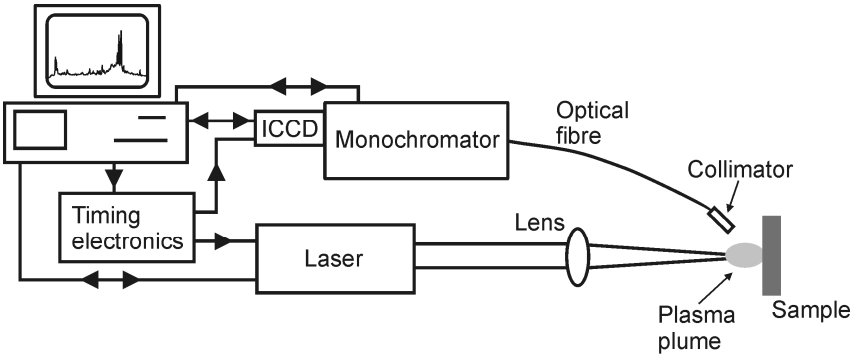

Fig. 2.15 Basic LIBS set-up

Depending on the application different monochromator and detector combinations are applied as spectrometer system for LIBS experiments. However, the most common used optical set-up for LIBS measurements is the Czerny-Turner monochromator set-up in combination with an ICCD [38]. During the last years the Echelle-spectrometer is also gaining interest in the LIBS field, since it can measure a wide bandwidth at high resolution [38, 72]. This allows complete recording of the emission spectrum at high resolution in a single shot. The disadvantage of the Echelle-system when measuring higher intensities is the blooming effect. This results in ghost lines in the acquired spectra [72]. Recent developments in spectrometer technology have resulted in rugged small fibre optical spectrometers with reduced cost, size and complexity which can be used for low(er) resolution LIBS measurements [73-76].

2.2.2 Plasma creation and emission

When an intense laser pulse is focused onto a material a part of the energy is transferred into heat. This results in evaporation of material and a vapor above the surface early during the laser pulse. The free electrons in this vapor absorb photons during the rest of the laser pulse by inverse bremsstrahlung. By collisions, photon emission and inverse bremsstrahlung energy is exchanged in this vapor causing an avalanche reaction. The vapor fractional ionizes and the plasma state is achieved.

Plasma is a gas mixture of neutral atoms, ions and free electrons with continuous energy exchange. Laser induced plasmas are short-time cold plasmas with a low ionization ratio (< 10%). Plasmas are overall electrically neutral. However, there is no homogeneous distribution of charge carriers. Another property of plasma is the intense emission of electromagnetic radiation with wavelengths in the interval UV - IR.

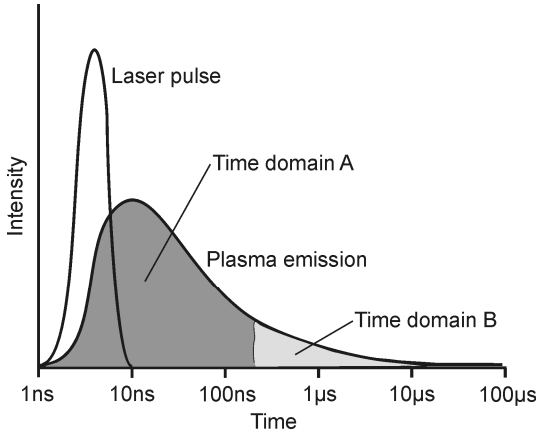

Fig. 2.16 Typical temporal history of laser induced plasma emission. The time domain A is characterized by a broadband white light emission and time domain B is characterized by discrete elemental line emission

The observed plasma emission is the sum of the continuum emission and the spectral line emission of the elements in the plasma plume. The continuum/line emission ratio depends on the observation window. Fig. 2.16 shows the typical temporal history of plasma emission induced by a short pulse laser.

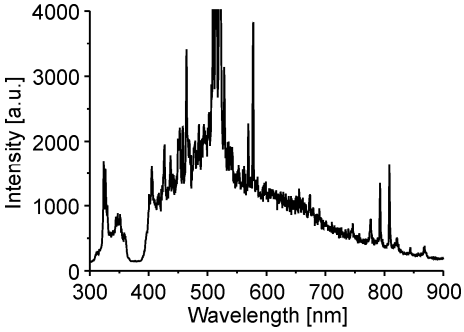

Fig. 2.17 LIB-spectrum of 99.9% copper, There was no delay between laser pulse and plasma emission acquiring (time domain A)

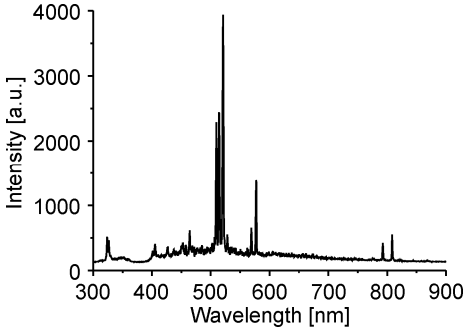

Fig. 2.18 LIB-spectrum of 99.9% copper, The delay between laser pulse and plasma emission acquiring was 1.5 µs (time domain B)

The first time domain (A; typical duration of some hundreds of nanoseconds) is dominated by continuous broadband white light emission. This continuum emission is primarily due to bremsstrahlung of free electrons and recombination emission from electron-ion recombination in the cooling plasma. Some strong elemental lines arise above the strong continuum; see Fig. 2.17.

The second time domain (B; typical duration of some microseconds) is characterized by discrete elemental line emission. The observed spectrum mainly corresponds to the elemental constitution of the plume; see Fig. 2.18. The line intensities are proportional to the concentration of the elements in the plume under the condition of no self-absorption.

Since the continuum decays faster than the line emission, the second time domain (B) is mostly used in conventional LIBS experiments (qualitative and quantitative). In this time domain the elemental line emission can be discriminated from the continuum emission.

The elemental line widths, profiles and line shifts in laser induced plasmas mainly depend on the plasma temperature and the electron density. The dominant broadening mechanisms are: Doppler broadening, natural line broadening and Stark broadening. Natural broadening can be neglected since it can not be observed with the spectrometers normally applied for LIBS experiments.

2.3 Linear correlation

The linear correlation coefficient r [77, 78] introduced by Karl Pearson in 1895 is a measure for the linear relation between paired x,y-values and ranges from -1 to 1. A value of $r = 1$ represents a correlation of 100%, $r = 0$ means no linear correlation and $r = -1$ a fully negative correlation. The Pearson's linear correlation coefficient is given by:

$$r = \frac{\sum_{i=1}^{m}(x_i - \bar{x})(y_i - \bar{y})}{\sqrt{\sum_{i=1}^{m}(x_i - \bar{x})^2}\sqrt{\sum_{i=1}^{m}(y_i - \bar{y})^2}} \tag{2.3}$$

where $\bar{x}$ is the mean of all x_i-data and $\bar{y}$ the mean of all y_i-data.

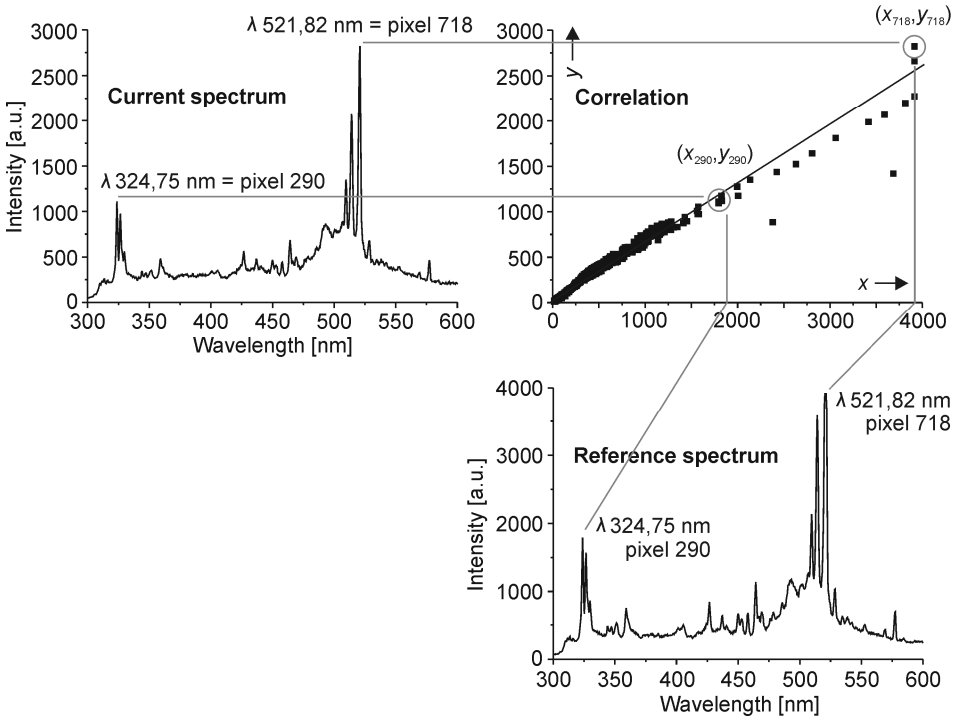

Fig. 2.19 Graphical visualization of the correlation between a current spectrum and a reference spectrum. The intensities of the same pixel (i) in the reference spectrum (x_i) and the current spectrum (y_i) generate the single (x_i,y_i)-pairs in the scatter diagram. Visible is the high correlation between both spectra

2.3.1 Linear correlation to compare LIB-spectra

In this work the linear correlation coefficient was applied to compare the spectrum of the irradiated material in process with a reference spectrum. The magnitude of *r* is used as a measure for the similarity of spectra. In case of correlating two “very”-identical spectra the correlation coefficient will approximate the value of 1.

The intensity on the CCD-pixels measured during recording the reference spectrum forms the *x* data set while the *y* data set is given by the spectrum of the irradiated material which is investigated, Fig. 2.19. A data set consists of *m* points representing the number of pixels of the spectrometer CCD-array, thus $i = 1..2048$ for the Ocean Optics HR2000. Each pixel represents a x_i-value (intensity of the reference spectrum) and respectively a y_i-value (current spectrum).

2.3.2 Parameters influencing the magnitude of the correlation coefficient

There are many different parameters which influence the magnitude of the correlation coefficient when correlating spectra, for example:

- Number of intensity variations (number of wavelengths that have a different intensity in the current spectrum than in the reference spectrum)
- Amplitude of the intensity variations
- Size of the data set (number of pixels used for correlation)
- Variance of the data set
- Combination of the parameters above

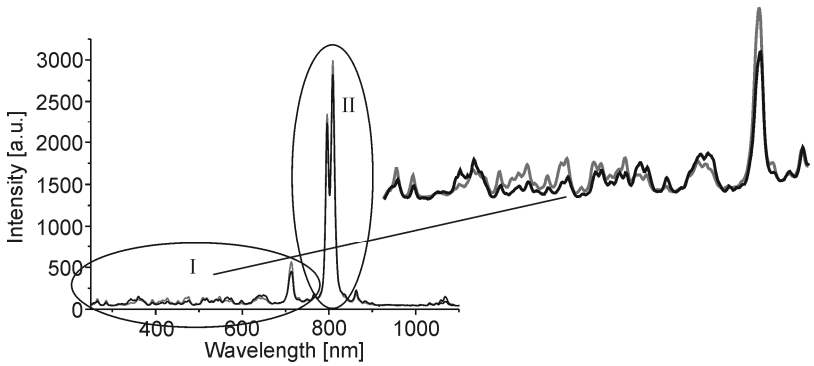

Fig. 2.20 Two very similar spectra with intense peaks (II), the most significant difference between both spectra is in area I

When correlating two spectra the prementioned parameters influence the magnitude of the correlation coefficient as follows:

- The correlation coefficient decreases with increasing number of variations.
- With increasing amplitude of variation, *r* decreases.
- The influence of a variation is smaller for a larger data set.
- The variance of a data set has a significant influence on the impact of a variation on the correlation coefficient. With increasing variance the influence of a variation decreases.

The spectra in Fig. 2.20 have a high intensity variance caused by the peaks in area II. Despite the variations in area I the correlation coefficient tends to 1. Thereby discriminating between both spectra by linear correlation analysis is difficult. In this case correlating just part I of the spectrum decreases the correlation coefficient and therewith the feasibility to distinguish between the spectra increases.

The linear correlation coefficient is not sensitive for a multiplication of all x_i-values with a constant factor α or adding a constant A to all x_i-values, $\left(X_i = \alpha \cdot x_i + A\right)$. This means that an offset (A) or an increase of the intensity of all pixels with a factor (α) will not influence the correlation coefficient r (see appendix A).

2.3.3 Rank order and modified correlation method

In literature the use of the rank order correlation coefficient and a modified correlation method to compare LIB-spectra is presented. Gornushkin et al. and Anzano et al. [67-70] applied linear and rank order correlation to identify plastic, solid, particulate and archaeological materials. Overall they obtained no significant difference between the results of both methods. Jurado-López and Luque de Castro [71] used rank order correlation for the identification of alloys used in the jewelry manufacturing. In statistic the rank order correlation coefficient is often used to correlate ordinal variables. In contrast with the linear correlation coefficient not the values of the variables but their ranks (R) are used for the calculation. A disadvantage of this method is the higher calculation effort since the rank of every value has to be obtained. The equation of the rank order correlation coefficient is the same as for the linear correlation coefficient:

$$r_{\text{rank}} = \frac{\sum_{i=1}^{m}\left(Rx_i - \bar{R}x\right)\left(Ry_i - \bar{R}y\right)}{\sqrt{\sum_{i=1}^{m}\left(Rx_i - \bar{R}x\right)^2}\sqrt{\sum_{i=1}^{m}\left(Ry_i - \bar{R}y\right)^2}} \tag{2.4}$$

In statistical books often the Spearman's rank order correlation coefficient equation can be found:

$$r_{\text{rank}} = 1 - \frac{6\sum_{i=1}^{m} d_i^2}{m^3 - m} \tag{2.5}$$

where $d_i = Rx_i - Ry_i$. This equation can be used when every x_i and y_i value is different and thus each rank exists only once per dataset which is not the case with LIB-spectra.

Tong et al. [79] modified the equation of the linear correlation coefficient to increase the calculation efficiency during real time control of ultra fast laser micromachining by laser induced breakdown spectroscopy. They modified the equation of the linear correlation coefficient by removing the averages of the data sets out of equation (2.3) and obtained the following equation:

$$r_{\text{mod}} = \frac{\sum_{i=1}^{m} x_i y_i}{\sqrt{\sum_{i=1}^{m} x_i^2}\sqrt{\sum_{i=1}^{m} y_i^2}} \tag{2.6}$$

The disadvantage of the modified correlation method is the sensitiveness for adding a constant *A* to all values of one data set and its lower sensitiveness for variations between data sets.

In this thesis the Pearson's linear correlation coefficient is applied. It has the best characteristics to compare spectra during laser cleaning (Table 2.2).

Table 2.2 Summary of the characteristics of the introduced correlation methods to compare LIB-spectra

Correlation method	Distinguishability between various spectra	Computing effort	Sensitiveness for a linear variation
r (Pearson)	+ +	+	+ +
r_{rank}	+ +	– –	+ +
r_{mod}	+	+ +	– –

3 Experimental set-up

3.1 Lasers and optics

Two generally applied optical set-ups for laser cleaning of artworks were used, in order to demonstrate the capability and ease of integration of the developed method in typical laser cleaning set-ups. The main differences between the set-ups regarding to the key objectives of this thesis are the beam delivery and the beam/sample manipulation. It must be pointed out that the difference in laser wavelength was no research objective of this study.

3.1.1 Excimer Laser

The applied KrF-excimer laser system is equipped with a computer controlled translation stage enabling controlled movements of the sample with respect to the stationary laser beam, see Table 3.1. The characteristics of the excimer laser are given in Table 3.2. Fig. 3.1 shows the used typical excimer laser based mask illumination and imaging optical set-up. A photograph of the applied excimer set-up is given in Fig. 3.2. The laser fluence could be externally attenuated by means of an angle dependent attenuator. The Kepler telescope compressed the raw rectangle excimer beam (30 x 15 mm^2) to an almost quadratic beam at the mask plane (15 x 15 mm^2). The applied quadratic mask (6 x 6 mm^2) was generally projected by an f = 120.7 mm lens to a 1.5 x 1.5 mm^2 spot onto the surface of the samples.

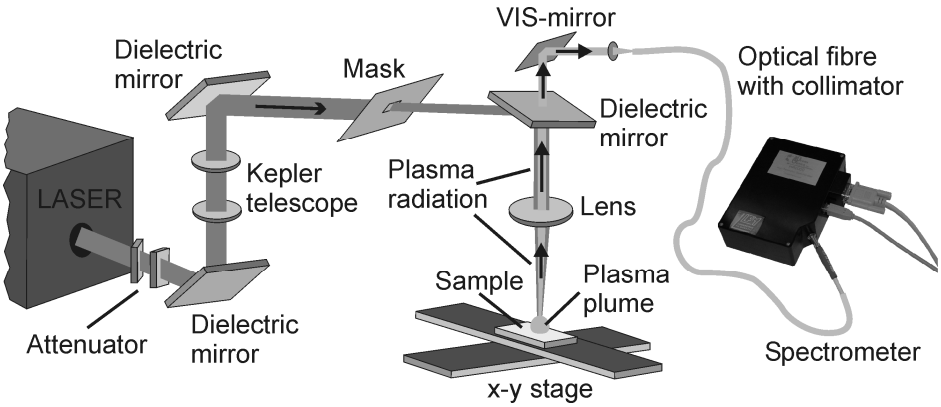

Fig. 3.1 Drawing of the excimer laser optical set-up with implemented optical fibre and collimator

Fig. 3.2 Photograph of the excimer set-up

This mask was chosen since it had the dimensions of the quasi homogenous part of the compressed excimer laser beam. Fig. 3.3 shows the measured beam profile at the imaging plane.

The optical fibre with collimator for collecting the plasma emission was placed behind the last dielectric mirror (on-axis plasma emission collection). This has the advantage in praxis that the collimator must not be aligned anew for samples of different heights.

Table 3.1 Characteristics of the translation stage

Type	IEF Werner PROPAC
Coding	CNC
Traveling range	800 x 800 mm^2
Resolution	7 µm
Digital I/O	20 channels

Table 3.2 Characteristics of the excimer laser

Type	Lambda Physics LPX 305i
Wavelength	248 nm (KrF)
Repetition rate	1-50 Hz
Max. pulse energy	1100 mJ
Pulse duration	20-40 ns

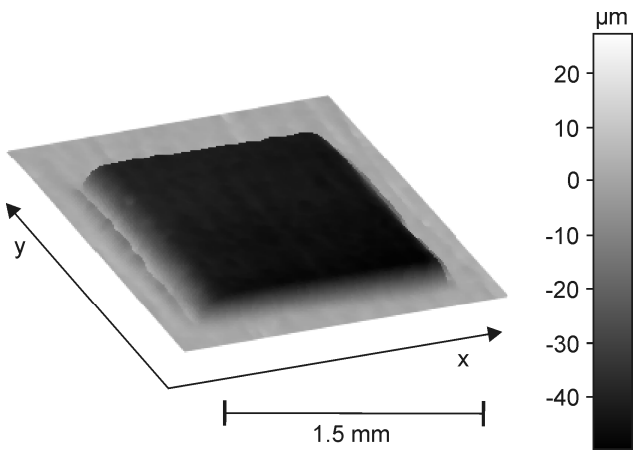

Fig. 3.3 Measured excimer beam profile at the imaging plane. This was gained by a topography measurement of irradiated PVC. (80 pulses, pulse energy 25 mJ, spot size 1.5 x 1.5 mm^2)

3.1.2 Nd:YAG cleaning laser

The second laser system from Thales, see Table 3.3, is equipped with an articulated mirror arm enabling manual spatial manipulation of the laser beam (Fig. 3.4). The laser system is a flash lamp pumped Q-switched Nd:YAG laser based on oscillator/amplifier principle with the possibility of frequency doubling, tripling and quadrupling. In this thesis only the first harmonic was applied. Fig. 3.5 shows the hand piece of the articulated arm with collimator and optical fibre integrated in the last mirror holder (on-axis plasma emission collection). The hand piece embodies a telescope consisting of a positive lens (f = 102.3 mm) sequenced by a negative lens (f = -101.0 mm). The distance between both lenses can be varied in order to adjust the working spot diameter and consequently the energy density on the object surface is adjusted. Fig. 3.6 shows a cross section of the mirror holder especially constructed for the in-process plasma emission measurements. The beam profile is shown in Fig. 3.7.

Fig. 3.4 Removal of an encrustation layer on sandstone with the Nd:YAG cleaning laser

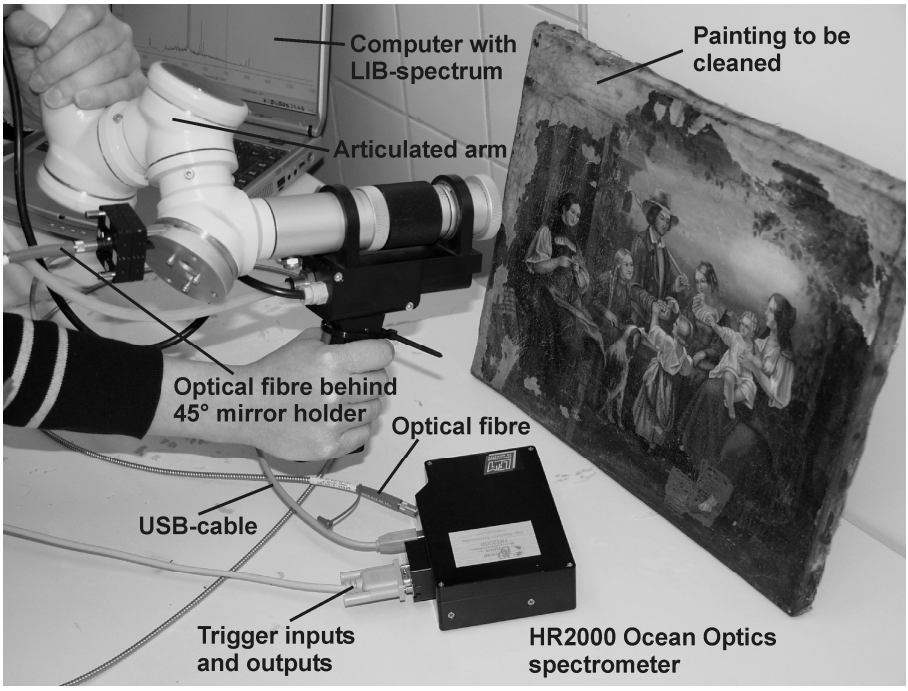

Fig. 3.5 Hand piece of the Nd:YAG cleaning laser with collimator and optical fibre implemented in the last mirror holder

Table 3.3 Characteristics of the Nd:YAG laser

Type	Thales Saga 220/10
Wavelengths	1064 nm (Nd:YAG) 2ω, 532 nm 3ω, 355 nm 4ω, 266 nm
Repetition rate	1-10 Hz
Max. pulse energy	1500 mJ @ 1064 nm
Pulse duration	10 ns

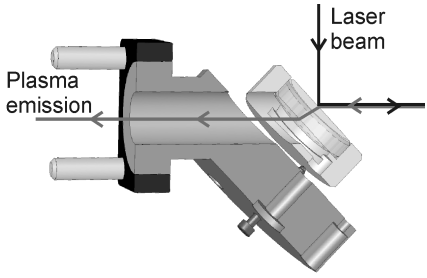

Fig. 3.6 Cross section of the last mirror holder

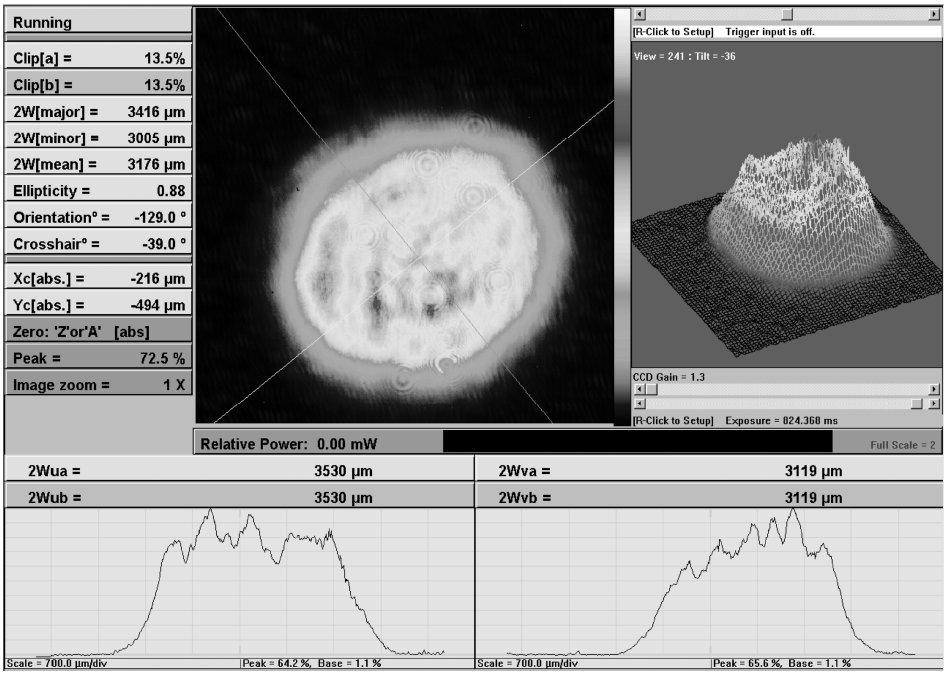

Fig. 3.7 Unmagnified beam profile of the Nd:YAG cleaning laser behind the telescope, obtained by a WinCam D beam analyser

3.2 Spectrometers

Two different spectrometers have been applied. These spectrometers differ in spectral resolution, complexity and construction. The main part of the research is based on the HR2000.

3.2.1 HR2000

The HR2000 spectrometer system is a user configured miniature fibre optic spectrometer from Ocean Optics. Fig. 3.9 shows the inside of the HR2000 which is build with a symmetrical crossed Czerny-Turner optical design. Table 3.5 shows the description of the parts and the chosen configuration.

The applied spectrometer is “LIBS-Upgraded” which enables the use of the LIBS software from Ocean Optics and triggering of the laser. The delay time between laser pulse and acquire plasma radiation is set in 500 ns steps by this software. For controlled laser cleaning an in LabView 7.1 written program

(described in section 8.1.2) in combination with a DAQ-card was used. Its on-board counters enable triggering of the process. The characteristics of the DAQ-card are given in Table 3.4.

The exposure time of the electronic “shutter” is factory-set on 2 ms. A 2 m long Ø = 600 µm optical fibre in combination with an *f* = 10 mm Ø = 5 mm collimator was applied to collect the plasma radiation. The groove density (300 grooves/mm) and the entrance aperture of 25 µm result in a spectral range of 200 to 1100 nm with a resolution of 2 nm. The wavelength dependent sensitivity of the Sony ILX511 linear CCD array, 2048 pixels A/D resolution 12 bit, is shown in Fig. 3.8.

Table 3.4 Characteristics of the multifunction DAQ-PCI device

Type	National Instruments PCI-6221
Analog inputs	16
Analog outputs	2
Digital I/O	24 channels
Counters	2 x 80 Mhz
Terminal block	BNC-2110

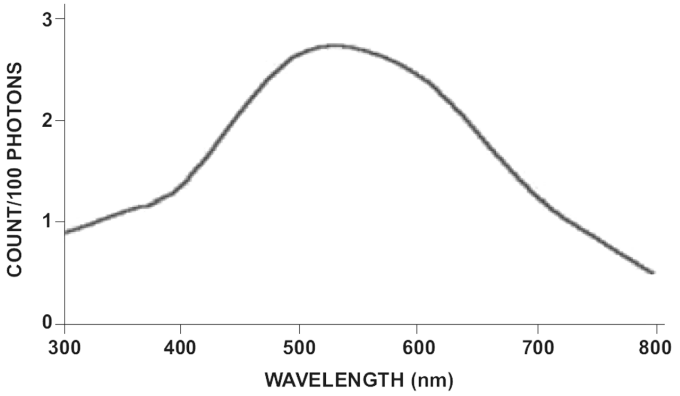

Fig. 3.8 CCD detector sensitivity versus wavelength [Source: OceanOptics]

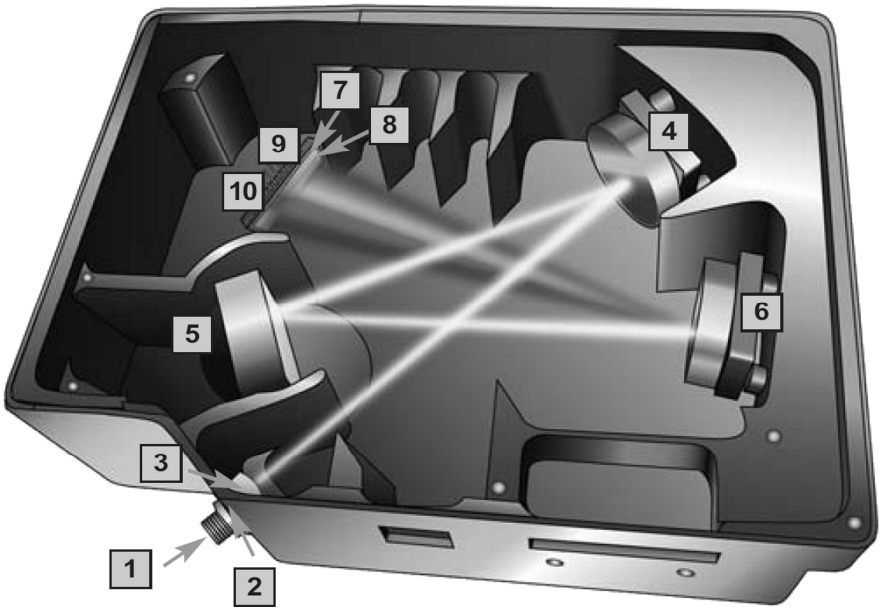

Fig. 3.9 Illustration of the inside of the HR2000, the explanation of the optical parts is given in Table 3.5 [Source: OceanOptics]

Table 3.5 Configuration of the user configured HR2000

Number	Description	Configuration
1	Fibre connector	SMA 905
2	Entrance slit	25 µm
3	Absorbance filter (optional)	-
4	Collimating mirror	Standard
5	Grating	#HC1-UV-NIR, 300 l/mm
6	Focussing mirror	Standard
7	Detector collecting lens (optional)	L2
8	Variable order-sorting filter (optional)	OFLV-200-1100
9	Detector upgrades (optional)	UV2
10	Detector	Sony ILX511 linear CCD array
	Optical fibre	QP600-2-UV-VIS
	Collimator	74-UV

3.2.2 SpectraPro-500i

The second spectrometer system, see Fig. 3.10 dashed rectangle, is a SpectraPro-500i monochromator equipped with a nitrogen cooled CCD. A multichannel plate (MCP) and imaging objectives are placed in between the monochromator and the CCD, to enable detector gating. Due to the size of the MCP and the 1:1 imaging on the detector the usable pixels vary from 1340 x 100 to 910 x 100. The timing is arranged by a programmable gate pulse generator. A photodiode signal (start of the laser pulse) was used as an input trigger for the pulse generator.

The optical fibre (2 m, Ø = 200µm) with microscope objective (20x *NA* = 0,35), applied for coupling the plasma radiation into the spectrograph, was placed under an angle of 36 degrees at a distance of 11 cm from the center of the plasma plume. The other side of the fibre with fixed collimator was placed in front of the adjustable entrance slit of the monochromator.

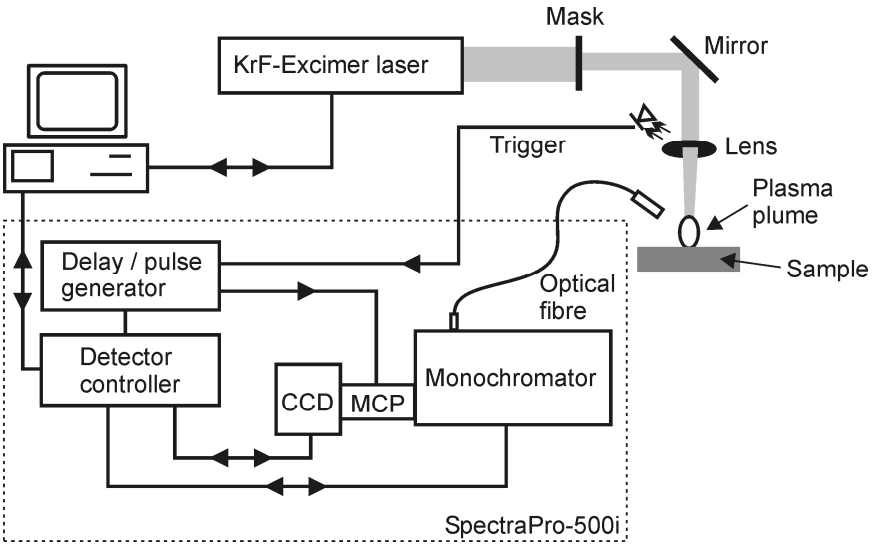

Fig. 3.10 Schematic of the experimental set-up based on the SpectraPro-500i

Table 3.6 Characteristics of the SpectraPro-500i set-up

Monochromator	SpectraPro-500i, Acton Research Corporation
Focal length	500 mm
Aperture ratio	f/6.5
Grating 1	300 grooves/mm
Grating 2	1200 grooves/mm
Controller	ST-138, Princeton Instruments
Software	WinSpec 1.4
CCD	LN/CCD-1340PF, Princeton instruments
Pixel number	1340 x 100
Pixel size	20 x 20 µm
Pulse generator	PG-200, Princeton Instruments

3.3 In-process and post-process sample observation

During (controlled) laser cleaning with the excimer set-up the cleaning process could be followed in-situ on a color monitor. The magnified processing area was displayed on the monitor by a color CCD camera with macro zoom objective. In addition, the process could be viewed directly through the acryl glass laser radiation protection cabin.

In case of cleaning with the hand guided Nd:YAG laser, the cleaning process was observed through laser safety goggles. In addition, a current picture of the sample could be viewed on a computer screen in-process, obtained by the installed webcam above the sample.

Post-processing, the cleaning results were examined by optical microscopy. Therefore, an incident/transmitted light optical microscope (50x, 100x, 200x, 500x and 1000x magnification) and stereo light optical microscope (3.15x – 114x magnification) were used. Both have integrated CCD-cameras to take digital pictures.

4 Layer identification during laser ablation

The key objective of this thesis is the development of a controlling/monitoring system for implementing in laser systems applied for laser cleaning of different polluted artworks to avoid over-cleaning, using on-line plasma emission analysis. Additionally this system should be robust, low cost and easy to handle by restorers without specific knowledge about plasma spectroscopy. Regarding to this, a broad band miniature spectrometer with consequently low resolution was chosen, to acquire the in-process available layer dependent plasma emission. Due to the low resolution of the spectrometer, close elemental emission lines could not be separated. However, the results of this thesis show that in most cases this was no problem.

The in-process acquired emission spectra of different layers were used as discrete fingerprints. Each layer has its individual spectral emission pattern and is therewith distinguishable from other layers in a multi layer arrangement of different materials.

4.1 Linear correlation

The application of linear correlation analysis enables the recognition of single layers (fingerprints) in a multi layer arrangement with the low resolution spectrometer. Because of the technique with reference spectra there is no need for huge spectral emissions tables or either foreknowledge of the elemental

configuration of the different layers. The method of comparing LIB-spectra by linear correlation analysis is described in section 2.3.1.

During laser ablation the plasma emission spectrum of the current ablated volume was correlated with a pre-stored reference spectrum. The online layer identification during the ablation process was accomplished by permanent calculation of the correlation coefficient *r*. If *r* is close to 1, the current spectrum of the ablated volume generally belongs to the same layer (material) as the reference spectrum. The calculation time for *r* (including data transfer from the CCD) was ≤ 100 ms. Considering normally used repetition rates of ≤ 10 Hz for laser cleaning of artworks, complete calculation can be ensured between single laser pulses.

The recorded spectra consisted of 2048 points. In general the complete spectra were used for correlation with the pre-stored reference spectrum. Exceptionally if correlating a fraction of the spectra increased the distinguishability between the layers. If the distinguishability between the spectra of different layers was negatively influenced by reflected laser radiation (248 or 1064 nm) these wavelengths were excluded from the spectra before correlation.

4.2 Reference spectrum

The reference spectrum is a spectrum which represents a material composition or layer configuration. By LIBS experiments with focused laser beam, the reference spectrum is generally created by averaging multiple single shot spectra of the material or layer to be represented. In case of laser cleaning, the reference spectrum was mainly a single shot spectrum. When ablating with a relative large spot the single shot spectra are applicable spectra to represent the layers. This is due to the integrating effect of the larger area in comparison to small focused laser spots whereby local layer configuration variations have more influence on the recorded spectra. When working with artworks, this is an advantage since there is generally no or only less place for testing and recording multiple “reference” spectra.

Depending on the layer construction of the objects to be laser cleaned the reference spectrum was recorded: (A) at a specific depth in the unwanted layer if the unwanted layer composition varies with depth, (B) from the transition layer

or (C) from the layer to be preserved, see Fig. 4.1. The transition layer consists of a mixture of elements from both layers.

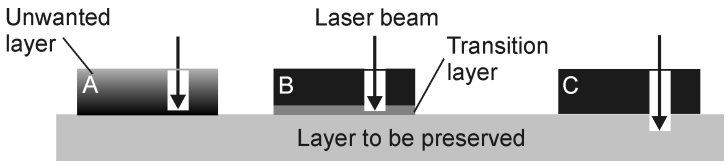

Fig. 4.1 Schematic of the different applied positions for recording reference spectra; A at a specific depth in the unwanted layer if the unwanted layer composition varies with depth, B at the transition layer, C at the layer to be preserved

The crater wall arising during laser ablation influences the emission spectra of the current ablation volume since elements of the wall contaminates the plasma. Therefore it is necessary that the reference spectra are recorded previously ablating the upper layer(s) instead of recording the reference spectra at a position without the unwanted layer(s). This is to secure similarity with the spectra obtained in-process. The form and strength of the LIB-spectra vary with experimental parameters as: laser pulse energy, delay between the laser pulse and plasma emission acquiring and experimental set-up. Therefore the experiments must be accomplished with the same parameter settings at which the reference spectrum was recorded.

4.3 Delay time

Since the layer recognition is based on comparing spectral fingerprints and not on element identification, the emission spectra can also be recorded without delay between the laser pulse and recording the plasma emission. Although the strong continuum emission at the beginning partially covers the elemental line emission (section 2.2.2), it is repeatable and layer dependent due to its physical character [37]. The advantage of recording the broadband continuum in the beginning is the higher emission intensity since the emission intensity rapidly decreases with time. This increases the detectability of the emission in-process and increases the signal to read out noise ratio (section 5.2.1). However, a disadvantage can be the smaller difference between the spectra of various layers since the spectra recorded without delay contain less elemental information.

4.4 Layer identification experiments

The experimental set-up for layer identification during laser ablation was based on the excimer laser and the HR2000 controlled by the LIBS software from OceanOptics, as described in chapter 3.

The principle of linear correlation analysis to distinguish between layers by the weight of the correlation coefficient during laser ablation will be shown by means of two examples. The first example is based on a homogenous artificial multi layer arrangement. The second example is based on original 18th century non-homogeneously polluted parchment.

4.4.1 Artificial multi layer arrangement

The artificial multi layer sample applied to ascertain the potential of the linear correlation coefficient as control parameter is characterized by a homogenous layer thicknesses, see Fig. 4.2. The sample was a 3M laser markable label consisting of four parallel layers with different thicknesses and material configurations, Table 4.1. This sample was chosen as the number of pulses to ablate a defined layer was constant.

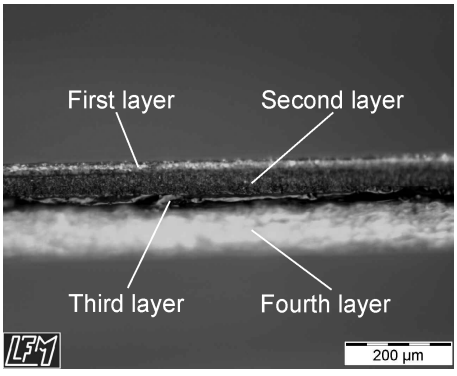

Fig. 4.2 Cross section of the 3M laser markable label

Table 4.1 Characteristics of the multi layer arrangement

Type	3M laser markable label material 7848
First layer	20 µm silver acrylate
Second layer	45 µm matte black acrylate
Third layer	30 µm high-holding acrylic adhesive
Fourth layer	90 µm liner

During ablation of the 3M laser markable label the laser induced plasma emission spectrum of every laser ablation pulse was acquired and correlated with three pre-recorded reference spectra. Fig. 4.3 shows these pre-recorded reference spectra (black, adhesive and liner) which were recorded at the layer

transitions: silver / black, black / adhesive and adhesive / liner (reference type B in Fig. 4.1).

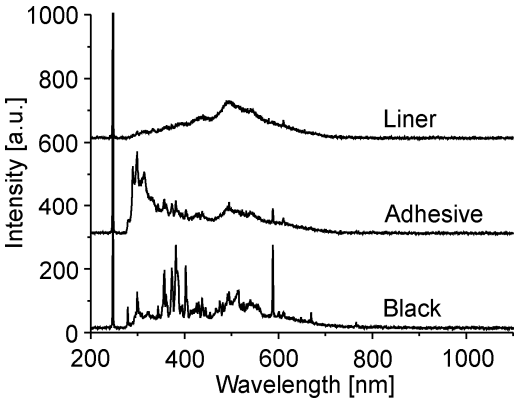

Fig. 4.3 Reference LIB-spectra of the transitions: silver / black, black / adhesive and adhesive / liner

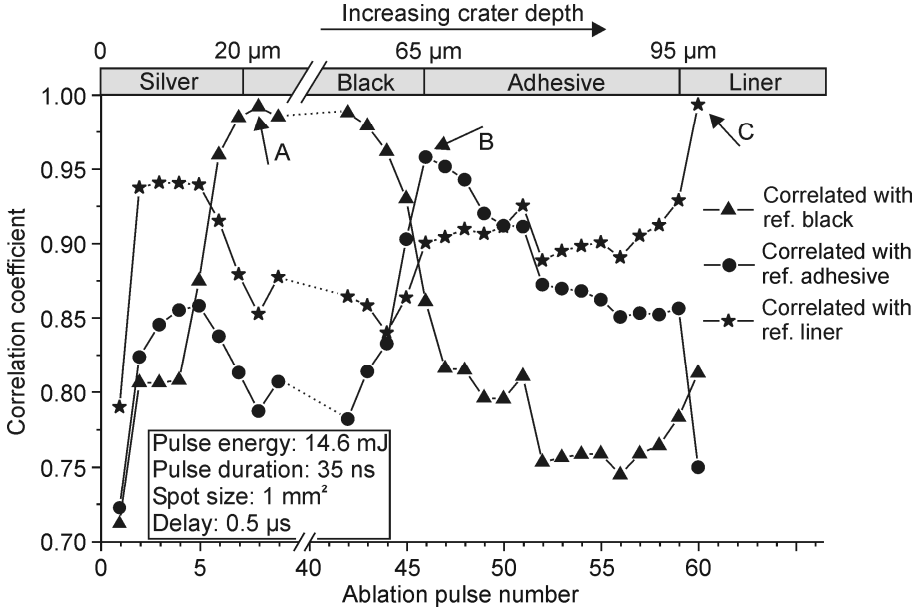

Fig. 4.4 Devolution of the correlation coefficients versus ablation pulse number during ablation of the 3M laser markable label when correlating with the reference spectra black, adhesive and liner. The bar at the top simulates the layers

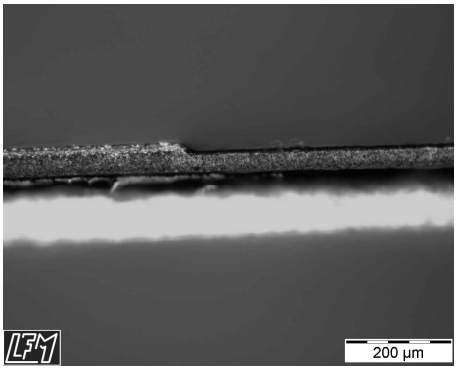

Fig. 4.5 Cross section of the laser markable label ablated till the correlation coefficient when correlating with the black reference spectrum reached its maximum

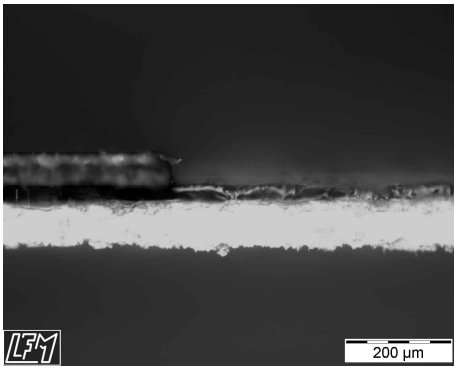

Fig. 4.6 Cross section of the laser markable label ablated till the correlation coefficient when correlating with the adhesive reference spectrum reached its maximum

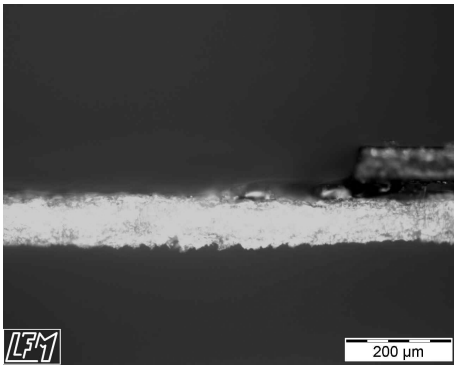

Fig. 4.7 Cross section of the laser markable label ablated till the correlation coefficient when correlating with the liner reference spectrum reached its maximum

The devolution of the correlation coefficients, obtained by correlating the acquired spectra with the reference spectra black, adhesive and liner is shown in Fig. 4.4. The ablation pulse number is a measure for the crater depth. As can been seen, the correlation coefficients pertaining to the correlation with the black reference spectrum achieved its highest value (r = 0.99) at the transition silver / black. This was at the same ablation pulse number at which the

reference spectrum was recorded, arrow A in Fig. 4.4. The same results were obtained for the correlation with the reference spectrum of the adhesive layer, arrow B and for the correlation with the reference spectrum liner, arrow C.

Fig. 4.5, Fig. 4.6 and Fig. 4.7 show cross sections of the laser markable label ablated till the correlation coefficients corresponding to the three reference spectra reached the maximum values, arrows A, B and C in Fig. 4.4. These results demonstrate the feasibility of the linear correlation coefficient as control variable to stop a laser ablation or laser cleaning process at a given level in a homogenous layer arrangement.

4.4.2 Polluted parchment

The experiments on inhomogeneous polluted parchment demonstrate the suitability of the weight of the correlation coefficient to distinguish between pollution and the layer to be preserved. Due to the inhomogeneous pollution, which is generally the case with artworks, the number of laser pulses needed to ablate the pollution layer differs with position on the sample. Therefore, this experiment was accomplished on three different positions on the sample, indicated with experiment 1, 2 and 3.

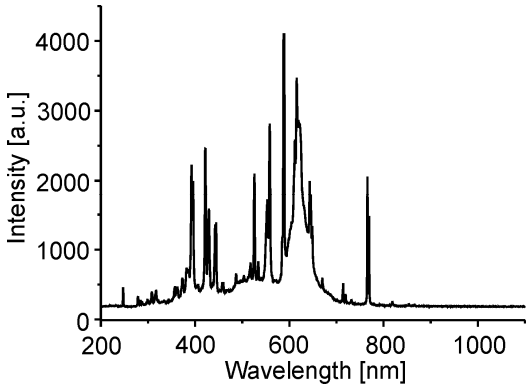

Fig. 4.8 Used reference spectrum

The reference spectrum (Fig. 4.8) was acquired by ablating on one position until the desired cleanness grade was reached (reference type A in Fig. 4.1). Fig. 4.9

shows the correlation coefficients versus ablation pulse number for the three experiments. As can be seen, the maximum is reached once at pulse 3 and twice at pulse 4, since the pollution grade varied between the irradiated positions of experiment 1, 2 and 3. However, the obtained cleanness grade at the maximum weight of correlation was equal for all the experiments and matched the cleanness grade represented by the reference spectrum.

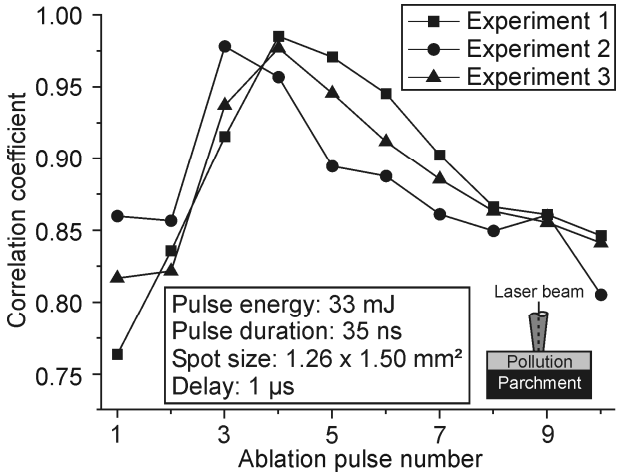

Fig. 4.9 Correlation coefficient versus ablation pulse number, 3 different experiments

Fig. 4.10 shows the LIB-spectra acquired at laser pulse 1, 2, 3 and 4 and pictures of the parchment after laser pulse 1, 2, 3, and 4 achieved during the third experiment. The spectrum of pulse 4 matched the reference spectra, with $r = 0.98$, see Fig. 4.8.

These results show the potential of the linear correlation weight as control variable during laser cleaning of inhomogeneous polluted samples.

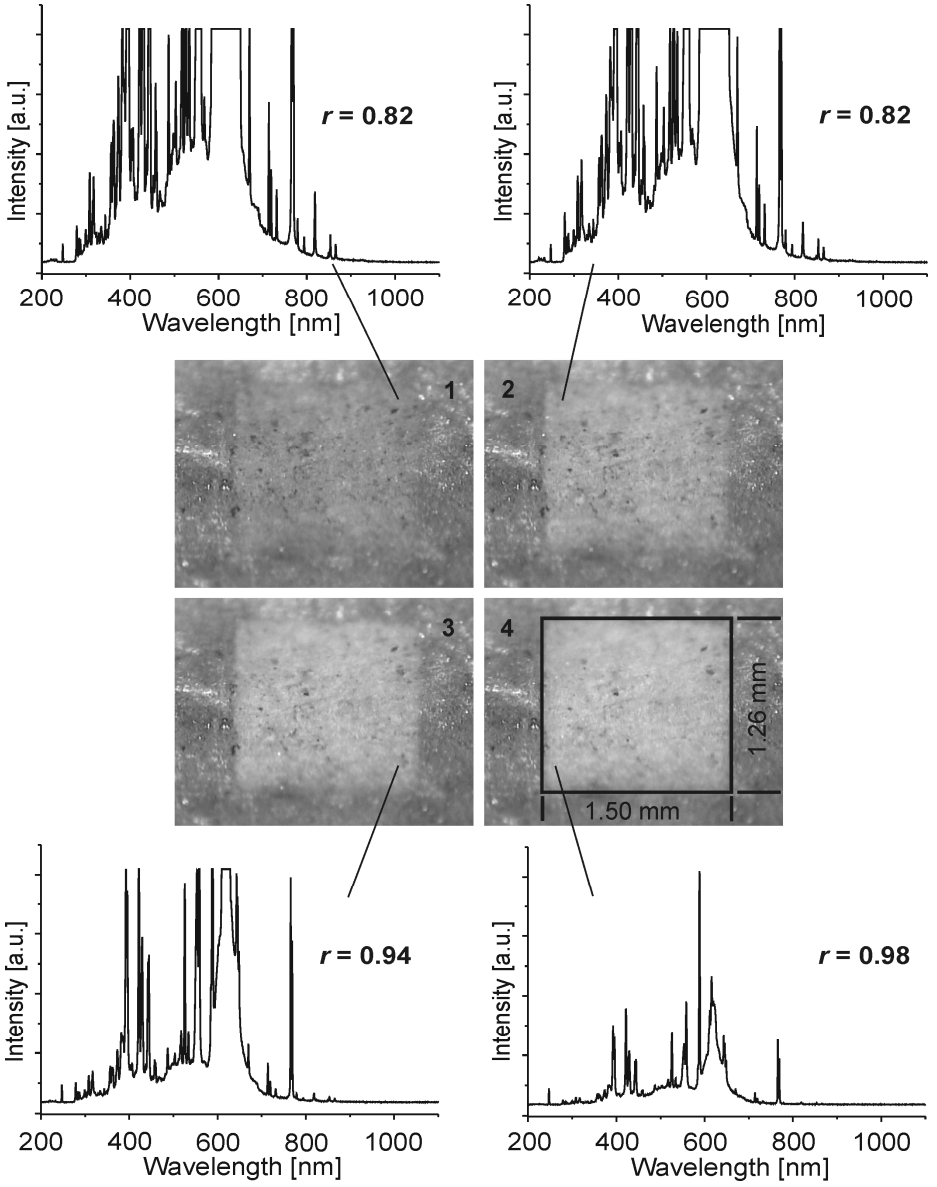

Fig. 4.10 Pictures of the parchment sample after the 1st – 4th laser ablation pulse on one position and the associated LIB-spectra (experiment 3). Laser pulse 4 induced a spectrum which mostly matched the reference spectrum (Fig. 4.8), r = 0.98

4.5 Pre-conditions for process control

Laser induced plasma emission is a stochastic process. The emission spectra of plasmas induced on the same material slightly vary from pulse to pulse. When correlating *n* single shot spectra of one layer with the same reference spectrum the result is *n* correlation coefficients *r*. The distribution of these *r* values can be visualized as shown in Fig. 4.11.

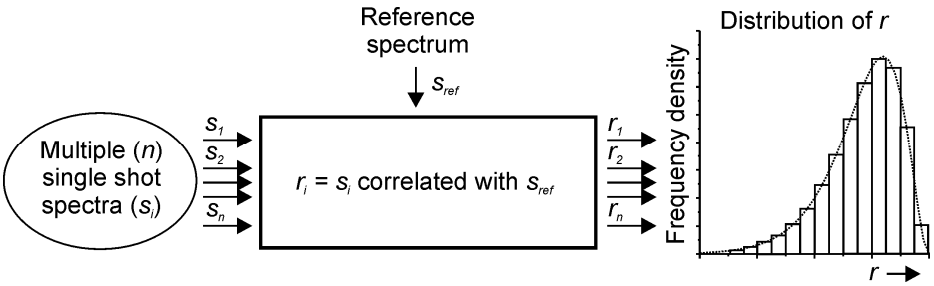

Fig. 4.11 Path from multiple single shot spectra to correlation coefficients distribution

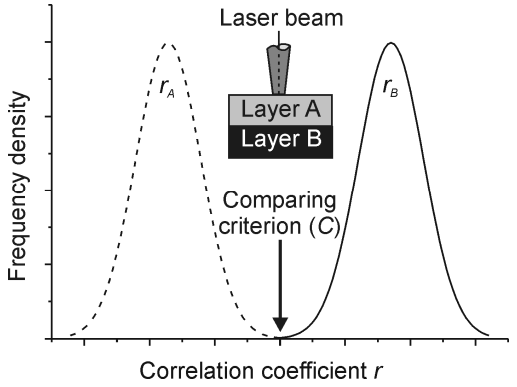

Fig. 4.12 Correlation coefficients distribution of the unwanted layer A and layer to be preserved B

To control laser cleaning processes by means of plasma emission spectroscopy in combination with linear correlation analysis there must be an acquirable plasma emission during the complete process. Secondly, the correlation coefficients, obtained during ablating an unwanted layer (A), should be lower than the correlation coefficients, obtained by reaching the layer to be preserved (B), see Fig. 4.12. Controlled laser cleaning in practice is based on the principle

that when the correlation coefficients exceeds a pre-defined criterion, the ablation process stops. If the comparing criterion is in between of both distributions the correlation coefficient exceeds the criterion (*C*) when reaching layer B.

When the layers have a very similar chemical composition it can occur that the distributions of correlation coefficients overlap and a successful process control cannot be guaranteed. A reduction or vanish of the overlap is in some cases achievable by the use of other parameters without affecting the artwork.

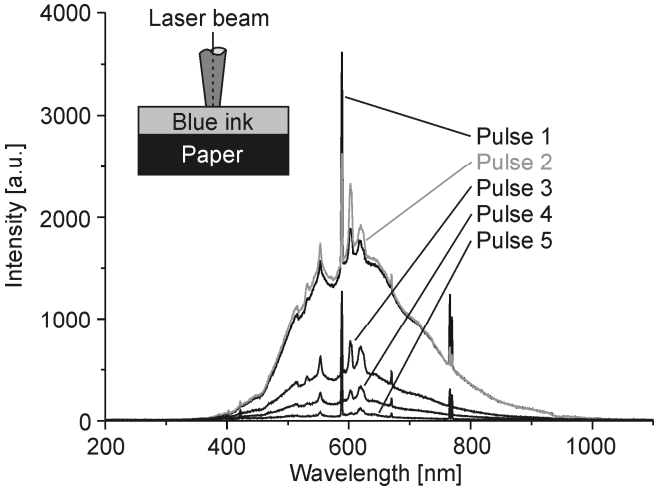

Fig. 4.13 LIB-spectra of the blue-paper sample, associated to pulse 1 - 5

As an example we consider a sample with a homogeneous two layer configuration; paper with a blue ink layer on top. The experimental parameters were: pulse energy 22 mJ, delay 1.5 µs, spot size 1.6 x 1.6 mm^2. Since the sample was homogeneous 5 pulses per position were constantly needed to ablate the blue ink layer. Fig. 4.13 shows the typical spectra associated to pulse 1 – 5. This process was repeated on 50 positions resulting in 50 x 5 spectra.

All the obtained spectra were correlated with a single shot reference spectrum which was acquired at pulse 5 (representing the desired cleanness grade of the paper). This leads to 5 x 50 correlation coefficients. These correlation coefficients are visualized per pulse number in histograms, see Fig. 4.14. As can been seen, there is a relative large gap between the distributions of pulse 1 – 3 and the distributions of pulse 4 and 5. Furthermore, no overlap

exists between the distribution of pulse 4 and pulse 5. With the applied experimental parameters and reference spectrum it is possible to stop the ablation process after pulse 4 or 5 by choosing an appropriate comparing criterion (e.g. 0.925 for pulse 4 and 0.975 for pulse 5). The pulse 1 correlation coefficients distribution shows a higher variance since the spectrum of pulse 1 is indirectly contaminated by varying surface pollutions.

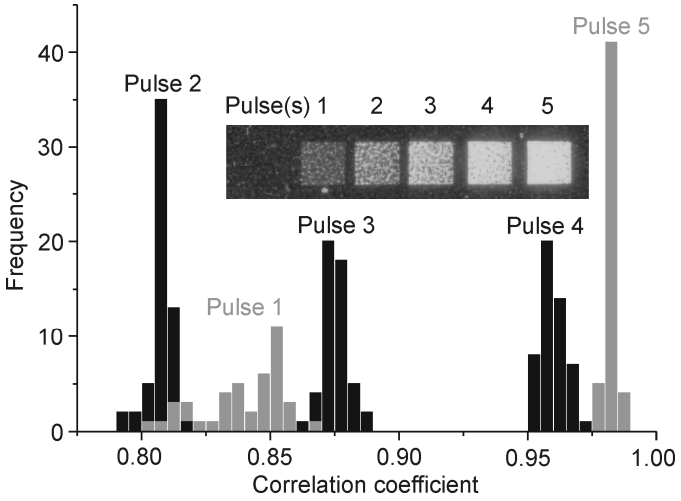

Fig. 4.14 Correlation coefficients histograms per pulse number. The picture shows the blue-paper sample before and after 1 – 5 subsequent laser ablation pulses (spot size 1.6 x 1.6 mm^2)

4.6 Conclusions and discussion

The experiments in this chapter show that it is feasible to stop a laser ablation process during cleaning of homogeneous and inhomogeneous polluted samples on basis of the correlation coefficient. This method can be applied if the following conditions are fulfilled:

- there is a recordable plasma emission during the complete process
- the spectra of the different layers or material configurations vary in form and intensity
- the distributions of correlation coefficients, corresponding to the layers to be distinguished between, show no overlap.

5 Influence of process parameters on the distribution of correlation coefficients

Parts of this chapter are published in the article: M. Lentjes, K. Dickmann, J. Meijer; Influence of process parameters on the distribution of single shot correlation coefficients obtained by correlating LIB-Spectra; Applied Physics A, 2007, Vol. 88, pp. 661-666

This chapter presents a systematic study about the influence of the process parameters on the distribution of correlation coefficients. In every experiment only one parameter was changed. Per setting 50 LIB-spectra were recorded and correlated with one reference spectrum, resulting in 50 correlation coefficients per setting. The results are presented as correlation coefficient distributions versus setting for each investigated parameter. The investigated process parameters are:

- pulse energy
- delay time
- integration time
- spectrometer resolution

The influence of the following process parameter variations on the distribution of correlation coefficients was investigated by cross-correlation:

- object lens distance variation
- irradiation angle variation
- crater depth variation
- upper layer thickness variation

The results indicate that the researched parameters have an indirect and/or direct influence on the distribution of correlation coefficients.

Castle et al. [80] have reported a systematic study about the influence of temporal signal development, sample translational velocity, number of spectra accumulated, laser pulse stability, detector gate delay, surface roughness and using background correction on the emission of atomic copper lines but up to now no systematic research has been reported dealing with influences of process parameters on the distribution of single shot correlation coefficients.

5.1 Experimental setup and applied method

The experimental set-up used for the presented work in this chapter was generally based on the HR2000 spectrometer and the 248 nm KrF-excimer laser. The SpectraPro-500i spectrometer was applied for the integration time and resolution experiments. The mask was projected by an f = 120.7 mm lens onto the sample (diffuse imaging). The experiments were carried out on a certified standard aluminium alloy and a standard Si-wafer. Per setting, with a frequency of 1 Hz at five positions, 10 LIB-spectra were recorded after five previous cleaning pulses. All the spectra were correlated in the interval 280 to 1100 nm to neglect the influence of the excitation wavelength (248 nm) on the measurements.

The 50 LIB-spectra of each setting have been averaged and applied as reference spectrum for that particular material and setting. The single shot spectra were correlated per setting with their reference spectrum.

In case of cross-correlation the 50 LIB-spectra of the initial setting have been averaged and applied as reference spectrum for all the settings within that experiment. The single shot spectra were correlated per setting with this reference spectrum.

5.2 Results and discussion

The experiments were generally carried out with and without delay between laser pulse and the measurement of the spectra. The applied delay time varied per experiment since a usable spectrum for all settings within the experiment had to be acquired. In cases of CCD-detector saturation a neutral density filter was placed in front of the optical fibre during the complete experiment.

5.2.1 Influence of S/N ratio

To research the direct influence of different parameter settings on the distribution of correlation coefficients, first the influence of the signal to noise ratio (S/N) was investigated. Noise is an unwanted characteristic of electronic signals. The characteristic readout noise of the HR2000 spectrometer is 20 counts peak to peak (datasheet OceanOptics). Since the HR2000 spectrometer has no intensifier the emission spectra cannot be optically amplified to increase the S/N ratio.

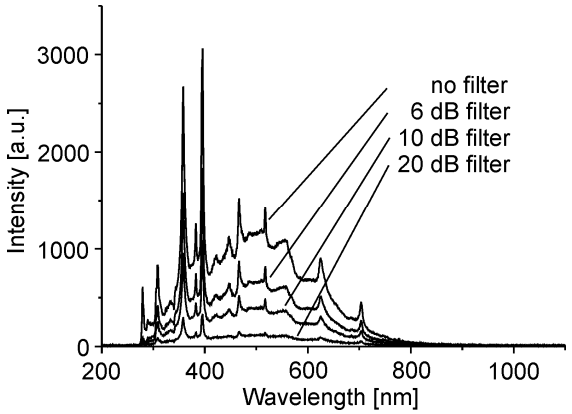

Fig. 5.1 Al LIB-spectra acquired with no and different attenuation filters in front of the collimator

The influence of the S/N ratio on the distribution of correlation coefficients was investigated by acquiring spectra with and without attenuation filters. Under the same experimental conditions 50 spectra were recorded with no filter, a 6 dB filter, a 10 dB filter and a 20 dB filter in front of the collimator and correlated with their reference spectrum. Fig. 5.1 shows the averaged spectra with and without filters. The influence of the signal strength (S/N ratio) on the variance and the mean of the correlation coefficients can be seen in Fig. 5.2. The variance increases and the mean decreases with decreasing signal strength. This means in case a parameter change causes a decrease of the emission intensity, the S/N ratio indirectly affects the distribution of correlation coefficients. From this can be concluded that a low variance and high mean are obtained with measured spectra with a high S/N ratio.

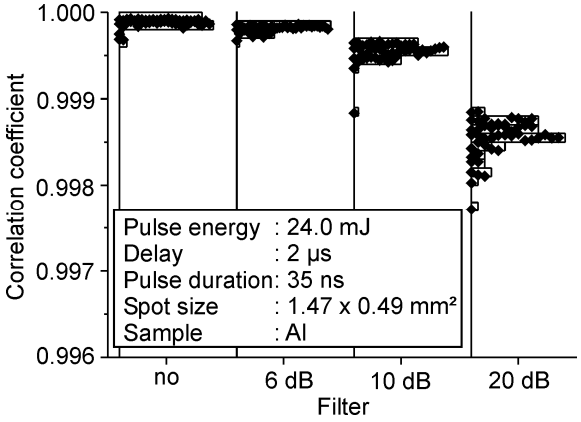

Fig. 5.2 Distribution of correlation coefficients versus filter (S/N ratio)

5.2.2 Influence of pulse energy

To investigate the influence of the pulse energy on the distribution of the single shot correlation coefficients, at 12 different energies 50 spectra were recorded and each of them correlated with their reference. The pulse energy was varied (11.8 to 37.9 mJ) by an external attenuator, whereby the relative standard deviation (RSD = 1.7 %) of the pulse energy was constant over the total range. Fig. 5.3 shows the averaged spectra recorded with pulse energies 11.6 mJ, 28.0 mJ and 37.9 mJ (Al, no delay, 20 dB filter in front of collimator). The spectral intensity decreases with pulse energy. The variance of the correlation coefficients decreases and the mean increases with increasing pulse energy as shown in Fig. 5.4. This behavior was similar for all energy experiments, Al 2 µs delay, Si no delay and Si 1 µs delay.

A comparison of the devolution of Fig. 5.4 and the spectra in Fig. 5.3 with Fig. 5.2 and Fig. 5.1 results in the conclusion that a lower pulse energy has the same effect as an attenuated signal (by filtering) on the distribution of correlation coefficients. The variation was indirect caused by the decreasing S/N ratio with decreasing pulse energy. The Al 2 µs delay and Si 1 µs delay experiments additionally showed a slightly higher variance for all pulse energies in comparison to the experiments without delay due to the increased intensity fluctuations of the elemental lines after a delay.

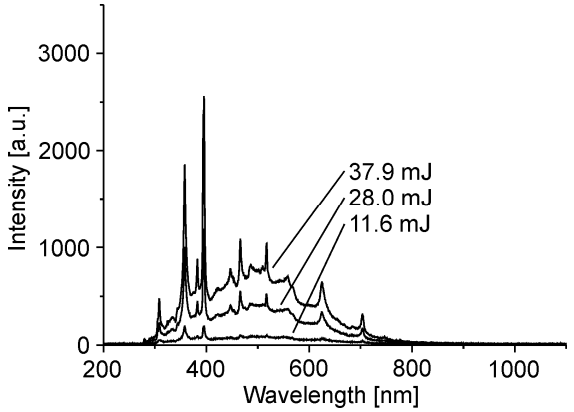

Fig. 5.3 Spectra of Al recorded with different pulse energies, no delay and 20 dB filter

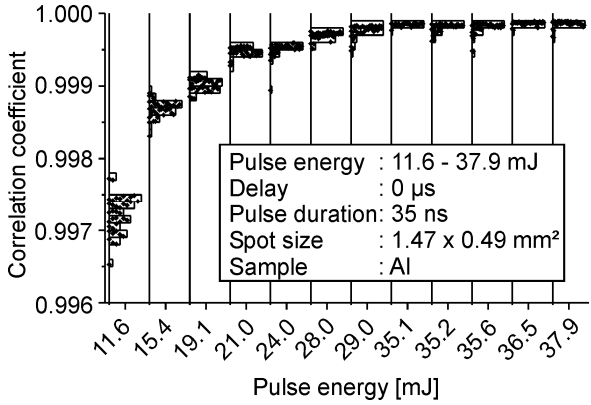

Fig. 5.4 Distribution of correlation coefficients versus pulse energy

5.2.3 Influence of delay time

The influence of the delay time on the variance and mean of the correlation coefficients is investigated by varying the delay in steps of 500 ns from 0 to 2.5 µs. Fifty spectra were recorded per setting and each correlated with their reference. Since the results of Si and Al are identical only the graph of Al is shown (Fig. 5.5). There is a decrease of the mean and an increasing variance with increasing delay.

With increasing delay time the plasma emission intensity decreases and therewith the S/N ratio. This indirectly affects the variation of the distributions. The direct effect of the delay time on the distribution of correlation coefficients is

caused by the increasing intensity fluctuations of the elemental emission lines with increasing delay time. Castle et al. [80] also investigated that the relative standard deviation of single lines increases with increasing delay.

From this can be concluded that spectra recorded without delay are the most reproducible. This results in a low correlation coefficient variance and high mean.

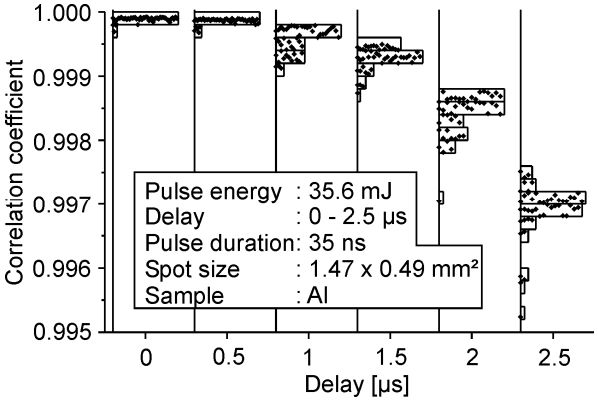

Fig. 5.5 Distribution of correlation coefficients versus delay

5.2.4 Influence of integration time

For these experiments the SpectraPro spectrometer was applied which has the facility to adjust the integration time. The typical temporal development of the laser induced plasma emission is described in section 2.2.2. At every setting 50 spectra were recorded and each correlated with their reference. Fig. 5.6 shows an increase of the variance and decrease of the mean for the integration times 1 µs and 500 ns in comparison to the longer integration times, Al-sample at a delay of 2 µs. The experiment without delay showed a constant behavior (Fig. 5.7). The same results are obtained for the Si sample.

The distributions of the experiments without delay show no significant variation since the intense and repeatable broad band white light emission dominates the spectra. The spectra recorded with an integration time of 500 ns were already intense enough to have no significant influence of the noise.

In case of 2 µs delay the variances were slightly influenced by the intensity fluctuations of the elemental lines. The reproducibility of the spectra recorded

with shorter integration times (< 5 µs) were also influenced by the low signal to noise ratio.

From this can be concluded that spectra recorded with a long integration time (> 5 µs) are the most reproducible.

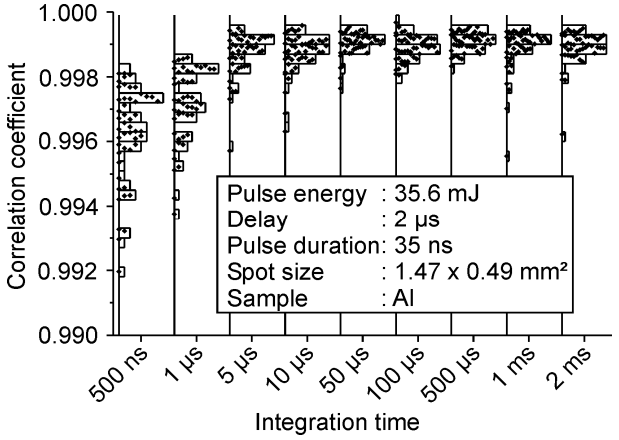

Fig. 5.6 Distribution of correlation coefficients versus integration time, Al-sample 2 µs delay

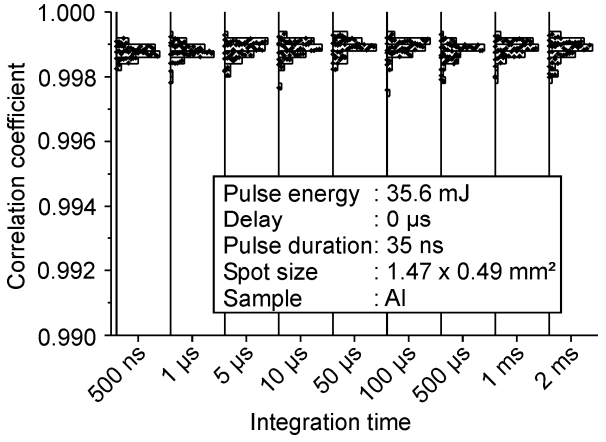

Fig. 5.7 Distribution of correlation coefficients versus integration time, Al-sample no delay

5.2.5 Influence of the spectrometer resolution

To investigate the influence of the optical resolution on the correlation coefficients both spectrometer systems were used. Since the SpectraPro is equipped with two different gratings (300 l/mm and 1200 l/mm) three optical resolutions were analyzed. Again at every setting 50 spectra were recorded and correlated with their reference. Fig. 5.8 shows the results of Al at no delay.

A decreasing variance and increasing mean with decreasing optical resolution was found. This can be explained by the higher spectral integrating range per CCD pixel at lower resolution, whereby intensity fluctuations of atomic lines have less influence on the total intensity of the pixel. Another reason can be the decrease of intensity per CCD pixel at higher resolution since the optical dispersion increases with increasing resolution. This leads to a decrease of the signal to noise ratio. The same results were obtained for Al and Si at a delay of 2 µs and Si without delay.

From this can be concluded that spectra recorded with a spectrometer with a low resolution are the most reproducible. This results in a low correlation coefficient variance and high mean.

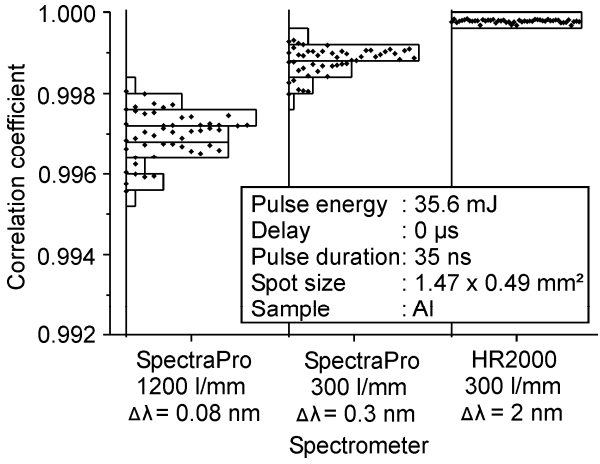

Fig. 5.8 Distribution of correlation coefficients versus spectrometer

5.2.6 Influence of object-lens distance deviation

During laser processing of non-plano objects the object lens distance can vary. The influence of a relative object lens distance deviation was investigated by

cross-correlation. The mask was projected by an f = 120.7 mm lens to a 1.46 x 0.86 mm^2 rectangle onto the sample (image distance was 142 mm, diffuse imaging); this object lens distance was set as reference, with z = 0.

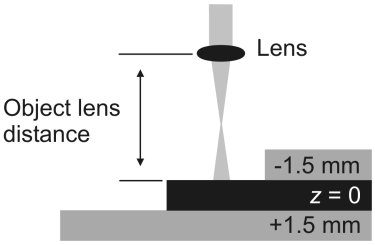

Fig. 5.9 Schematic of the distance displacement with respect to z = 0

Table 5.1 Energy density at different z

Object lens distance z [mm]	Spot area [mm^2]	Energy density [mJ/mm^2]
-1.5	1.14	31.2
0	1.26	28.3
1.5	1.35	26.4

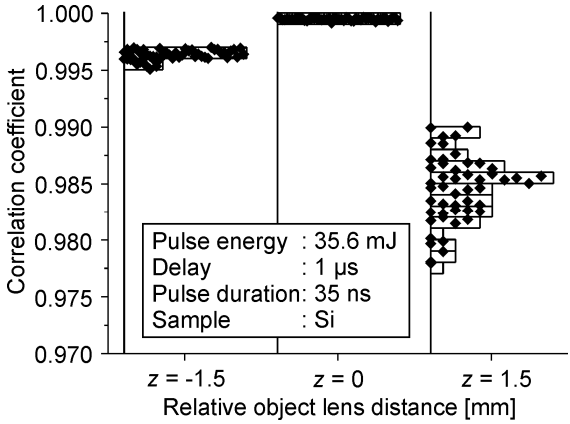

Fig. 5.10 Distribution of correlation coefficients versus relative object lens distance, cross-correlation with the reference spectrum of z = 0

The 50 spectra recorded at z = 0 were averaged and used as reference. A displacement of the sample about -1.5 mm and 1.5 mm (Fig. 5.9) with respect to z = 0 affects a modification of the spot size to 1.44 x 0.79 mm^2 and 1.44 x 0.94 mm^2 (the divergence of the excimer laser beam differs in both directions) which leads to a change of the energy density (Table 5.1). The spectra recorded at z = -1.5, z = 0 and z = 1.5 were correlated with the

reference spectrum of $z = 0$ (cross-correlation). The results show that a variation of the object lens distance during laser processing can highly affect the distribution of correlation coefficients (Fig. 5.10).

Due to the object lens distance variation the energy density and the spot size changes and therewith the form of the spectra of z = -1.5 and z = 1.5 in comparison to z = 0. Additionally z = 1.5 suffered from the decreased S/N ratio.

From this can be concluded that spectra recorded from flat samples with a homogeneous thickness are the most reproducible. This results in a low correlation coefficient variance and high mean.

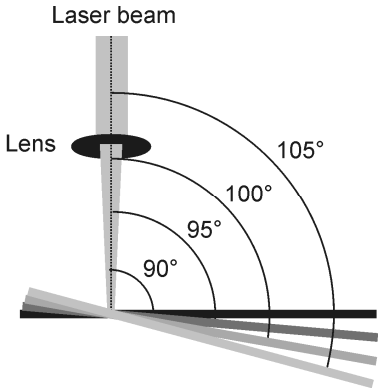

Fig. 5.11 Schematic of the different irradiation angles

Table 5.2 Energy density at different irradiation angles

Irradiation angle [°]	Spot area [mm²]	Energy density [mJ/mm²]
90	0.76	28.3
95	0.77	27.9
100	0.78	27.6
105	0.79	27.2

5.2.7 Influence of irradiation angle

To investigate the influence of an irradiation angle deviation on the distribution of correlation coefficients, spectra were recorded at 4 different irradiation angles (90°, 95°, 100° and 105°) and cross correlated with the reference spectrum of 90°. The 50 spectra recorded at this irradiation angle were averaged and used as reference. The irradiation angle was varied with respect to the laser beam (Fig. 5.11). Irradiation angle variations occur in practice when objects are angular, rough or not flat. When working with hand-guided beam delivery, variations of the irradiation angle are additionally caused by the operator. A

modification of the irradiation angle leads to a change of the energy density (Table 5.2). The observed part of the plasma emission shifts with irradiation angle (on-axis plasma emission collection) since the atoms emerge perpendicular away from the surface independent of the irradiation angle. However, at early times, the continuum light emission shows a symmetry along the axis of the incident laser beam (s. Fig. 5.13) [81, 82].

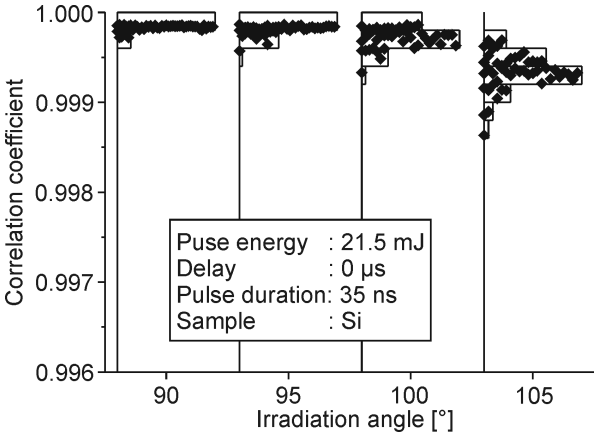

Fig. 5.12 Distribution of correlation coefficients versus irradiation angle, cross-correlation with the reference spectrum of 90°

Fig. 5.12 shows a decrease of the mean and increasing variance with increasing irradiation angle. The same results were obtained for Al without delay. The experiments with delay (Al and Si, 1 µs) showed a stronger decrease of the mean and increasing variance with increasing irradiation angle. This can be explained by the stronger influence of the observed plasma area shift in comparison to no delay. Additionally the delayed experiments suffered from the increased fluctuations of the elemental lines.

From this can be concluded that spectra recorded from smooth flat samples are the most reproducible. This results in a low correlation coefficient variance and high mean.

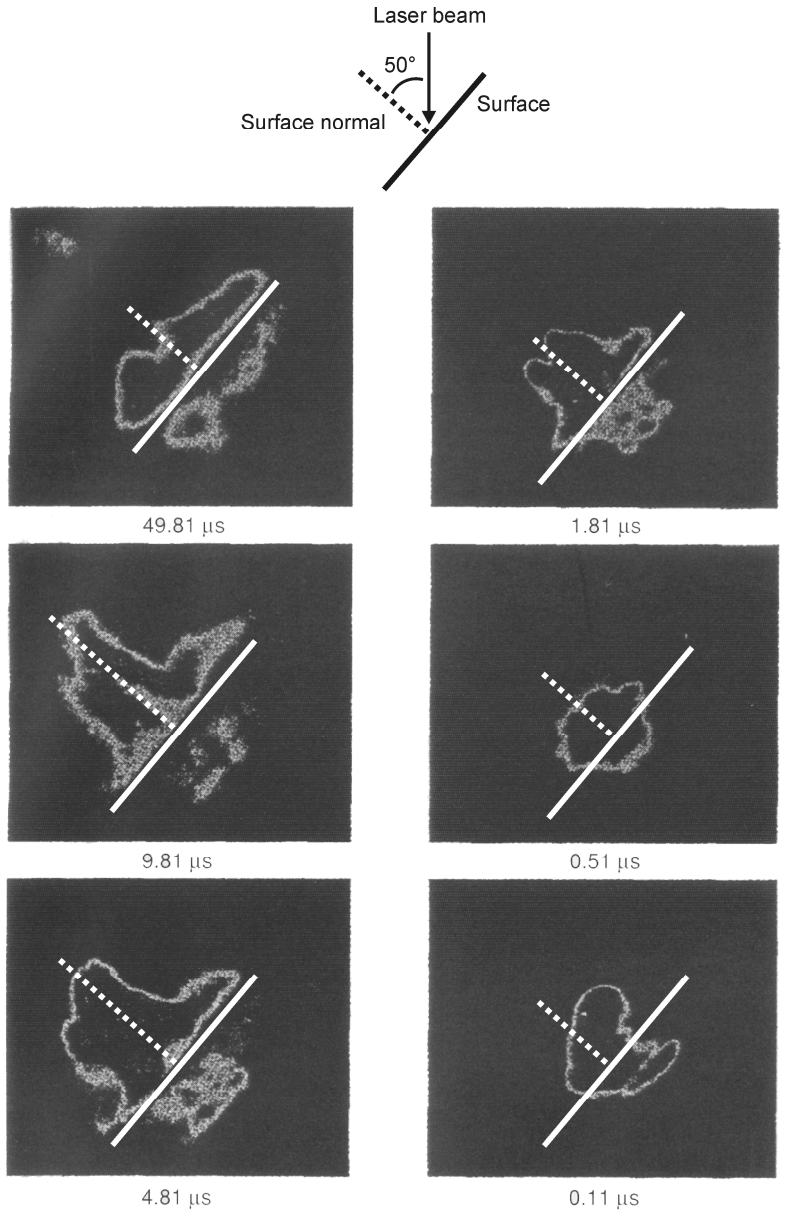

Fig. 5.13 Temporal evolution of the plasma light emission formed by a laser pulse incident at 50° on a Cr-coated aluminium sample. The plasma light was spectrally filtered to monitor the 425 nm Cr(I) line. At a delay of 0.11 µs the continuum emission is symmetric along the path of the incident laser beam. In the other figures is shown that at later times the central axis of the atomic emission is the surface normal (source: [82]).

5.2.8 Influence of crater depth

The influence of the laser induced crater depth on the distribution of correlation coefficients was investigated at 1 µs delay and no delay by pulsing 1000 pulses on Si and Al. The spectra of the first 50 pulses were averaged and applied as reference spectrum. All spectra were correlated with this reference spectrum. To evaluate the results, distributions were formed per 100 pulses; the first distribution consisted of pulse 1 to 100 and so on. Fig. 5.14 shows the results of Si at no delay, the mean slightly decreases and the variance slightly increases with increasing pulse number (the pulse number is a measure for the crater depth, 1000 pulses ≙ 100 µm). The same results were obtained for the Si 1 µs delay, Al 1 µs delay and Al no delay.

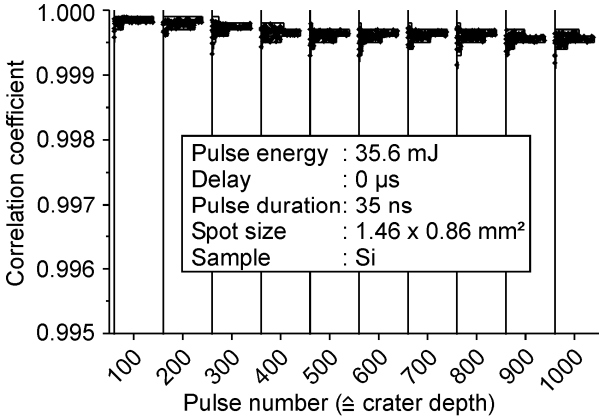

Fig. 5.14 Distribution of correlation coefficients versus pulse number, cross-correlation with the reference spectrum of pulse 1 to 50

Since the spot size (1.46 x 0.86 mm²) is relatively large there is no constriction of the plasma into the crater which is a well-know phenomenon when ablating with small focus. Actually the plasma emission intensity slightly increased with increasing depth. This is expected to be caused by the increased laser radiation interaction surface due to the arising crater wall with increasing depth.

From this can be concluded that spectra recorded at the same depth (pulse number) are more identical than spectra recorded at different depths. This results in a low correlation coefficient variance and high mean.

5.2.9 Influence of the upper layer thickness

The reference spectra used for controlled laser cleaning as described in section 4.2 are recorded: at a specific depth in the unwanted layer, from the transition layer or from the layer to be preserved. In general the pollution layers have an inhomogeneous thickness. The thickness of the first layer influences the spectrum of the second layer since the plasma is contaminated by elements of the crater wall.

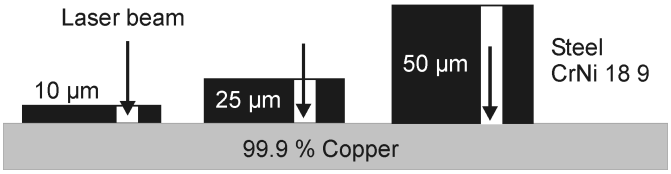

Fig. 5.15 Schematic of the applied two layer system, pure copper with 10, 25 and 50 µm steel

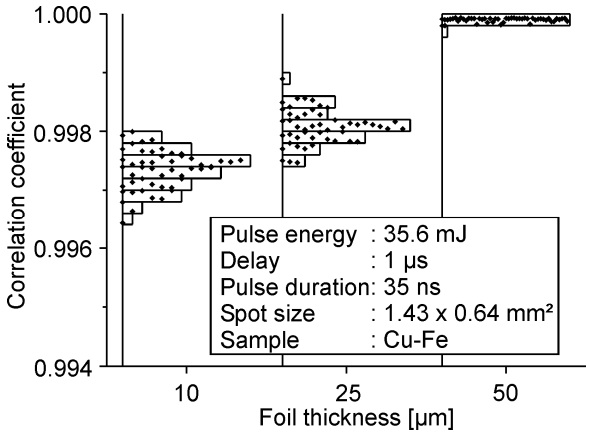

Fig. 5.16 Distribution of correlation coefficients versus layer thickness, cross-correlation with the reference spectrum of foil thickness 50 µm

The influence of the upper layer thickness on the distribution of correlation coefficients was investigated by recording 3 x 50 spectra of pure copper with upon steel foils with different thickness as given in Fig. 5.15. The craters in the steel foils were ablated previously recording the copper spectra with the same laser in one process simulating laser cleaning in practice. Fig. 5.16 shows the

distributions when correlating all spectra with the reference of layer thickness 50 µm (cross-correlation). It is visible on the basis of the different distributions that the (steel) crater wall height influences the recorded copper spectra. The spreading of the correlation coefficient distribution of the second layer will increase with increasing thickness and composition variation of the first layer.

From this can be concluded that spectra recorded from the second layer are the most reproducible when the upper layer has a homogenous thickness. This results in a low correlation coefficient variance and high mean.

5.3 Conclusions

The parameters that can be varied depend on the applied equipment and process. For example by laser cleaning processes the energy density cannot be set arbitrary high to obtain a bright plasma emission. The maximum allowed energy density without disturbing depends on the object to be cleaned. Conversely, in the case of steel identification a high energy distribution will pose no problem.

The experiments showed that all the investigated parameters had an indirect and/or direct influence on the distribution of correlation coefficients. The S/N ratio has a significant influence on the reproducibility of measured spectra with a low intensity, defined as indirect influence. In case of intense spectra the influence of the noise on the form of the measured spectra can be neglected. Since miniature fibre optical spectrometers are not featured with intensifiers this influence can not be remedied (without changing the collecting set-up). The most reproducible spectra will be obtained with the in Table 5.3 given process parameter settings.

Table 5.3 Process parameter settings for most reproducible spectra

Process parameter	Setting	Experiment value
Pulse energy → S/N ratio	High	> 35 mJ
Delay	No	0 µs
Integration time	Long	> 5 µs
Spectrometer resolution	Low	> 2 nm
Sample structure	Flat, smooth, homogenous thickness	

It should be noted that spectra obtained without delay are more reproducible than spectra acquired with a delay. However, the distinguishability between the spectra of different materials can decrease due to the missing atomic emission lines in the spectra acquired without delay. The spectra recorded with a low resolution spectrometer are more reproducible than spectra recorded with a higher resolution spectrometer. But the distinguishability between the spectra of the different materials can decrease due to the missing resolving power.

6 Calculation and optimization of sample identification

Parts of this chapter are published in the article: M. Lentjes, K. Dickmann, J. Meijer; Calculation and optimization of sample identification by laser induced breakdown spectroscopy via correlation analysis; Spectrochimica Acta Part B 62 (2007) 56-62

As mentioned in section 2.2 linear correlation analysis is used as a technique for the identification of samples with a very similar chemical composition by laser induced breakdown spectroscopy [67-71]. The spectrum of the “unknown” sample is correlated with a library of reference spectra and identified by the weight of correlation.

The method works well as long as the distribution of correlation coefficients has no overlap with the distribution received by correlating the same spectra with another reference in the library, identification is not guaranteed when the distributions overlap (Fig. 6.1).

In this chapter a method for estimating the probability of identification by single shot correlation analysis is given. Single shot is an important requirement because in case of automated control after each shot has to be decided if another shot is necessary or not. In case the probability of identification by single shot correlation analysis is below 99.9% a second method is given to calculate the number of spectra to be averaged to achieve a 99.9 % right identification. Both methods are verified experimentally. The adoption of these

methods to estimate the probability of layer identification during laser cleaning is described in section 6.6.

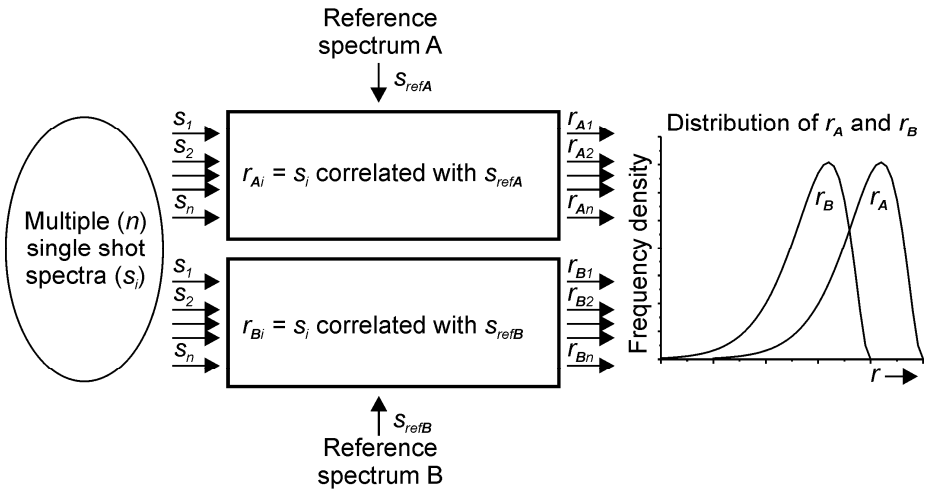

Fig. 6.1 Multiple single shot spectra correlated with two reference spectra, both distributions show an overlap

6.1 Experimental

The experimental set-up used for the work presented in this chapter is based on the SpectraPro-500i spectrometer, like described in section 3.2.2. The 300 grooves/mm grating was centered on 375 nm resulting in a spectral range from 320 to 440 nm. The time delay between the start of the laser pulse and the acquisition was 2 µs with a gate of 5 µs.

The plasma was generated by the KrF-Excimer laser with a standard mask illumination and imaging set-up. The mask was projected by an f = 120.7 mm lens to a 1.5 x 0.5 mm² spot onto the sample (diffuse imaging). The applied pulse energy was 45 mJ. The experimental settings of the spectrometer and laser have been kept constant during the experiments. Two aluminum-alloy standards AS1 and AS3 were used because their distributions overlap. The composition of both standards is given in Table 6.1.

Per sample at 10 positions 8 LIB-spectra after 5 previous cleaning pulses were recorded. The 8 LIB-spectra of one position were averaged and stored as a reference spectrum (Ref.AS1, Ref.AS3) and not further used for correlation.

Table 6.1 Element concentration Al-alloy standard AS1 and AS3 [m/m %]

	Cu	Mg	Fe	Mn	Ni	Zn	Pb	Sn	Ti	Cr	Si	Al
AS1	1.08	0.7	0.32	0.14	1.17	0.11	0.06	0.063	0.53	0.055	10.1	85.67
AS3	0.67	0.56	0.84	0.56	0.61	0.48	0.16	0.21	0.33	0.15	10.4	85.03

6.2 Single shot distribution

Correlating *n* single shot spectra of a sample with one reference spectrum results in *n* correlation coefficients *r*. These results can be presented by a histogram from which a probability density function can be obtained. This function is applied to predict the probability of a result for the random variable $\underline{r}$. The distribution functions of the data obtained in this work are found to be gamma distributions [83]. The gamma distribution is a “family” of distributions changing from an exponentional shape to a normal distribution depending on the chosen shape parameter *γ;* see Fig. 6.2.

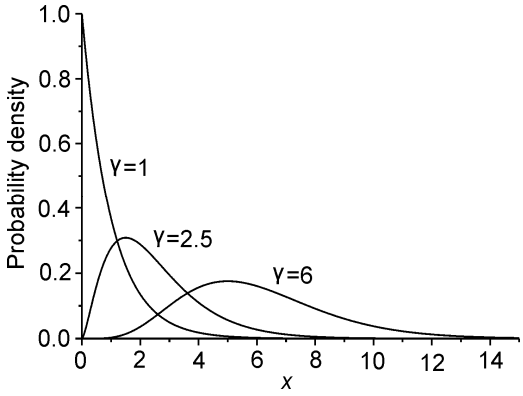

Fig. 6.2 Gamma distributions with different shape parameter (γ) and constant scale parameter (β = 1)

For identical spectra the distribution of correlation coefficients shows an exponentional form. Since the gamma distribution starts at $x = 0$ the gamma distribution is applied for $x = 1 - r$; see Fig. 6.3. It is clearly shown that a normal distribution does not fit in this case. The gamma distribution, however, requires more calculation effort.

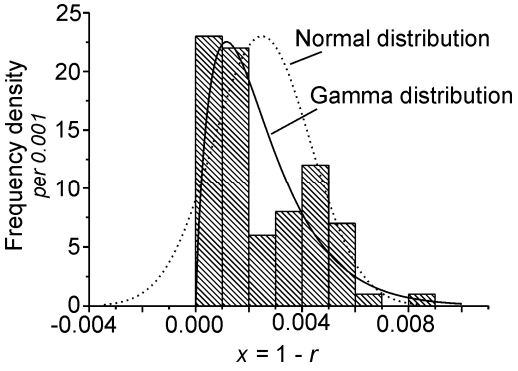

Fig. 6.3 Histogram with fitted gamma and normal distribution

6.3 Probability of identification

For the identification of “unknown”-samples the spectral emission of the plasma was first measured and then correlated with a library of reference spectra. The highest correlation coefficients are obtained by correlating spectra from sample “AS1” with the reference spectrum *A* of sample ”AS1” and not when correlating with the reference spectrum *B* of sample “AS3”, $\left(\underline{r}_A > \underline{r}_B\right)$ see Fig. 6.4. If there is an overlap between the distributions (Fig. 6.5) a positive identification is not guaranteed. The probability $P\left(\underline{r}_A > \underline{r}_B\right)$ is calculated as described in 6.3.1 in case of gamma distributions or like described in 6.3.2 for normal distributions.

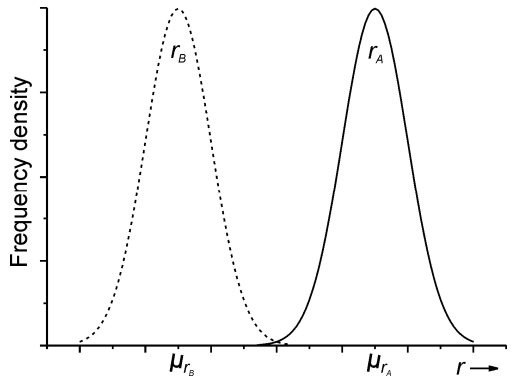

Fig. 6.4 Two normal distributions without overlap, the probability of identification is > 99.9%

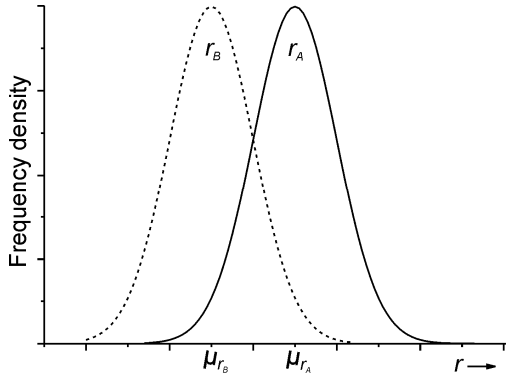

Fig. 6.5 Two normal distributions with an overlap, the probability that $\underline{r}_A > \underline{r}_B$ is < 99.9%

6.3.1 Gamma distribution

The equation for the probability density function of the Gamma distribution is:

$$f(x) = \frac{\left(\frac{x}{\beta}\right)^{\gamma-1} e^{\frac{-x}{\beta}}}{\beta\Gamma(\gamma)} \quad x \geq 0 \quad \gamma, \beta > 0 \tag{6.1}$$

In which γ is the shape parameter, β the scale parameter and Γ the Gamma function:

$$\Gamma(x) = \int_0^\infty t^{x-1} e^{-t} \mathrm{d}t \tag{6.2}$$

The shape parameter γ and scale parameter β are $\gamma = \frac{\mu^2}{\sigma^2}$ and $\beta = \frac{\sigma^2}{\mu}$.

where μ is the expected value and σ the standard deviation of the samples. The gamma distributions are applied for $x = 1 - r$. The equation to calculate the probability $\underline{r}_A < \underline{r}_B$ is:

$$P(\underline{r}_A < \underline{r}_B) = \int_0^1 \int_0^y f(x) g(y) \mathrm{d}x \mathrm{d}y \tag{6.3}$$

where *f(x)* is the probability density function of case A and *g(y)* the probability density function of case B.

6.3.2 Normal distribution

When the distributions can be described by a normal distribution $\underline{r}_A \sim N\left(\mu_{\underline{r}_A}, \sigma_{\underline{r}_A}\right)$ for case A and $\underline{r}_B \sim N\left(\mu_{\underline{r}_B}, \sigma_{\underline{r}_B}\right)$ for case B with an expected value μ and a standard deviation σ the probability of identification $P\left(\underline{r}_A > \underline{r}_B\right)$ can be obtained as follows.

Suppose $\underline{r}_A > \underline{r}_B$, this means that $\underline{r}_A - \underline{r}_B > 0$. We introduce a new random variable $\underline{r}_S$ which is defined as: $\underline{r}_S = \underline{r}_A - \underline{r}_B$ with an expected value $\mu_{\underline{r}_S} = \mu_{\underline{r}_A} - \mu_{\underline{r}_B}$ and a standard deviation $\sigma_{\underline{r}_S} = \sqrt{\sigma_{\underline{r}_A}{}^2 + \sigma_{\underline{r}_B}{}^2}$. This random variable is also normal distributed $\underline{r}_S \sim N\left(\mu_{\underline{r}_S}, \sigma_{\underline{r}_S}\right)$. This means that $P\left(\underline{r}_A > \underline{r}_B\right) = P\left(\underline{r}_S > 0\right)$. The probability that $\underline{r}_S > 0$ is found in the table for the standard normal distribution in combination with the *z*-value: $z = \left(l - \mu\right)/\sigma$ where *l* = limit value, in this case *l* = 0. So we get for *z*:

$$z = \frac{0 - \mu_{\underline{r}_S}}{\sigma_{\underline{r}_S}} = \frac{\mu_{\underline{r}_B} - \mu_{\underline{r}_A}}{\sqrt{\sigma_{\underline{r}_A}{}^2 + \sigma_{\underline{r}_B}{}^2}} \tag{6.4}$$

The probability $\underline{r}_S > 0$ can also be calculated by integrating the probability density function of $\underline{r}_S$ from 0 to +∞. The equation for the probability density function of the normal distribution is:

$$f\left(x\right) = \frac{1}{\sigma\sqrt{2\pi}} e^{-\frac{1}{2}\left(\frac{x-\mu}{\sigma}\right)^2} \quad -\infty < x, \mu < +\infty \quad \sigma > 0 \tag{6.5}$$

6.4 Identification by averaging

When both single shot distributions have an overlap but different expected values (Fig. 6.5) a 99.9% right identification can be achieved by averaging correlation coefficients $\bar{r} = \frac{1}{n}\sum_{i=1}^{n} r_i$ or averaging spectra $\bar{S}pectrum = \frac{1}{n}\sum_{i=1}^{n} Spectrum_i$ before correlating.

6.4.1 Gamma distribution

The Central Limit Theorem (CLT) states that the distribution of an average tends to be normal even when the initial distribution is not normal. Furthermore, this distribution has the same mean as the initial distribution and a standard deviation equal to the standard deviation of the initial distribution divided by the square root of the number of samples.

Fig. 6.6 shows multiple gamma distributions with the same expected value and a standard deviation reduced by $\sqrt{n}$. It is clear that the distribution of the mean has an increasing tend to a normal distribution at higher *n*. In that case, e.g. $n > 10$, the results obtained by calculating with the gamma distribution become the same as the results when using a normal distribution, so the normal distribution was used for the calculations.

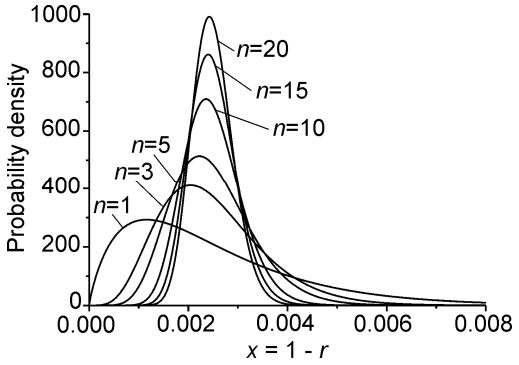

Fig. 6.6 Initial gamma distribution (n = 1) and the distributions of the mean when averaging n random variables

6.4.2 Normal distribution

The mean $\underline{\bar{x}}$ of a normal distributed random variable $\underline{x}$ has an expected value $\mu_{\underline{\bar{x}}}$ which is equal to the expected value of the single values $\mu_{\underline{x}}$, so $\mu_{\underline{\bar{x}}} = \mu_{\underline{x}}$. The standard deviation of the mean is a factor $1/\sqrt{n}$ smaller than the standard deviation of the single values. Thus, the distribution of the mean can be described by: $\underline{\bar{x}} \sim N\left(\mu_{\underline{x}}, \sigma_{\underline{x}} / \sqrt{n}\right)$. In case of two overlapping distributions with different expected values, the distribution of the means narrows with increasing

n and the overlap becomes smaller. What we do is to increase *n* until the probability $\left(\underline{\overline{r}}_A > \underline{\overline{r}}_B\right)$ is > 99.9% (Fig. 6.7).

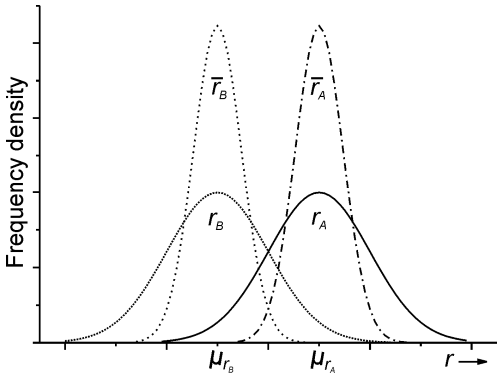

Fig. 6.7 Initial distributions and the distributions of the means when averaging n random values

The number of spectra or correlation coefficients to be averaged can be calculated as follows:

Suppose $\underline{\overline{r}}_A > \underline{\overline{r}}_B \Rightarrow \underline{\overline{r}}_A - \underline{\overline{r}}_B > 0$

and introduce a new variable: $\underline{\overline{r}}_S = \underline{\overline{r}}_A - \underline{\overline{r}}_B$

with expected value: $\mu_{\underline{\overline{r}}_S} = \mu_{\underline{r}_A} - \mu_{\underline{r}_B}$

and standard deviation: $\sigma_{\underline{\overline{r}}_S} = \sqrt{\frac{\sigma_{\underline{r}_A}{}^2}{n} + \frac{\sigma_{\underline{r}_B}{}^2}{n}}$

Substituting this in $z = \frac{l - \mu}{\sigma}$ and replacing $l = 0$, because $\underline{\overline{r}}_A - \underline{\overline{r}}_B > 0$ gives the required number of spectra to be averaged as:

$$n = z^2 \frac{\sigma_{\underline{r}_A}{}^2 + \sigma_{\underline{r}_B}{}^2}{\mu_{\underline{r}_A}{}^2 - 2\mu_{\underline{r}_A}\mu_{\underline{r}_B} + \mu_{\underline{r}_B}{}^2} \tag{6.6}$$

$z = 3$ is used for the calculations ($P\left(\underline{\overline{r}}_A > \underline{\overline{r}}_B\right) = 99{,}9\%$). For the calculations in the experimental section the expected value $\mu_{\underline{x}}$ is replaced by the sample

mean $\bar{x} = \frac{1}{n}\sum_{i=1}^{n} x_i$ and the standard deviation $\sigma_{\underline{x}}$ is replaced by the estimated standard deviation $S = \sqrt{\frac{\sum_{i=1}^{n}(x_i - \bar{x})^2}{n-1}}$.

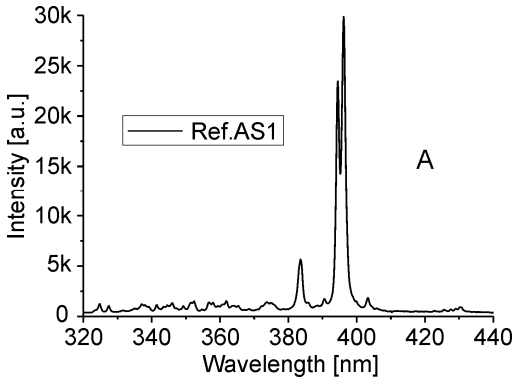

Fig. 6.8 Averaged spectra of one position used as reference for sample AS1

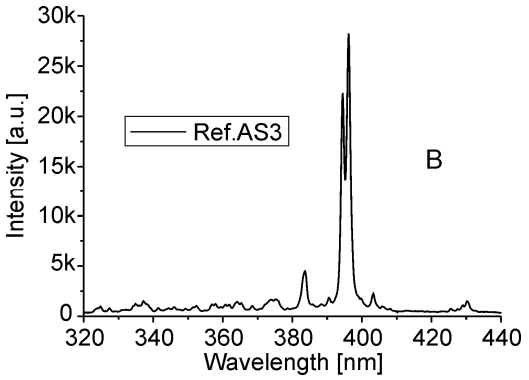

Fig. 6.9 Averaged spectra of one position used as reference for sample AS3

6.5 Results and discussion

Fig. 6.8 and Fig. 6.9 show the both used reference spectra. Case A describes spectra of sample AS1 correlated with Ref.AS1 and case B describes spectra of sample AS1 correlated with Ref.AS3. There is almost no visible difference

between the spectra of both samples. Nevertheless it is feasible to identify the samples by correlation analysis.

6.5.1 Single shot analysis

The correlation coefficients acquired by correlating the single shot spectra are shown in Fig. 6.10. In 57 of the 72 cases A was found higher than B, which means 79% positive identification. The distributions of A and B are shown in Fig. 6.11. As can be seen, the gamma functions fit well to the distributions. Estimating the probability that $\underline{r}_A > \underline{r}_B$ (raw data) by equation (6.3) gives: $P\left(\underline{r}_A > \underline{r}_B\right) = 85\%$. The accuracy of the predicted probability will increase with more data.

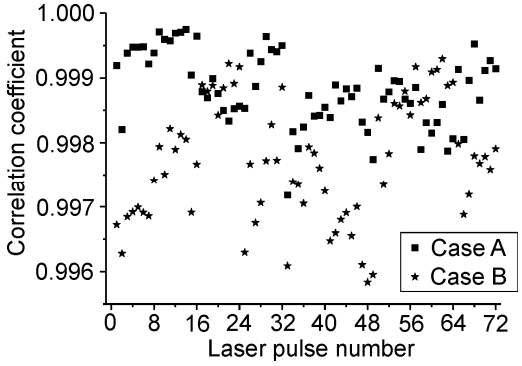

Fig. 6.10 Single shot correlation coefficients vs. laser pulse number for case A and B

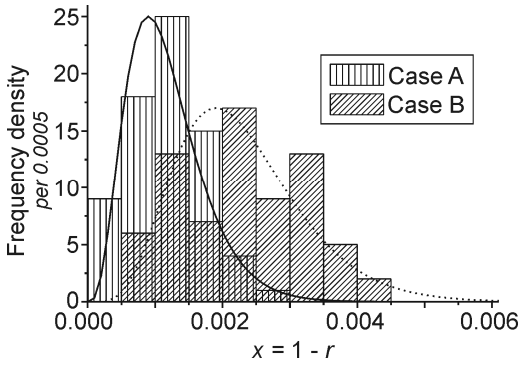

Fig. 6.11 Distribution of the single shot correlation coefficients for case A and B with fitted gamma

6.5.2 Averaged correlation analysis

In section 6.5.1 was shown that a correct identification was not always possible by single shot correlation analysis. The number of correlation coefficients to be averaged to achieve 99.9% probability can be calculated with equation (6.6) resulting in n = 9.

Fig. 6.12 shows the single shot distribution for case A and B (same as Fig. 6.11) and the distribution of the means for n = 9. The correlation coefficients of the first pulse on each position, pulse two of each position, etc. until pulse 8 for case A and B (8 pulses per position, 9 positions) have been averaged. These results (case A' and case B') are shown per pulse number in Fig. 6.13. Positive identification was obtained every time, case A'>case B'.

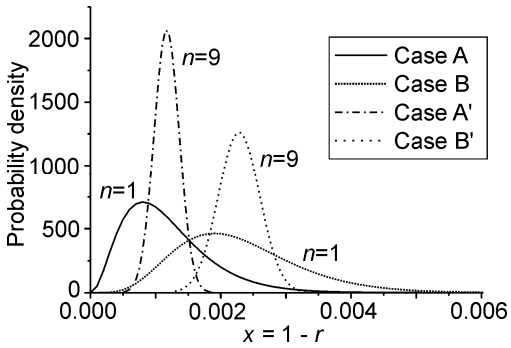

Fig. 6.12 Distribution of the single shot correlation coefficients for case A and B and the distributions of the mean when averaging 9 single shot correlation coefficients, case A' and B'

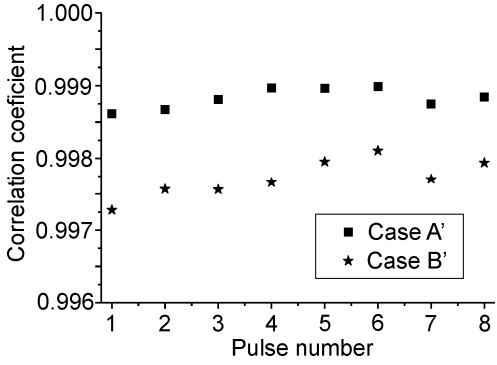

Fig. 6.13 Averaged single shot correlation coefficients vs. pulse number for case A' and B', each point represent an average of 9 correlation coefficients

6.5.3 Averaging correlation coefficients or spectra

During this work was found out that the deviation between two correlation coefficients, obtained by averaging spectra and then correlate this mean spectrum with both reference spectra, gives the same results as averaging the correlation coefficients, obtained from single spectra and than average the correlation coefficients. Fig. 6.14 shows correlation coefficients obtained by both methods. The deviations between two correlation coefficients calculated by the same method are indicated by *Δc* and *Δd* at two pulse numbers. Since the deviation between two correlation coefficients is equal regardless of which approach is used, equation (6.6) can also be applied to calculate the number of spectra to be averaged before correlating with the reference spectra to come to a correct identification.

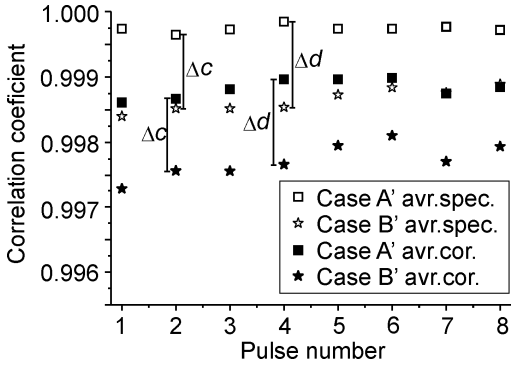

Fig. 6.14 Correlation coefficients obtained by averaging correlation coefficients and correlation coefficients obtained by averaging spectra before correlating vs. pulse number, Δc and Δd indicate the equal deviation achieved between the correlation coefficients per method

The advantage of correlating averaged spectra over averaging correlation coefficients is the calculation time in praxis. In case of averaging correlation coefficients there is a calculation for each correlation coefficient and one extra for averaging the correlation coefficients instead of two calculations when correlating averaged spectra. In this case one calculation for averaging the spectra and one for correlating this averaged spectrum is needed.

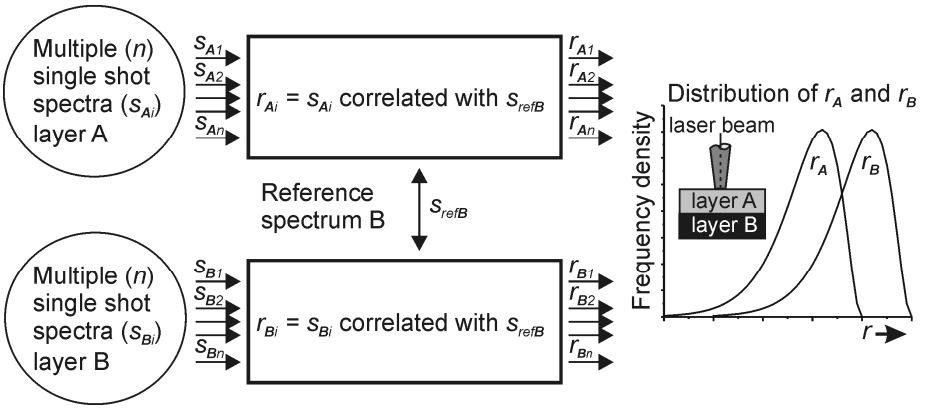

Fig. 6.15 Multiple single shot spectra of layer A and B correlated with the reference spectrum of layer B, both distributions show an overlap

6.6 Probability calculation and laser cleaning

During controlled laser cleaning the current spectrum is correlated with the reference spectrum of the layer to be preserved (layer B). In contrast to identification of “unknown” samples all spectra are correlated with this reference spectrum. For a successful process control the correlation coefficients belonging to the unwanted layer (A) have to be lower than the correlation coefficients affiliated to the layer to be preserved. Fig. 6.15 schematically shows the creation of both correlation coefficient distributions.

6.6.1 Probability of successful process control

The probabilities of correct decisions during ablating layer A and at the transition from layer A to layer B can be estimated by means of the correlation coefficient distributions of layer A and B and the value of the comparing criterion *C* (Fig. 6.16). The probability of a correct decision after each laser ablation pulse during ablating layer A (the process continues) is equal to $P\left(\underline{r_A} < C\right)$. Analog the probability of an incorrect decision (the process stops) is $P\left(\underline{r_A} > \mathrm{C}\right)$. The probability of a correct decision (the process stops) at the transition from layer A to layer B is equal to $P\left(\underline{r_B} > \mathrm{C}\right)$. Analog the probability of an incorrect decision at the transition (the process continues) is $P\left(\underline{r_B} < \mathrm{C}\right)$. These probabilities can be estimated by integrating the probability distribution function

or in case of a normal distribution also with the table of the standard normal distribution and the *z*-value: $z = (I - \mu)/\sigma$ where $I = C$.

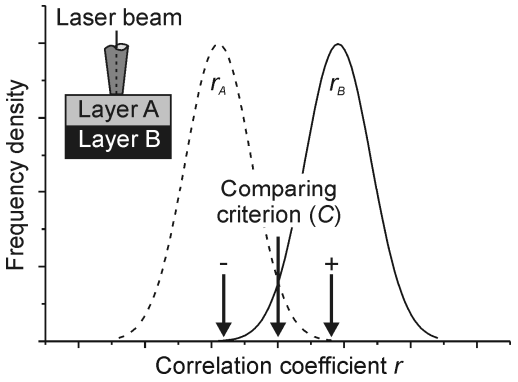

Fig. 6.16 The correlation coefficient distribution corresponding to layer A overlays with the distribution affiliated to layer B. In this case an ideal comparing criterion does not exist

From this follows that an optimal comparing criterion does not exist in case of overlapping distributions. Increasing the value of the comparing criterion increases the probability of correct decisions during ablating layer A but decreases the probability of a good decision at the transition (Fig. 6.16). Reverse, decreasing the value of the comparing criterion decreases the probability of correct decisions during ablating layer A and therewith increases the probability of a good decision at the transition (Fig. 6.16). The best is when both distributions do not overlap and the comparing criterion is in between the distributions (Fig. 4.12). In this case the highest probability of correct decisions will be obtained.

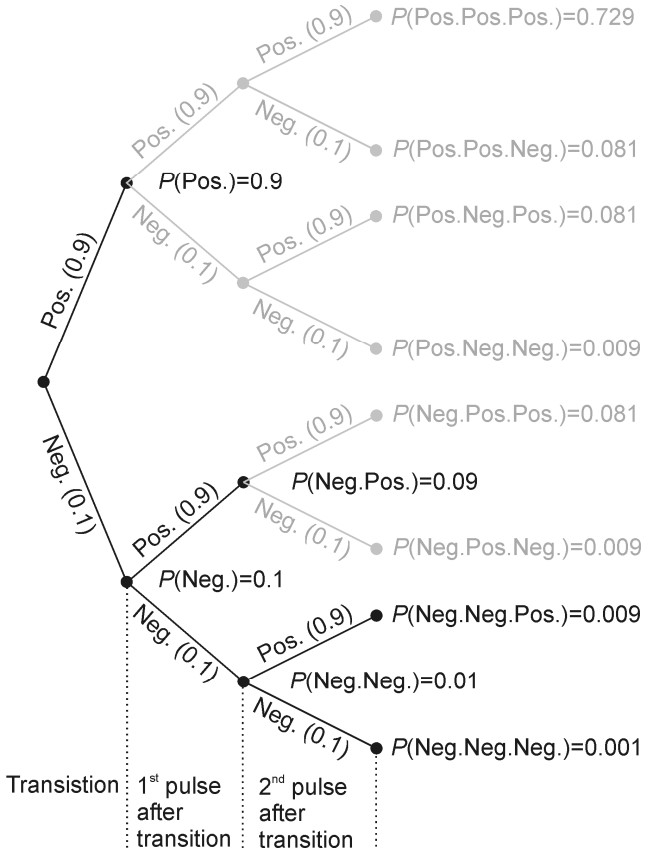

Fig. 6.17 Probability tree applied to estimate the probabilities of different possible results at the transition. The probability on a positive (0.9) or negative (0.1) outcome stays constant (experiment with replacement). The gray lines symbolize events that will not happen since a positive event stops the cleaning process

6.6.2 Probability trees

Probability trees can be applied to estimated and visualize the probabilities of consecutive events [84]. The probability tree in Fig. 6.17 shows by black lines the different consecutive events which can happen when reaching layer B. The gray lines illustrate events which cannot occur since a positive event stops the cleaning process. In this example $P\left(\underline{r_B} > \text{comparing criterion}\right) = 0.9$ (Pos.) and $P\left(\underline{r_B} < \text{comparing criterion}\right) = 0.1$ (Neg.). Thus, the probability of a correct decision at the transition is 0.9. Analog there is a 0.1 probability, that the

decision at the transition is incorrect. This causes a continuing of the cleaning process (over-cleaning). When the decision is incorrect there will be a next laser ablation pulse after which the decision “stop” or “continue” must be made again. The probabilities of consecutive events are calculated by multiplying the probabilities of the single decisions. For example the probability of a negative decision followed by a positive decision P(Neg.Pos.) is $0.1 \cdot 0.9 = 0.09$.

If the probability of an incorrect decision at the transition is >> 0 multiple laser pulses are generally needed to stop the process. This may be no problem for objects that permit a little distortion of the layer to be preserved, e.g. technical surfaces. In these cases controlling can occasionally reduce the amount of redundant laser pulses.

6.7 Conclusions

The presented work in this chapter shows that the probability of identification by correlation analysis can be estimated with the aid of the gamma or normal distribution, the sample mean and estimated standard deviation of the sample values. The prediction accuracy increases with the number of experimental data.

In case that a 99.9% probability of identification is not obtained by single shot correlation analysis the accuracy can be increased by averaging spectra. The number of spectra to be averaged for 99.9% probability can be calculated with the method described in this chapter.

The probabilities of correct decisions during laser cleaning can be estimated by means of the correlation coefficient distribution of the unwanted layer, the correlation coefficient distribution of the layer to be preserved and the value of the comparing criterion. If both distributions overlap an optimal comparing criterion does not exists. In this case the probability of consecutive events at the transition can be visualized and calculated by means of probability trees.

7 Plasma emission collecting arrangements

Basic ray propagation models are developed to simulate the propagation of the plasma emission through the collecting optics. These models give a better understanding of the influence of the collecting optics alignment on the emission detection efficiency. The propagation of the plasma emission rays through the collecting optics is geometrically approximated by ray transfer matrices. Due to the fact that the refraction index is wavelength dependent the ray propagation differs with wavelength. Therefore the form of the LIB-spectra can be shifted by changing the alignment of the collecting optics.

The models developed in this chapter are used to simulate the collecting efficiency as a function of wavelength for different alignments of the collecting optics. Furthermore the models provide information about the applicability of different collimators. In this thesis the applicability of two collimators is investigated for both laser systems: collimator-1 f = 10 mm, aperture radius 2.5 mm and collimator-2 f = 100 mm, aperture radius 12.7 mm.

As already described in chapter 3, the collimator and optical fibre are implemented in both optical set-ups (excimer and Nd:YAG) behind the last mirror. To simplify the ray propagation models the minor influence of this mirror on the ray propagation is neglected.

7.1 Beam - collimator - optical fibre couple efficiency

A collimator is used to couple the plasma light into an optical fibre. The couple efficiency depends on the applied collimator, the beam parameters at the collimator entrance and the fibre parameters (Fig. 7.1). In this basic model the couple efficiency is calculated by multiplying three area ratios:

- collimator area / beam area at collimator entrance ratio, $\eta_c = \frac{r_c^{\,2}}{r_{bc}^{\,2}}$
- fibre area / beam area at optical fibre entrance ratio, $\eta_{fi} = \frac{r_{fi}^{\,2}}{r_{bf}^{\,2}}$
- *NA* fibre² / *NA* collimator² ratio, $\eta_{NA} = \frac{NA_{fiber}^{\,2}}{NA_{coll}^{\,2}}$

where r_c is the collimator radius, r_{bc} the beam radius at the collimator entrance, r_{fi} the fibre core radius and r_{fc} the beam radius at the fibre entrance (r_{fi} = 300 µm). Thus, the beam - collimator - optical fibre couple efficiency reads:

$$\eta_{b-c-f} = \eta_c \eta_{fi} \eta_{NA} \tag{7.1}$$

The (single) efficiencies cannot exceed 1, if $\eta_i > 1$ then $\eta_i = 1$. This model assumes the light beam has a homogeneous intensity distribution and the fibre entrance is one nominal focal length behind the collimator. The wavelength dependent collimator focal length variation and the wavelength dependent *NA* variation of the fibre (NA_{fibre} = 0.22) are neglected.

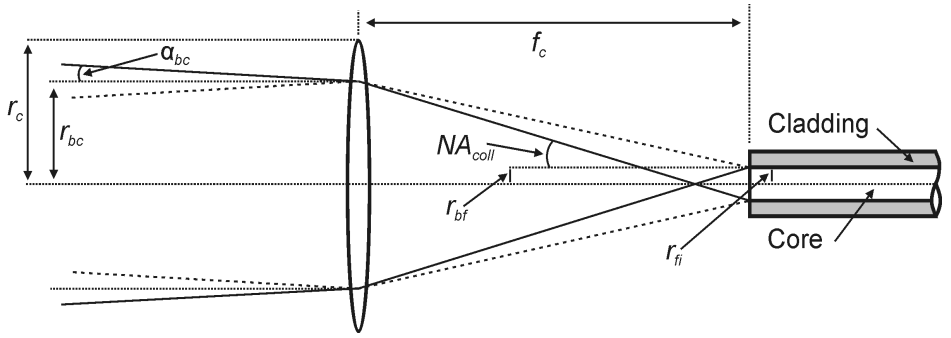

Fig. 7.1 The outer rays define the NA of the collimator and the radius at the optical fibre entrance

The emission beam radius at the fibre entrance depends on the collimator focal length (f_c) and the angle (α_{pc}) of the outer rays passing through the collimator (if $r_{bc} \le r_c$ then $\alpha_{pc} = \alpha_{bc}$, else $\alpha_{pc} \neq \alpha_{bc}$):

$$r_{bf} = f_c \left| \alpha_{pc} \right| \tag{7.2}$$

α_{bc} is the angle of the outer rays of the beam to be coupled at the collimator entrance plane.

The angle of the outer rays behind the collimator and therewith the *NA* of the collimator depends on: the collimator focal length, the angle of the outer rays passing through the collimator and the radius of the beam (r_{pc}) passing through the collimator area (if $r_{bc} \le r_c$ then $r_{pc} = r_{bc}$, else $r_{pc} = r_c$):

$$NA_{coll} = \left| -\frac{r_{pc}}{f_c} + \alpha_{pc} \right| \tag{7.3}$$

Equation (7.2) and (7.3) are derived from following matrix equation:

$$\begin{pmatrix} r_{bf} \\ NA_{coll} \end{pmatrix} = \begin{pmatrix} 1 & f \\ 0 & 1 \end{pmatrix} \begin{pmatrix} 1 & 0 \\ -\frac{1}{f_c} & 1 \end{pmatrix} \begin{pmatrix} r_{pc} \\ \alpha_{pc} \end{pmatrix} \rightarrow \begin{pmatrix} f_c \alpha_{pc} \\ -\frac{r_{pc}}{f} + \alpha_{pc} \end{pmatrix}$$

Depending on the beam to be collected a suitable collimator type has to be chosen. In general collimators with a shorter focal length have a higher *NA* and constitute a smaller beam radius one focal length behind the collimator (if the ray entrance angle > 0) in comparison to collimators with longer focal lengths. The advantage of collimators with longer focal length is generally their higher collecting efficiency due to the larger aperture radius at equal f-number.

7.2 Collecting arrangements, excimer laser

7.2.1 Model

In the excimer imaging set-up one lens projects the laser radiation on the object surface, s. Fig. 3.1. Together with the collimator and the optical fibre this lens forms the plasma emission collecting set-up (Fig. 7.2).

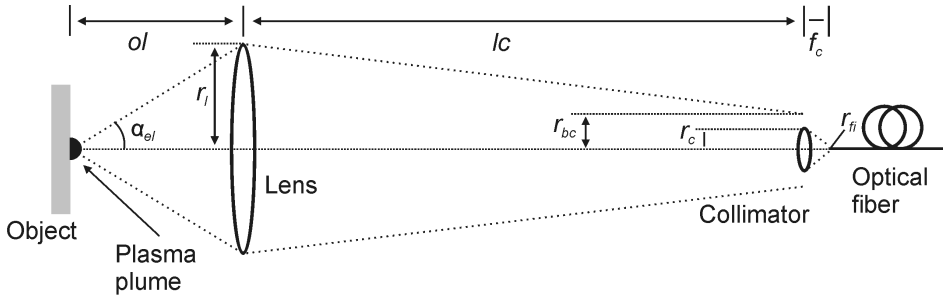

Fig. 7.2 Basic model of the outer plasma emission rays propagating through the collecting set-up (excimer laser)

In this basic model the plasma emission is assumed to be a point source at the object interaction area, as shown in Fig. 7.3. The collecting efficiency (η_{el}) of the projection lens depends on the lens area and the object lens distance (*ol*) and can be estimated from the ratio: lens area to area of the half sphere *ol* away from the object:

$$\eta_{el} = \frac{\pi r_l^2}{2\pi ol^2} \tag{7.4}$$

where r_l is the effective radius of the projection lens (r_l = 19 mm).

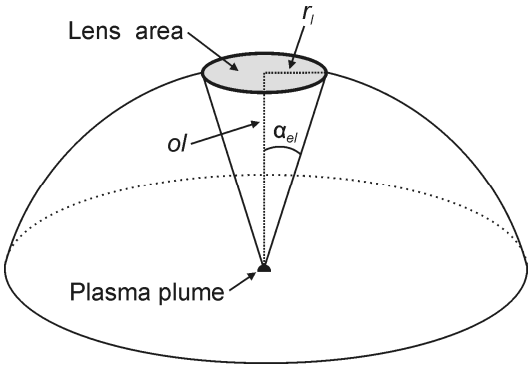

Fig. 7.3 The emitting plasma is assumed to be a radiating spherical point source

The wavelength dependent collecting efficiency of the plasma emission collecting set-up is calculated by multiplying the projection lens collecting efficiency with the wavelength dependent beam - collimator - optical fibre couple efficiency:

$$\eta(\lambda) = \eta_{el}\eta_{b-c-f}(\lambda) \tag{7.5}$$

Since the focal length of a lens is wavelength dependent the plasma emission ray propagation through the collection optics also varies with wavelength. The wavelength dependent focal lengths can be found in Appendix B. The emission beam radius (r_{bc}) and the angle (α_{bc}) of the outer rays at the collimator entrance plane, needed to calculate the beam - collimator - optical fibre couple efficiency, are calculated (in this model) with ray transfer matrices as follows:

$$\begin{pmatrix} r_{bc} \\ \alpha_{bc} \end{pmatrix} = \begin{pmatrix} 1 & lc \\ 0 & 1 \end{pmatrix} \begin{pmatrix} 1 & 0 \\ -\dfrac{1}{f_l(\lambda)} & 1 \end{pmatrix} \begin{pmatrix} 1 & ol \\ 0 & 1 \end{pmatrix} \begin{pmatrix} r_e \\ \alpha_{el} \end{pmatrix} \tag{7.6}$$

where $r_e = 0$ is the radius of the point source at the object, α_{el} the angle of the outer emission rays passing through the lens, $f_l(\lambda)$ the wavelength dependent focal length of the projection lens and lc the lens collimator distance.

In case the emission beam radius at the collimator entrance is larger as the collimator radius ($r_{bc} > r_c$) the angle (α_{pc}) of the outer rays passing through the collimator has to be calculated. Since the radius of the beam passing through the collimator cannot exceeds the collimator radius, r_{bc} is substituted by r_c. From equation (7.6) can be derived that:

$$r_c = \left(olf_l(\lambda) - olc + lcf_l(\lambda)\right)\frac{\alpha_{new}}{f_l(\lambda)} \tag{7.7}$$

and

$$\alpha_{pc} = \left(-ol + f_l(\lambda)\right)\left(\frac{\alpha_{new}}{f_l(\lambda)}\right). \tag{7.8}$$

α_{pc} can now be calculated by dissolving equation (7.7) to α_{new} and substituting this new starting angle in equation (7.8).

7.2.2 Numerical calculations

With the described model the propagation of the outer plasma emission rays and the collecting efficiency for different alignments of the collecting optics are simulated per wavelength. Fig. 7.4 shows the simulated propagation (equation (7.6)) of the outer plasma emission rays after the projection lens for four different wavelengths. The object lens distance was chosen 154 mm and the lens collimator distance 556 mm, since these distances were frequently used in

the practical experiments. The radius of the emission beam at the collimator entrance plane increases with increasing wavelength.

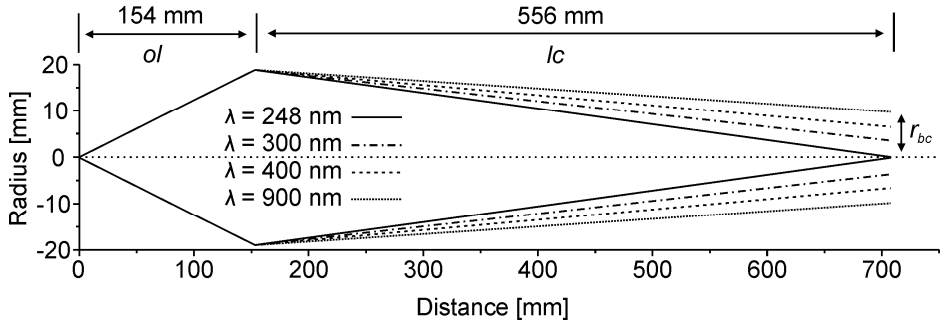

Fig. 7.4 Simulated propagation of the outer emission rays of different wavelengths

As already mentioned, the collecting efficiency depends on the applied optics, alignment of the optics and the wavelength of the rays. Fig. 7.5 shows the by equation (7.5) simulated efficiencies for the two collimator types versus object lens distance for 6 different wavelengths. The lens collimator distance was 556 mm. This simulation predicts, that when working with object lens distances > 150 mm, the f = 10 mm collimator affects higher collecting efficiencies than the f = 100 mm collimator. In practice the object lens distance was > 150 mm. Based on this information there was chosen to buy only the f = 10 mm collimator. From Fig. 7.5 can also be obtained that a variation of the object lens distance has a wavelength dependent influence.

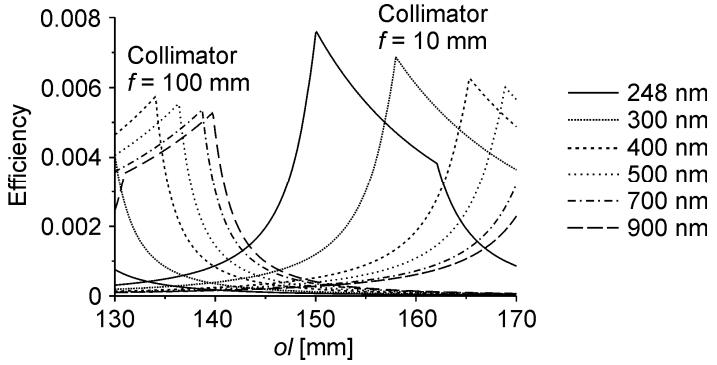

Fig. 7.5 Simulated efficiencies versus object lens distance for both collimators. Lens collimator distance = 556 mm

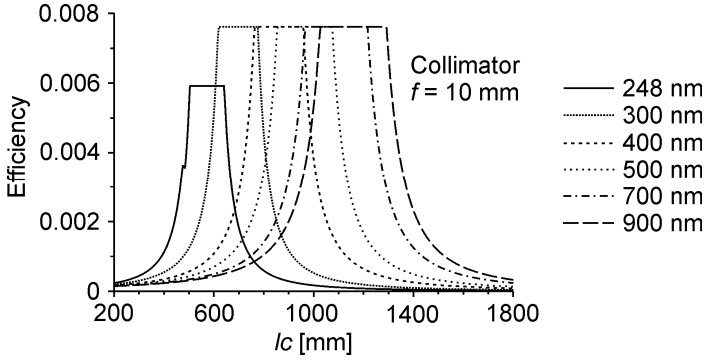

Fig. 7.6 Simulated efficiencies versus lens collimator distance for the f = 10 mm collimator, object lens distance = 154 mm

Fig. 7.6 shows the by equation (7.5) simulated collecting efficiencies versus lens collimator distance at constant object lens distance of 556 mm for the *f* = 10 mm collimator. From this simulation can be obtained that the optimum lens collimator distance is strongly wavelength dependent. With increasing *lc* the collecting efficiency for longer wavelengths increase and the collecting efficiency for shorter wavelengths already decrease. The horizontal parts result from the intervals *lc,* wherein the (emission beam) radius at the collimator entrance plane is smaller or equal to the aperture radius of the collimator.

7.2.3 Experimental validation

An adjustment of the projection set-up varies the energy density on the surface and causes a variation of the plasma emission parameters. According to this, only a validation of the lens collimator distance variation model could be accomplished with LIB-spectra. In this case the energy density on the surface stays constant. Nevertheless, a validation of the models was achieved by applying a stable broadband radiating source instead of the plasma.

For the validation of the models the plasma was replaced with a stabilized deuterium-halogen lamp applied in combination with an optical fibre (Ø 200 µm) as broadband radiating cone source. The light source completely illuminated the first lens. The end of the optical fibre was positioned coaxial with respect to the optical axes of the collecting system in the object plane. The constant emission spectra of the lamp were measured at different alignments of the collecting optics. By dividing the measured spectrum of one setting by the spectrum of

another setting the intensity increment as function of wavelength was obtained. These results are compared with the simulated wavelength dependent increments for the same alignment variation.

The object lens distance variation simulation is additionally validated with recorded LIB-spectra. Per setting (*lc* = 556 mm and *lc* = 596 mm) 10 spectra were acquired and averaged. The average spectrum of one object lens distance was divided by the average spectrum of another object lens distance, to obtain the intensity increment as function of wavelength. Again the results were compared with the simulated wavelength dependent increments. The applied experimental parameters were: λ = 248 nm, E_{pulse} = 22 mJ, focal area = 2.37 mm², *ol* = 154 mm, no delay between laser pulse and plasma acquisition and the sample was blue-paper (section 4.5).

The simulated wavelength depended intensity increments were calculated by dividing the calculated wavelength dependent efficiencies of two collecting optics alignments. These wavelength dependent efficiencies per alignment were in turn calculated by equation (7.5). The wavelength dependent focal lengths can be obtained from Appendix B.

Object lens distance variation

Fig. 7.7 shows 2 deuterium-halogen spectra acquired with different object lens distances. The spectral intensity increased over the complete bandwidth, with the exception of wavelengths shorter than ≈ 325 nm, when increasing the object lens distance form 154 to 160 mm. The wavelength dependent intensity increments are shown in Fig. 7.8. These were obtained by dividing the *ol* = 160 mm spectrum by the *ol* = 154 mm spectrum. The form of this graph agrees with the simulation, see the dotted line. The slight deviation can be declared with; the simplification of the model, uncertainties in the distance measurements and manufacturer specifications.

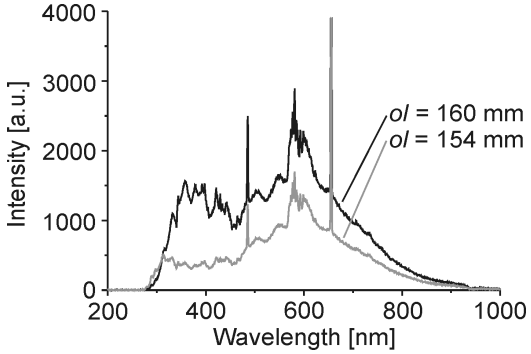

Fig. 7.7 Deuterium-halogen spectra recorded with an object lens distance of 154 mm and 160 mm (lc = 556 mm)

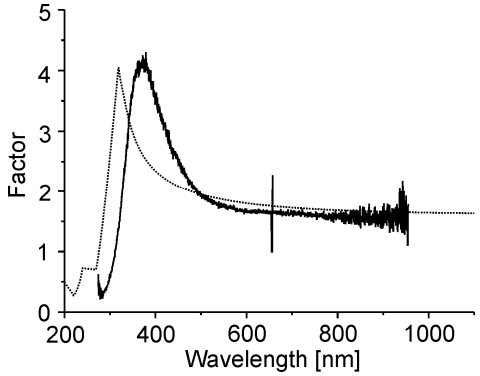

Fig. 7.8 Deuterium-halogen spectrum with ol = 160 mm divided by the deuterium-halogen spectra with ol = 154 mm, dotted line indicates the simulation

Lens collimator distance variation

Fig. 7.9 shows 2 deuterium-halogen spectra acquired with different lens collimator distances. With increasing lens collimator distance the intensities increased over the complete bandwidth, with the exception of wavelengths shorter than ≈ 300 nm. Fig. 7.10 shows the wavelength dependent intensity increments for increasing the lens collimator distance form 556 to 596 mm. These were obtained by dividing the *lc* = 596 mm spectrum by the *lc* = 556 mm spectrum. The form of this graph agrees with the simulation, see dotted line. The deviation can be explained by the simplification of the model, uncertainties in the distance measurements and manufacturer specifications.

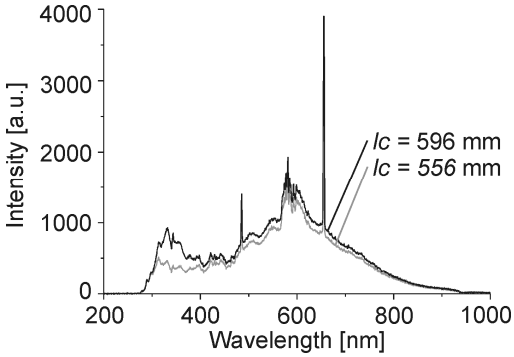

Fig. 7.9 Deuterium-halogen spectra recorded with a lens collimator distance of 556 mm and 596 mm (ol = 154 mm)

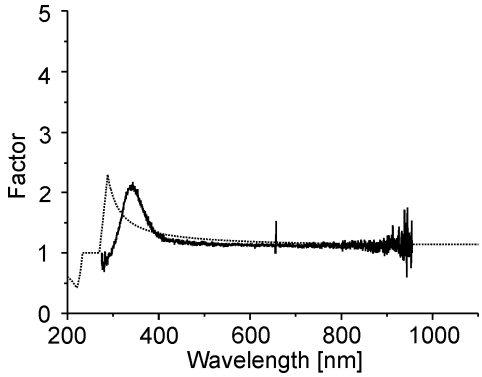

Fig. 7.10 Deuterium-halogen spectrum recorded with lc = 596 mm divided by the LIB-spectrum recorded with lc = 556 mm, the dotted line indicates the simulation

Fig. 7.11 shows two LIB-spectra of blue-paper recorded at different lens collimator distances. The *lc* = 596 mm spectrum shows an intensity increase over the complete bandwidth with respect to the *lc* = 556 mm spectrum. The wavelength dependent intensity increments for increasing the lens collimator distance form 556 mm to 596 mm are shown in Fig. 7.12. The form of the graph agrees with the deuterium-halogen intensity increment graph (Fig. 7.10). However, in contrast to the deuterium-halogen results the factors are lower in the 300…425 nm interval. This is expected to be caused by the low spectral intensities and noise in this interval. Furthermore, the spectral fluctuations of both adjustments overlapped.

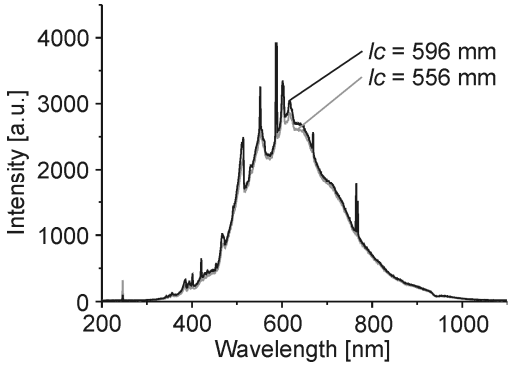

Fig. 7.11 Average LIB-spectra of blue-paper recorded with a lens collimator distance of 556 mm and 596 mm (ol = 154 mm)

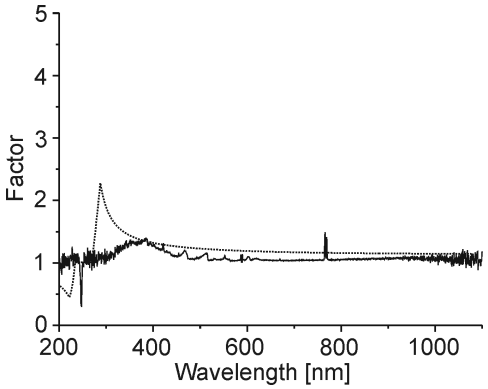

Fig. 7.12 Average LIB-spectrum recorded with lc = 596 mm divided by the average LIB-spectrum recorded with lc = 556 mm

7.3 Collecting arrangements, Nd:YAG cleaning laser

7.3.1 Model

The hand piece of the articulated arm is equipped with a telescope. This telescope forms with the collimator and optical fibre the plasma emission collecting set-up of the Nd:YAG cleaning laser, Fig. 7.13.

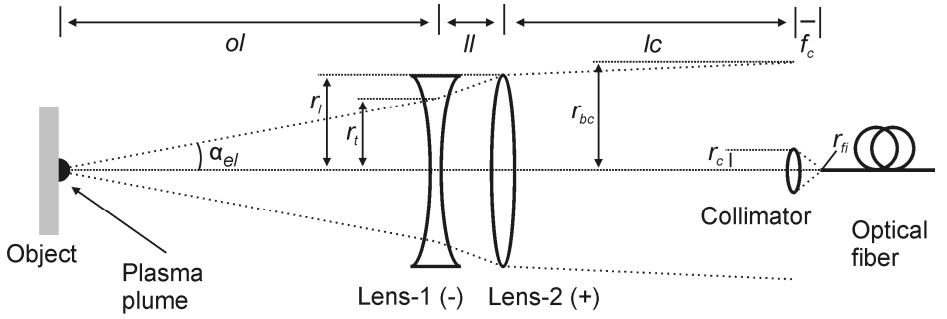

Fig. 7.13 Basic model of the outer plasma emission rays propagating through the collecting set-up (Nd:YAG laser)

Just as in the excimer model, the plasma emission is assumed to be a point source radiating half spherical, Fig. 7.3. In this model the collecting efficiency of the telescope is defined as the ratio: area of the emission beam passing both lenses (*ol* away from the object) to area of the half sphere *ol* away from the object. In equation form:

$$\eta_t = \frac{\pi r_t^2}{2\pi ol^2} \tag{7.9}$$

where r_t is the radius of the emission beam passing through both lenses at the first lens ($r_t = r(ol)$) and *ol* the object lens-1 distance. r_t can be calculated by:

$$r_t = \alpha_{el} ol \tag{7.10}$$

with

$$\alpha_{el} = \frac{r_l f_1(\lambda)}{ol f_1(\lambda) - ol ll + ll f_1(\lambda)} \tag{7.11}$$

Equation (7.11) is derived from:

$$\begin{pmatrix} r(ol+ll) \\ \alpha(ol+ll) \end{pmatrix} = \begin{pmatrix} 1 & ll \\ 0 & 1 \end{pmatrix} \begin{pmatrix} 1 & 0 \\ -\frac{1}{f_1(\lambda)} & 1 \end{pmatrix} \begin{pmatrix} 1 & ol \\ 0 & 1 \end{pmatrix} \begin{pmatrix} r_e \\ \alpha_{el} \end{pmatrix} \tag{7.12}$$

$$r_l = r(ol+ll)$$

where $r_e = 0$ is the radius of the point source at the object, α_{el} the angle of the outer emission rays passing both lenses, $f_1(\lambda)$ the wavelength dependent focal length of the first lens, *ll* the distance between the first and second lens and r_l the effective radius of both lenses (r_l = 11.65 mm).

The wavelength dependent collecting efficiency of the plasma emission collecting set-up is calculated by multiplying the collecting efficiency of the telescope with the beam - collimator - optical fibre couple efficiency:

$$\eta(\lambda) = \eta_t(\lambda)\eta_{b-c-f}(\lambda) \tag{7.13}$$

The emission beam radius (r_{bc}) and the angle (α_{bc}) of the outer rays at the collimator entrance plane, needed to calculate the beam - collimator - optical fibre couple efficiency, are calculated on the basis of this model with ray transfer matrices as follows:

$$\begin{pmatrix} r_{bc} \\ \alpha_{bc} \end{pmatrix} = \begin{pmatrix} 1 & lc \\ 0 & 1 \end{pmatrix} \begin{pmatrix} 1 & o \\ -\dfrac{1}{f_2(\lambda)} & 1 \end{pmatrix} \begin{pmatrix} 1 & ll \\ o & l \end{pmatrix} \begin{pmatrix} 1 & 0 \\ -\dfrac{1}{f_l(\lambda)} & 1 \end{pmatrix} \begin{pmatrix} 1 & ol \\ 0 & 1 \end{pmatrix} \begin{pmatrix} r_e \\ \alpha_{el} \end{pmatrix} \tag{7.14}$$

where $f_2(\lambda)$ is the wavelength dependent focal length of the second lens and *lc* the distance between the second lens and the collimator (*lc* = 237 mm).

In case the emission beam radius at the collimator entrance is larger as the collimator radius ($r_{bc} > r_c$) the angle (α_{pc}) of the outer rays passing through the collimator has to be calculated. Since the radius of the beam passing through the collimator cannot exceeds the collimator radius, r_{bc} is substituted by r_c. From equation (7.14) can be derived that:

$$r_c = \begin{pmatrix} olf_1(\lambda)f_2(\lambda) - ollcf_1(\lambda) - olllf_2(\lambda) + olllc - ollcf_2(\lambda) \\ +llf_1(\lambda)f_2(\lambda) - llf_1(\lambda)lc + lcf_1(\lambda)f_2(\lambda) \end{pmatrix} \frac{\alpha_{new}}{f_1(\lambda)f_2(\lambda)} \tag{7.15}$$

and

$$\alpha_{pc} = \left(olll - olf_1(\lambda) - olf_2(\lambda) - llf_1(\lambda) + f_1(\lambda)f_2(\lambda)\right)\frac{\alpha_{new}}{f_1(\lambda)f_2(\lambda)} \tag{7.16}$$

α_{pc} can now be calculated by dissolving equation (7.15) to α_{new} and substituting this new starting angle in equation (7.16).

7.3.2 Numerical calculations

Equation (7.10), (7.11), (7.12) and (7.14) are applied to simulate the beam propagation of the outer emission rays. The object lens distance is chosen 300 mm which is a practical value. The value of *lc* and *ll* are defined by the construction of the hand piece. Fig. 7.14 shows the propagation of the outer rays passing both lenses for the minimum feasible lens-1 lens-2 distance (3 mm). This simulation shows that the rays of the different wavelengths nearly

coincide. Fig. 7.15 shows the propagation of the outer rays passing both lenses for the maximum feasible lens-1 lens-2 distance (21 mm). It is visible that the difference between the wavelength dependent ray propagation increases with increasing lens-1 lens-2 distance. The wavelength dependent focal lengths can be found in Appendix B.

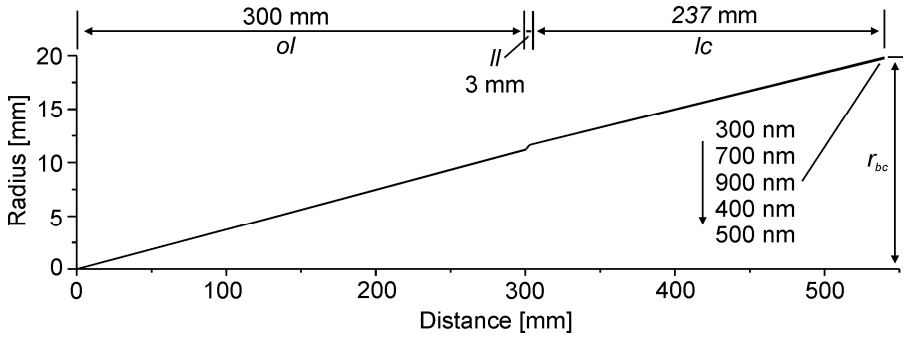

Fig. 7.14 Propagation of the outer emission rays passing both lenses (ll = 3 mm)

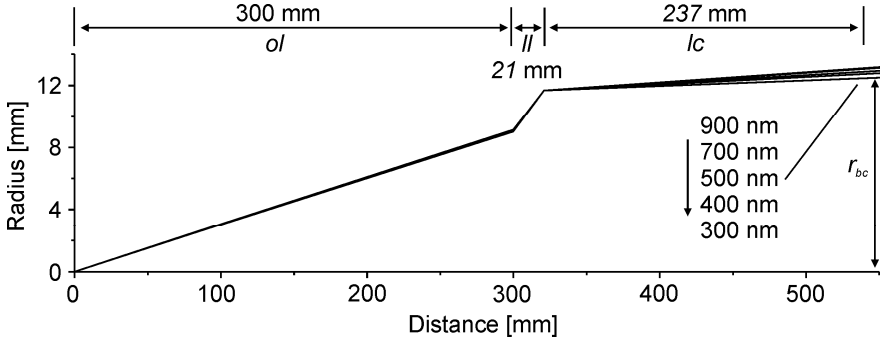

Fig. 7.15 Propagation of the outer emission rays passing both lenses (ll = 21 mm)

The wavelength dependent collecting efficiencies are simulated with equation (7.13) for the two different collimators. As result of implementing the *f* = 100 mm collimator into the hand piece its effective aperture radius mechanically decreases from 12.5 mm to 5.5 mm. Fig. 1 shows the simulation for *ll* = 3 mm and Fig 2 for *ll* = 21 mm.

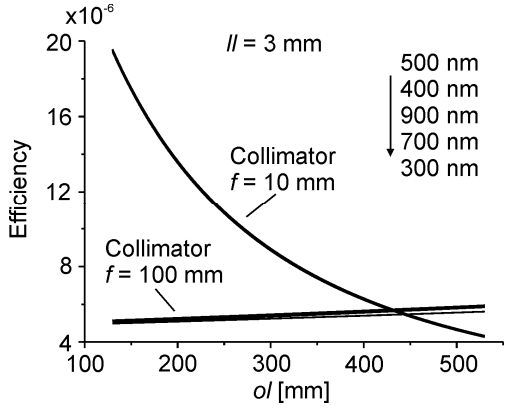

Fig. 7.16 Simulated efficiencies versus object lens distance for both collimators and different wavelengths (ll = 3 mm)

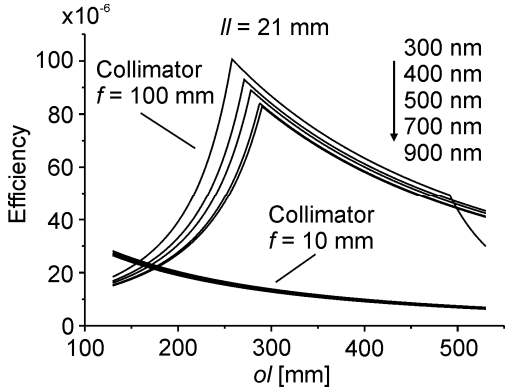

Fig. 7.17 Simulated efficiencies versus object lens distance for both collimators and different wavelengths (ll = 21 mm)

The *f* = 10 mm collimator causes higher intensities at the fibre entrance than the *f* = 100 mm collimator when *ll* = 3 mm. In case of *ll* = 21 mm the collecting efficiencies profit by the *f* = 100 mm collimator. In comparison to the excimer set-up the influence of an object lens distance variation is not significantly wavelength dependent.

7.3.3 Experimental validation

The validation of the Nd:YAG model was achieved by the same methods as applied for the excimer laser model, described in 7.2.3. For *ll* = 21 mm only the

method with the deuterium-halogen light source was applied, since an adjustment of the object lens distance caused a significant energy density variation. The experimental parameters for the LIB-spectra (*ll* = 3 mm) were: λ = 1064 nm, E_{pulse} = 606 mJ, 0.21 cm² focal area for *ol* = 300 mm, 0.20 cm² focal area for *ol* = 350 mm, no delay between laser pulse and plasma emission acquisition and the sample was an aluminum alloy.

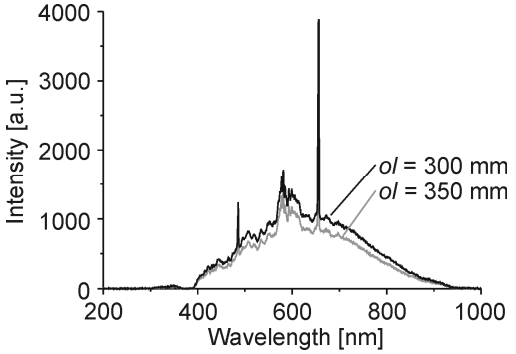

Fig. 7.18 Deuterium-halogen spectra recorded with an object lens distance of 300 and 350 mm (ll = 3 mm)

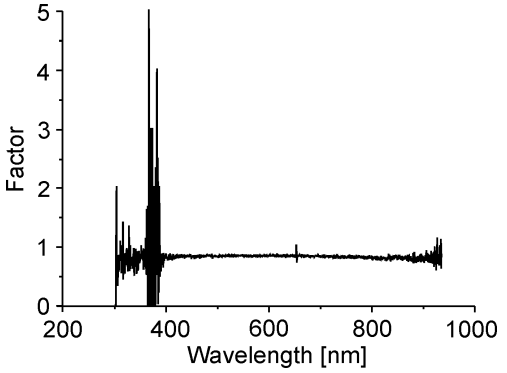

Fig. 7.19 Deuterium-halogen spectrum recorded with ol = 350 mm divided by the Deuterium-halogen spectrum recorded with ol = 300 mm

Fig. 7.18 shows 2 deuterium-halogen spectra acquired with different object lens distances. The spectral intensity decreased over the complete bandwidth, when increasing the object lens distance from 300 mm to 350 mm. The wavelength dependent intensity increments are shown in Fig. 7.19. The noise at ≈ 375 nm

was caused by the low transmission of the collecting optics at these wavelengths. The wavelength dependent intensity increments are obtained by dividing the *ol* = 350 mm spectrum by the *ol* = 300 mm spectrum. It can be clearly seen, that the influence of a variation was not significantly wavelength dependent. This agrees with the results displayed in Fig. 7.16. The same results were obtained for *ll* = 21 mm, these are not displayed in this thesis.

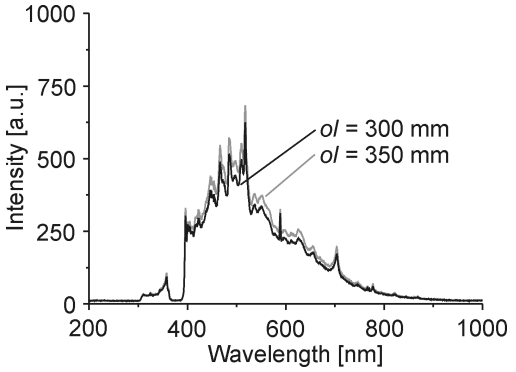

Fig. 7.20 LIB-spectra of AC13 recorded with an object lens distance of 300 mm and 350 mm (ll = 3 mm)

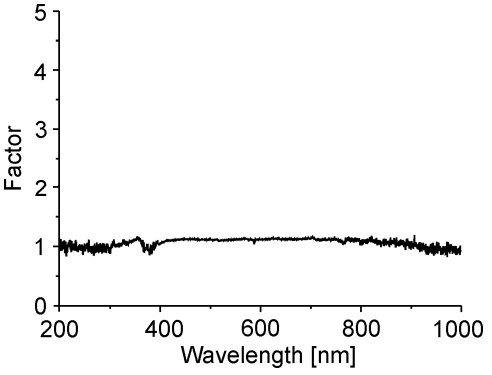

Fig. 7.21 LIB-spectrum recorded with ol = 350 mm divided by the LIB-spectrum recorded with ol = 300 mm

Fig. 7.20 shows two LIB-spectra of the aluminum alloy sample recorded with different object lens distances. According to the model, the spectral intensities should decrease by a constant factor when increasing the object lens distance

from 300 mm to 350 mm. However, the acquired plasma emission intensities increased (by a constant factor) due to the increased energy density at the surface. The wavelength dependent intensity increments for increasing the object lens distance from 300 mm to 350 mm are shown in Fig. 7.21. The upwards shift, in comparison to the simulation, is thus caused by the increased plasma emission intensity.

7.4 Conclusions and discussion

The simulations in this chapter show that the wavelength dependent influence of the collecting optics alignment can be simulated by basic models. If the collecting set-up consists of irradiation set-up components, the alignment of the collecting optics cannot be chosen arbitrarily. In this case the plasma emission detection efficiency can be optimized by the choice of an appropriate collimator. The beam – collimator – optical fibre couple efficiency depends on the following parameters:

- diameter of the beam to be coupled
- divergence or convergence of the beam to be coupled
- collimator aperture radius
- collimator focal length
- collimator lens material
- optical fibre diameter
- *NA* of the optical fibre

The beam – collimator – optical fibre couple efficiency can be estimated with the method described in this chapter.

In case the beam to be coupled is parallel, the advantage of a collimator with longer focal length is its higher emission collecting efficiency due to the larger aperture radius at equal f-number. However, if the ray entrance angle > 0 collimators with a shorter focal length have the advantage that they constitute a smaller beam radius one nominal focal length behind the collimator than collimators with a longer focal length. Summarizing, the collimator to be applied has to be adapted to the properties of the used set-up to achieve an optimal coupling efficiency.

8 Controlled laser cleaning in practice

For laser cleaning of artworks, lasers with manual- or computer-controlled beam delivery are applied. The computer controlled beam delivery includes for example a translation stage and scanner optic. The articulated beam delivery usually exists of an optical fibre or mirror arm with hand piece. This chapter is about the practical implementation of the technique described in chapter 4.

In section 8.1 the implementation in a KrF-excimer laser system with translation stage is described. Section 8.2 presents the implementation in a Nd:YAG cleaning laser with articulated mirror arm.

8.1 KrF-excimer system with translation stage

The correlation process has been automated in a closed-loop control system which was able to clean a predefined area automatically. The correlation coefficient was estimated after each laser pulse by correlating the current spectrum with the reference spectrum. When this value exceeded the value of the pre-defined compare criterion the ablation process was paused and the translation stage moved the sample to the next position. The cleaning process resumed until the correlation coefficient again exceeded the criterion, etc. This process repeated until the predefined area was completely cleaned. The areas were cleaned with a meander movement of the samples (Fig. 8.1). In this example the spot size is 1.5 x 1.5 mm^2 and the area to be cleaned is 4.5 x 6 mm^2 which results in a spot array of 3 x 4.

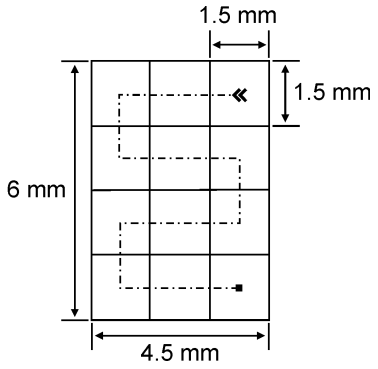

Fig. 8.1 Visualization of the meander movement of the translation stage

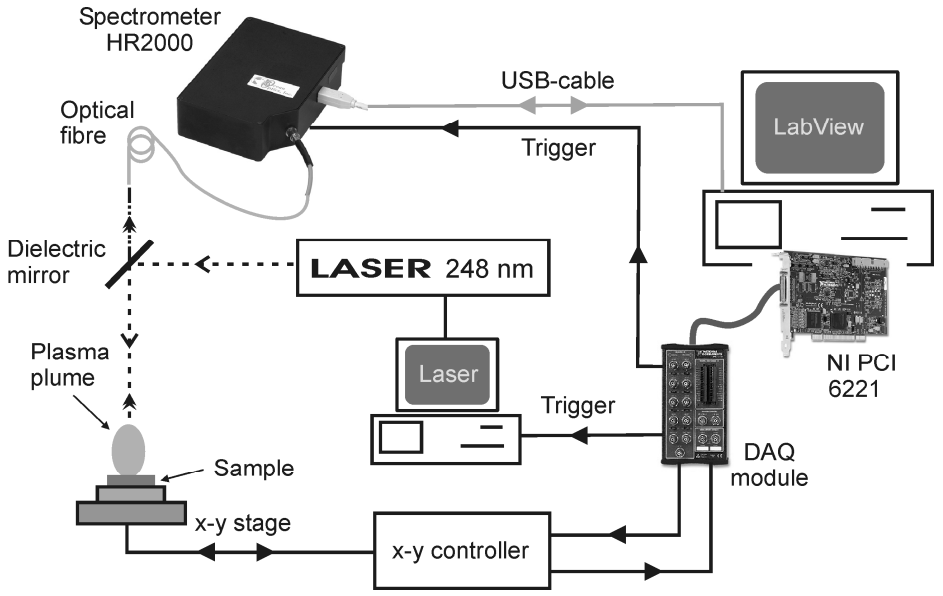

Fig. 8.2 Schematic visualization of the electronic communication set-up for controlled laser cleaning

8.1.1 Experimental set-up

All components in the KrF-excimer laser set-up were directly or indirectly connected with the controller PC (Fig. 8.2). The applied components are described in section 3.1.1 and 3.2.1.

The closed-loop process was controlled by in LabView written software. The area to be cleaned and the laser spot size were programmed on the x-y stage

controller. After entering the relevant data, the x-y stage controller was waiting for an input signal from the controller PC. After each input signal the stage moved to a new position until the pre-defined area was completely cleaned. When this situation was reached the x-y stage controller set the output channel on a high level. The laser parameters for cleaning were directly entered in the controller of the laser.

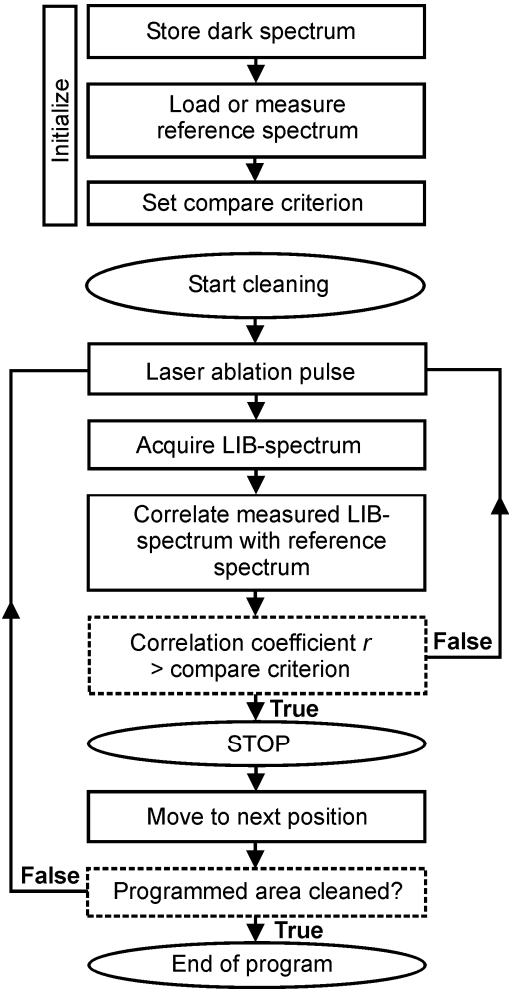

Fig. 8.3 Flow diagram of controlled laser cleaning with translation stage

8.1.2 Software and control

The sequence of the written software is shown in Fig. 8.3. In the initialization phase the reference spectrum is measured or loaded and the compare criterion is chosen.

Fig. 8.4 shows a screenshot of the user interface. The top left graph shows the measured spectrum and the lower left graph shows the applied reference spectrum. On the right, in the graph in the center, a scatter diagram shows the correlation between the current spectrum and the reference spectrum. The current correlation coefficient and the comparing criterion are displayed in the middle left.

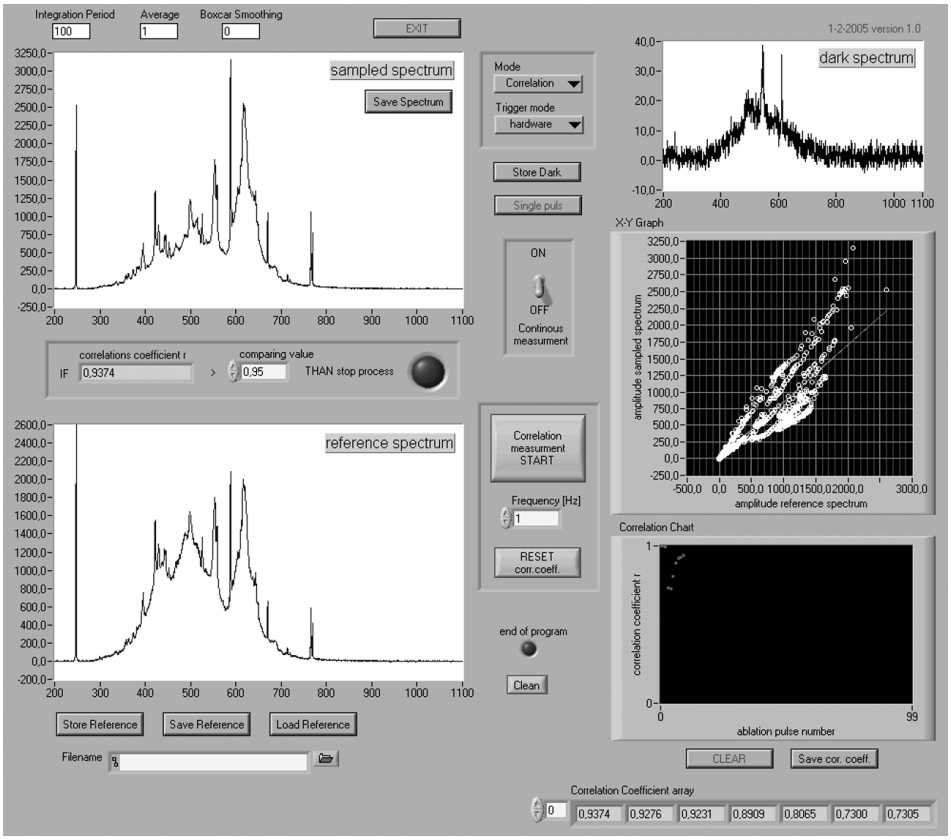

Fig. 8.4 User interface of the LabView program for controlled laser cleaning with translation stage

The delay between laser pulse and acquiring a plasma emission spectrum could be set by software (in combination with the DAQ-card) in 500 ns steps with a jitter of 10 ns from 0 to 20 µs. The applicable pulse frequency ranged from 1 to 10 Hz.

8.1.3 Results

Controlled laser cleaning was tested on 8 different samples. The following samples are used:

- Encrusted color pigment smalt on sandstone
- Polluted 18th century parchment
- Polluted marble gravestone
- Artificial encrusted model glass
- Rusty modern steel
- Varnish on black paint
- Black paint on white paint
- Black painted modern glass

A summary of the used parameters and results is shown in Table 8.1 and 8.2. The results and data of encrusted color pigment smalt on sandstone will be discussed in detail in this section. The data and results of the other samples will be discussed less detailed.

Encrusted smalt

The artificial encrusted pigment smalt sample was suited for automatic laser cleaning. There was a significant difference between the spectra of the encrustation layer (Fig. 8.10 and Fig. 8.11) and the spectrum when reaching the layer to be preserved (Fig. 8.12). Fig. 8.5 shows the sample before laser cleaning and Fig. 8.6 shows the same extract after partial laser cleaning. The rectangular area (4.5 x 6.0 mm^2) was cleaned with a 1.5 x 1.5 mm^2 square laser spot in one minute time. Considerably recognizable is the removal of encrustation outside the cleaning boundary. Since the black gypsum layer was brittle, shockwaves induced during laser cleaning affected removal of gypsum outside the irradiation spot. This caused in addition to the inhomogeneity of the unwanted layer an adaptation of the number of pulses per spot. The applied number of pulses per spot and an enlargement of the cleaned area are shown in Fig. 8.7 and Fig. 8.8.

Table 8.1 Summary of the sample assembly, applied parameters and result per sample, part 1

	Encrusted smalt	Polluted parchment	Polluted marble	Encrusted glass
Unwanted layer	Artificial: black gypsum	Natural pollution	Natural pollution	Artificial encrustation
Layer to be preserved	Smalt, binding linseed oil	Parchment	White marble	Model glass
Base material	Sandstone	-	-	-
Spot size [mm^2]	1.5 x 1.5	1.5 x 1.4	1.44 x 1.45	0.80 x 0.75
Cleaned area [mm^2]	4.5 x 6.0	4.5 x 5.6	-	3.20 x 3.75
Correlation range [nm]	200 - 1100	200 - 1100	282 - 1100	282 - 550
Compare criterion	0.98	0.99	-	0.986
Pulse energy [mJ]	42	15	21	37
Delay [µs]	0	0	0	3.5
Result per spot	+ +	+ +	– –	+
No visibility of the single spots	+ +	+		+
Comment	Overall good result	Overall good result	Spectra of the different layers to identical	The spot array was slightly visible

Table 8.2 Summary of the sample assembly, applied parameters and result per sample, part 2

	Rusty modern steel	Varnish on black paint	Black on white paint	Black paint on modern glass
Unwanted layer	Oxidation layer	Varnish	Black paint	Black glass paint
Layer to be preserved	Steel	Black paint	White paint	Modern glass
Base material	-	Wood	Wood	-
Spot size [mm^2]	1.46 x 1.47	1.42 x 1.43	1.42 x 1.43	1.47 x 1.48
Cleaned area [mm^2]	5.84 x 5.88	4.26 x 4.29	4.26 x 4.29	5.88 x 5.92
Correlation range [nm]	282 - 1100	282 - 1100	282 - 1100	282 - 1100
Compare criterion	0.99	0.93	0.95 & 0.98	0.99
Pulse energy [mJ]	26	25	25	23
Delay [µs]	0	0	0	0
Result per spot	+/–	+ +	+ +	– –
No visibility of the single spots	– –	+	+	– –
Comment	The spot array was clearly visible	Overall good result	Overall good result	Spot array visible, the glass was affected

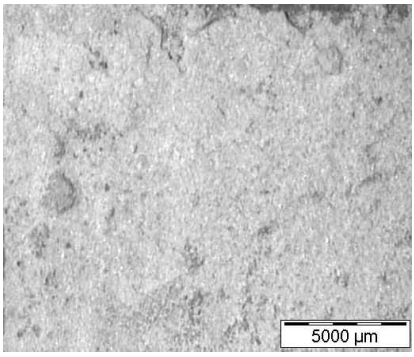

Fig. 8.5 Encrusted smalt before laser cleaning

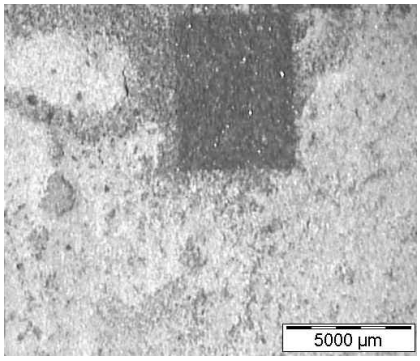

Fig. 8.6 Encrusted smalt with automatic laser cleaned area

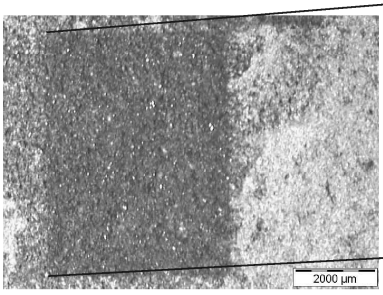

Fig. 8.7 Enlargement of the laser cleaned area

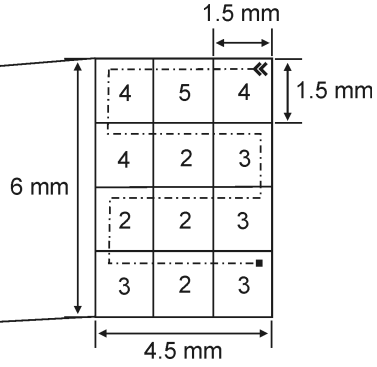

Fig. 8.8 Meander movement during cleaning of encrusted smalt. The numbers represent the amount of ablation pulses per spot

The corresponding correlation coefficients calculated during automatic cleaning of the encrusted smalt sample versus ablation pulse number per spot are visualized in Fig. 8.9. The horizontal dashed line indicates the compare criterion (0.98). After exceeding this value the ablation process was paused and continued at the next spot. More pulses were needed on spot 1 to 4 in comparison to spot 5 to 12 since the latter were affected by the induced shockwave of pulse 1 to 4.

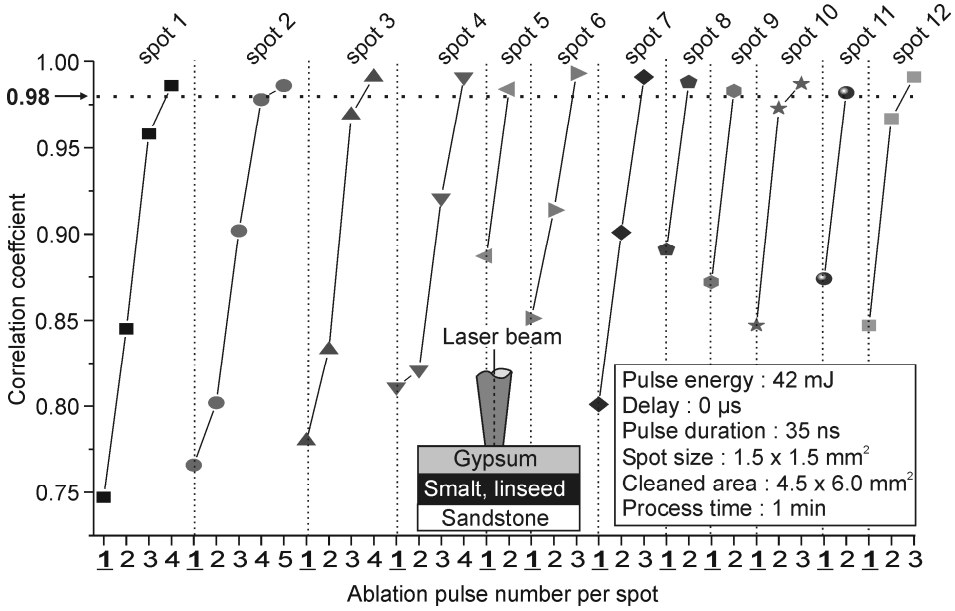

Fig. 8.9 Variation of the correlation coefficient versus ablation pulse number per spot calculated during automatic laser cleaning of encrusted smalt. When the correlation coefficient exceeded the compare criterion (0.98) the process is paused and continued at the next spot position

The trend of the LIB-spectra of spot 6 is shown by Fig. 8.10 (pulse 1), Fig. 8.11 (pulse 2) and Fig. 8.12 (pulse 3). All the spectra were correlated with the reference spectrum shown in Fig. 8.13. This reference spectrum was recorded at the transition smalt / encrustation.

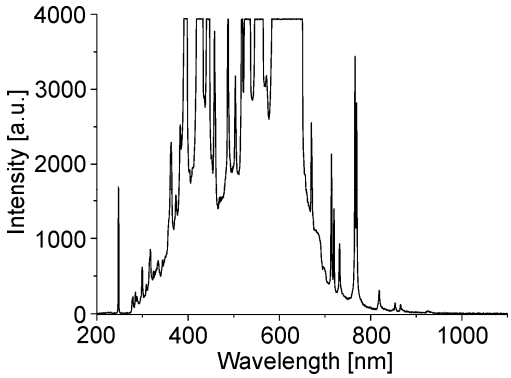

Fig. 8.10 LIB-spectrum of pulse 1 spot 6, r = 0.851

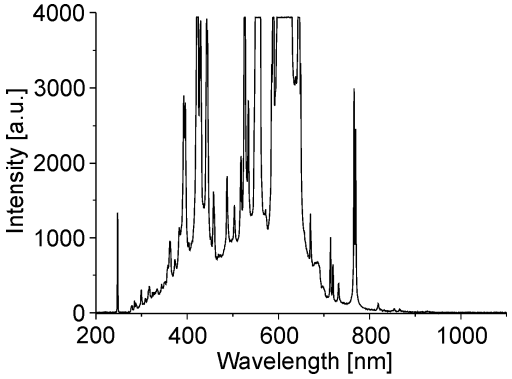

Fig. 8.11 LIB-spectrum of pulse 2 spot 6, r = 0.914

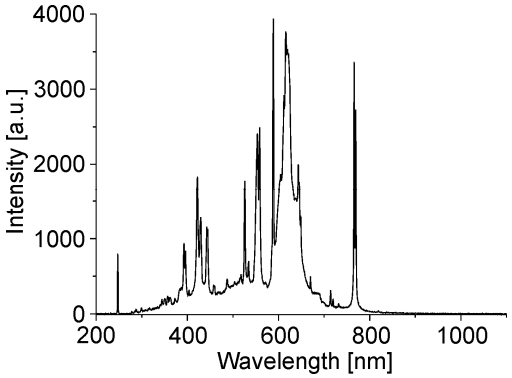

Fig. 8.12 LIB-spectrum of pulse 3 spot 6, r = 0.993

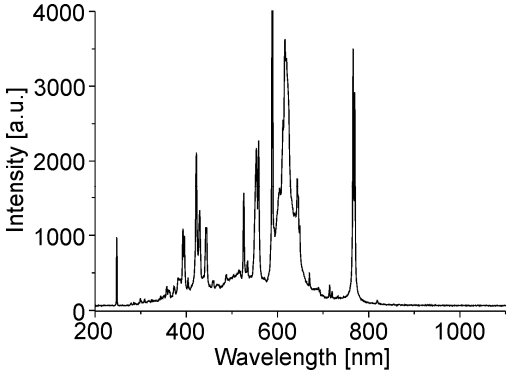

Fig. 8.13 Applied reference spectrum

The outcome of the automatically cleaned encrusted smalt sample was a smooth cleaned area without visible footprints of the single laser pulses.

Polluted 18th century parchment

The parchment sample was suited for automatic laser cleaning. There was a significant difference between the spectra of the pollution layer (Fig. 8.18) and the spectrum when reaching the parchment layer (Fig. 8.19). Fig. 8.14 shows the sample before laser cleaning and Fig. 8.15 shows the same extract after partial laser cleaning. The applied number of laser pulses per spot and the meander movement of the sample are shown in Fig. 8.16. Fig. 8.17 shows the corresponding correlation coefficients calculated during automatic cleaning of the polluted parchment sample versus ablation pulse number per spot. The horizontal dashed line indicates the compare criterion (0.99). The result was a smooth cleaned area without visible footprints of the single laser pulses.

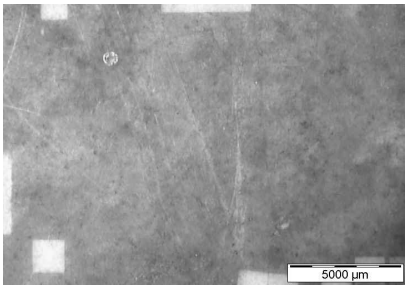

Fig. 8.14 Polluted parchment before laser cleaning

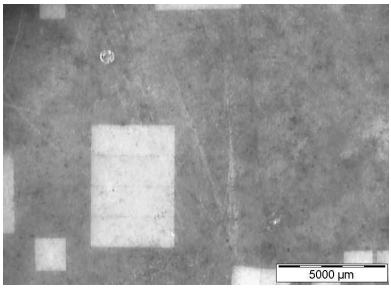

Fig. 8.15 Polluted parchment with automatic laser cleaned area

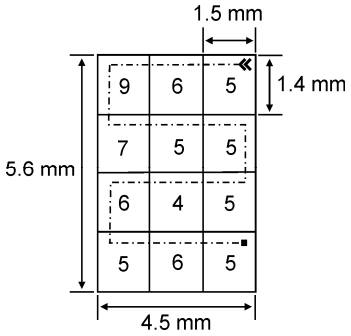

Fig. 8.16 Meander movement during cleaning of polluted parchment. The numbers represent the amount of ablation pulses per spot

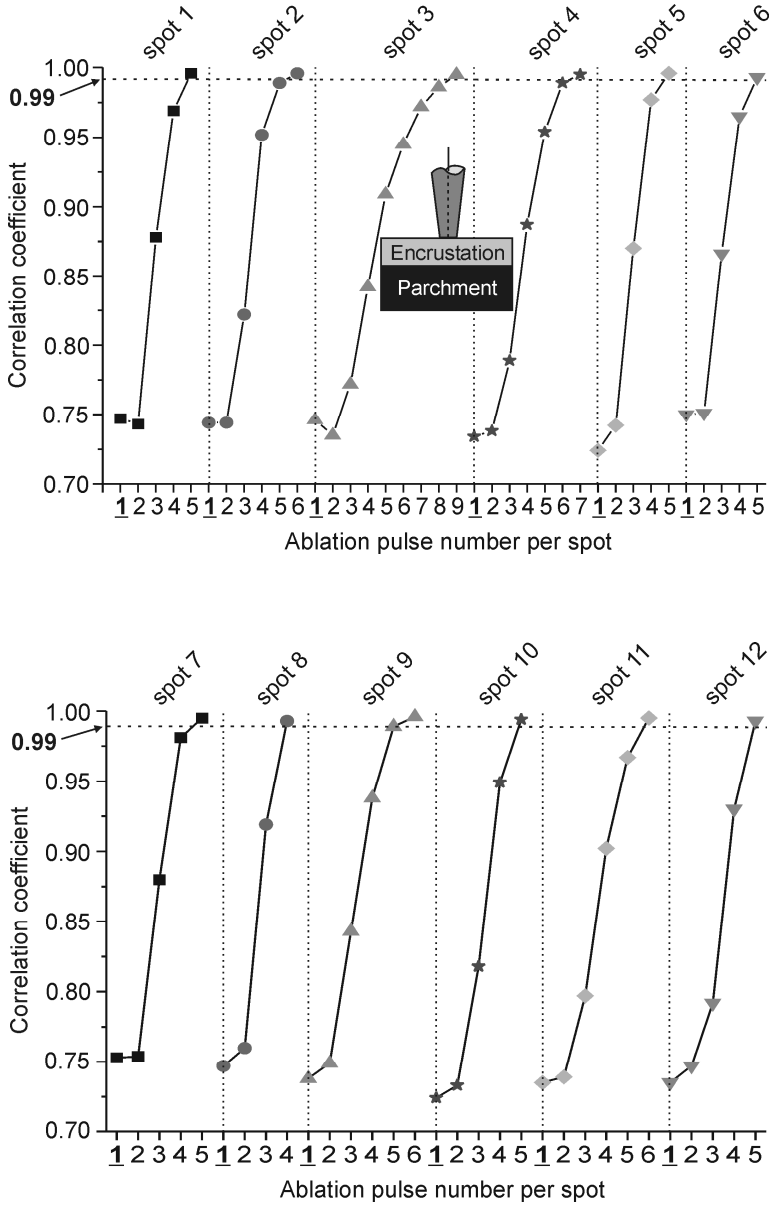

Fig. 8.17 Variation of the correlation coefficient versus ablation pulse number per spot calculated during automatic laser cleaning of polluted 18th century parchment. When the correlation coefficient exceeded the compare criterion (0.99) the process is paused and continued at the next spot position

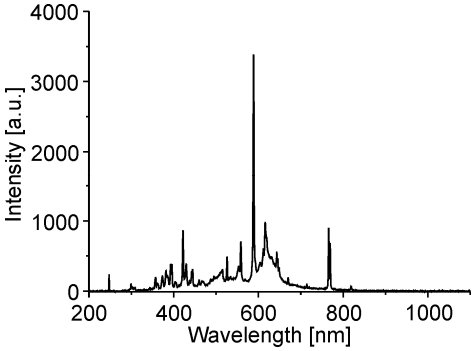

Fig. 8.18 LIB-spectrum of pulse 1 spot 5, r = 0.724 (parchment sample)

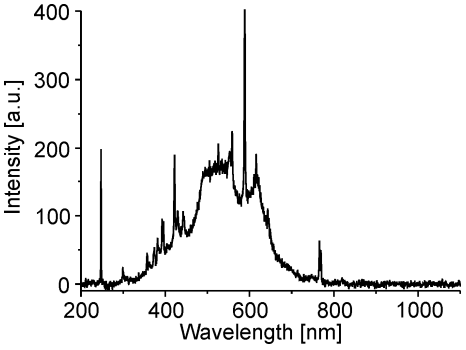

Fig. 8.19 LIB-spectrum of pulse 5 spot 5, r = 0.996 (parchment sample)

Polluted marble gravestone

The marble gravestone was unsuitable for automatic laser cleaning (with this set-up) since the acquired spectra of the different layers were too identical. Fig. 8.20 shows a LIB-spectrum of the encrustation and Fig. 8.21 of the marble layer. Using a spectrometer with higher resolution can increase the ability to discriminate.

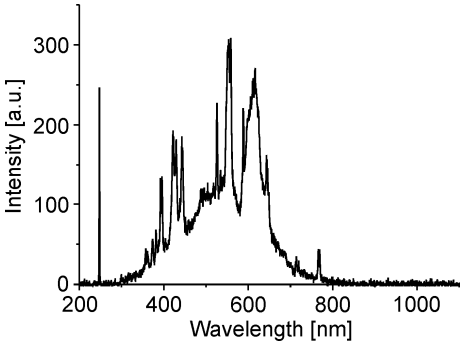

Fig. 8.20 LIB-spectrum of the encrustation layer

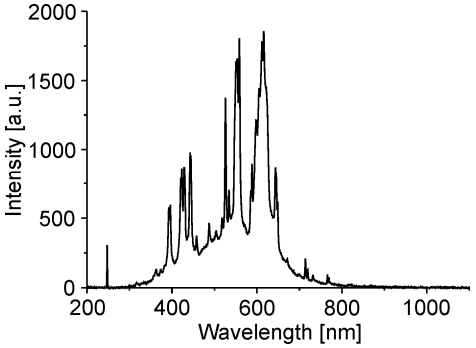

Fig. 8.21 LIB-spectrum of the marble layer

Artificial encrusted model glass

The artificial encrusted model glass sample was satisfactorily cleaned. The spectra of the different layers were very identical (Fig. 8.26 and Fig. 8.27). By decreasing the correlation interval to 282 – 550 nm it was anyhow feasible to distinguish between the different layers. However, the result is less convincing

than the result of the smalt sample. The surface is not smoothly cleaned and the spot array is slightly visible. Fig. 8.22 shows the sample before laser cleaning and Fig. 8.23 shows the same extract after partial laser cleaning. The applied number of laser pulses per spot and the meander movement of the sample are shown in Fig. 8.24. Fig. 8.25 shows the corresponding correlation coefficients calculated during automatic cleaning of the artificial encrusted model glass sample versus ablation pulse number per spot. The horizontal dashed line indicates the compare criterion (0.986).

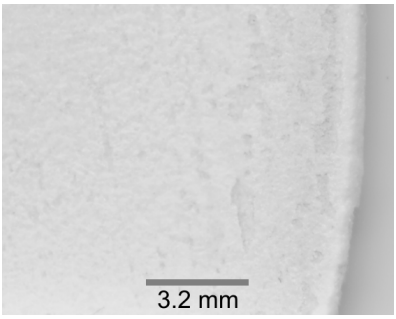

Fig. 8.22 Encrusted model glass before laser cleaning

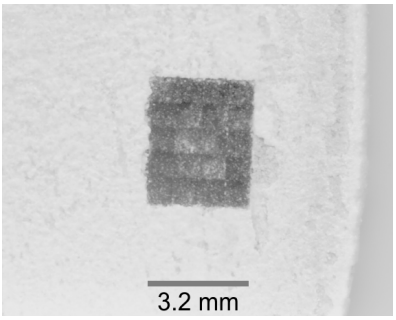

Fig. 8.23 Encrusted model glass with automatic laser cleaned area

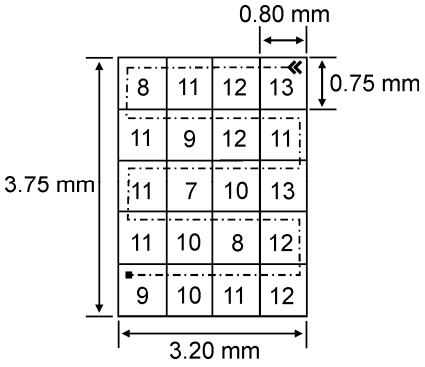

Fig. 8.24 Meander movement during cleaning of encrusted model glass. The numbers represent the amount of ablation pulses per spot

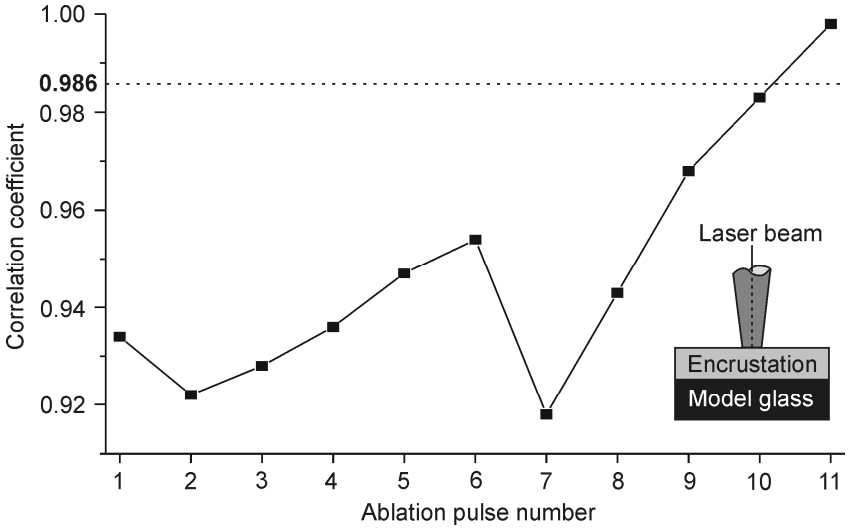

Fig. 8.25 Variation of the correlation coefficient versus ablation pulse number (spot 3) calculated during automatic laser cleaning of the encrusted model glass sample (compare criterion 0.986)

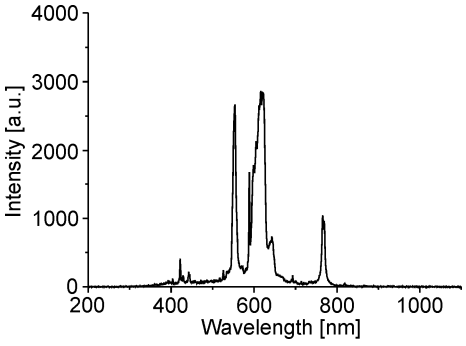

Fig. 8.26 LIB-spectrum of the encrustation layer (pulse 1, spot 3)

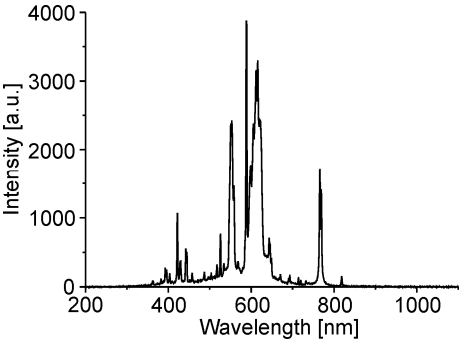

Fig. 8.27 LIB-spectrum when reaching the glass layer (pulse 11, spot 3)

Rusty modern steel

The rusty modern steel sample (Fig. 8.28) was unsuitable for automatic laser cleaning. At some spots the process stopped automatically when reaching the steel surface. However, when the oxidation constitution on the current spot differed from the oxidation on the reference spectrum position the process continued. In this case the process was stopped by manual intervention.

Furthermore, the sample suffered from carbonization during laser cleaning. This resulted in clearly visible single spots (Fig. 8.29).

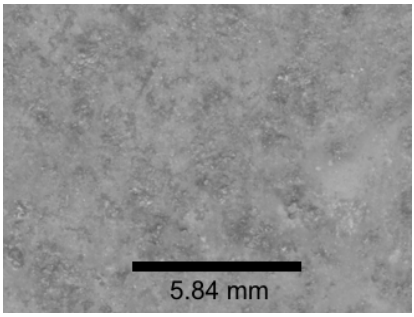

Fig. 8.28 Rusty modern steel before laser cleaning

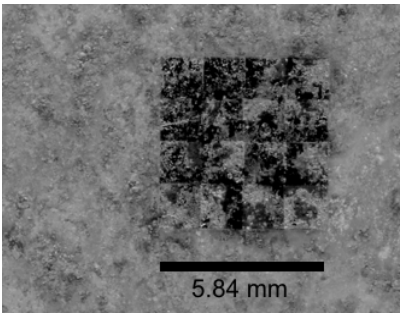

Fig. 8.29 Rusty modern steel with automatic laser cleaned area

Varnish on black paint

The varnish on black paint sample was suited for automatic laser cleaning. There was a significant difference between the spectra of the varnish layer and the black paint layer (Fig. 8.34 and Fig. 8.35). The result was a smooth cleaned area without visible footprints of the single laser pulses. Fig. 8.30 shows the sample before laser cleaning and Fig. 8.31 shows the same extract after partial laser cleaning. The applied number of laser pulses per spot and the meander movement of the sample are shown in Fig. 8.32. Fig. 8.33 shows the corresponding correlation coefficients calculated during automatic cleaning of the varnish on black paint sample versus ablation pulse number per spot. The horizontal dashed line indicates the compare criterion (0.93).

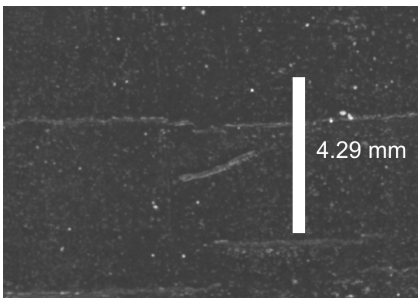

Fig. 8.30 Varnish on black paint sample before laser cleaning

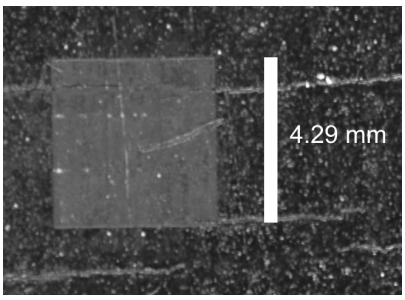

Fig. 8.31 Varnish on black paint sample with automatic laser cleaned area

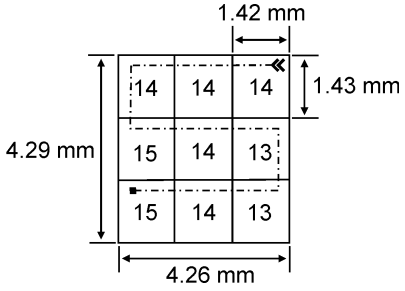

Fig. 8.32 Meander movement during cleaning of the varnish on black paint sample. The numbers represent the amount of ablation pulses per spot

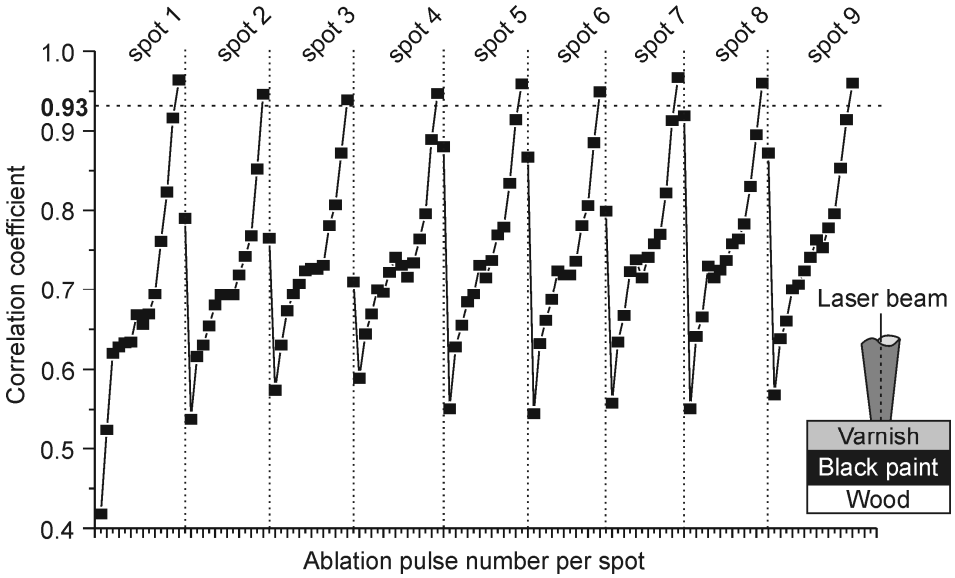

Fig. 8.33 Variation of the correlation coefficient versus ablation pulse number per spot calculated during automatic laser cleaning of the varnish on black paint sample (compare criterion 0.93)

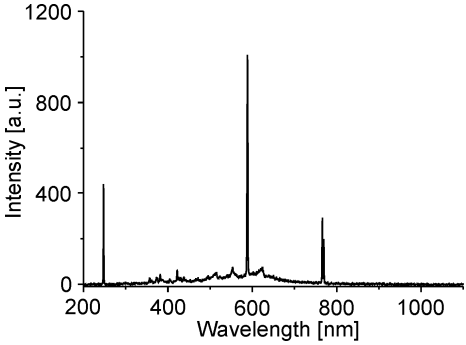

Fig. 8.34 LIB-spectrum of the varnish layer (pulse 2, spot 1)

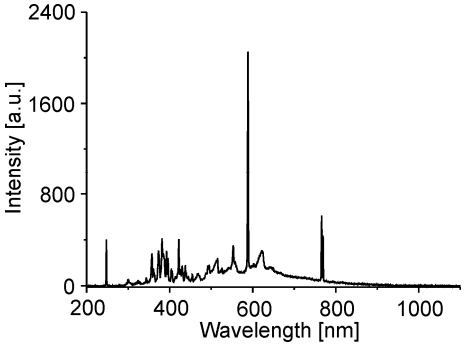

Fig. 8.35 LIB-spectrum when reaching the black paint layer (pulse 14, spot 1)

Black paint on white paint

The black paint on white paint sample was suited for automatic laser cleaning. There was a significant difference between the spectra of the black paint layer and the spectra when reaching the white paint layer (Fig. 8.41 and Fig. 8.42). The result was a cleaned area without visible footprints of the single laser pulses. The degree of purification could be regulated by adjusting the comparing criterion (0.95 or 0.98). Fig. 8.36 shows the sample before laser cleaning and Fig. 8.37 shows the same extract after partial laser cleaning with a comparing criterion of 0.95. The result of automatic cleaning with a comparing criterion of 0.98 is shown in Fig. 8.39. The higher degree of purification is clearly visible. Fig. 8.40 shows the typical variation of the correlation coefficient during cleaning of the black paint on white paint sample (one spot). The horizontal dashed line indicates the compare criterion 0.98.

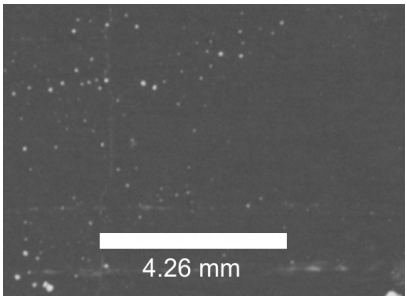

Fig. 8.36 Black paint on white paint sample before laser cleaning

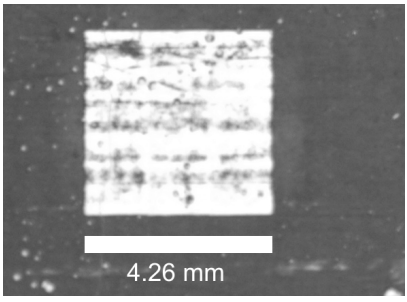

Fig. 8.37 Black paint on white paint sample with automatic laser cleaned area (compare criterion 0.95)

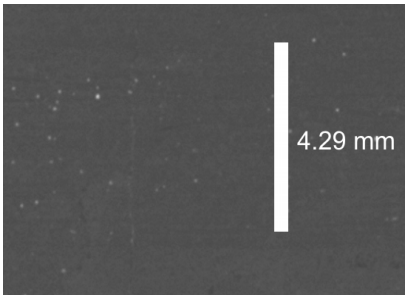

Fig. 8.38 Black paint on white paint sample before laser cleaning

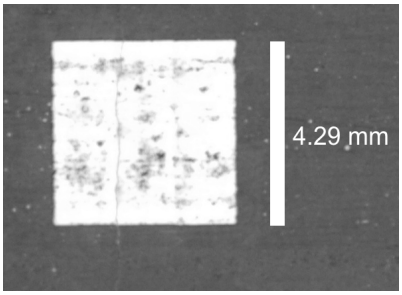

Fig. 8.39 Black paint on white paint sample with automatic laser cleaned area (compare criterion 0.98)

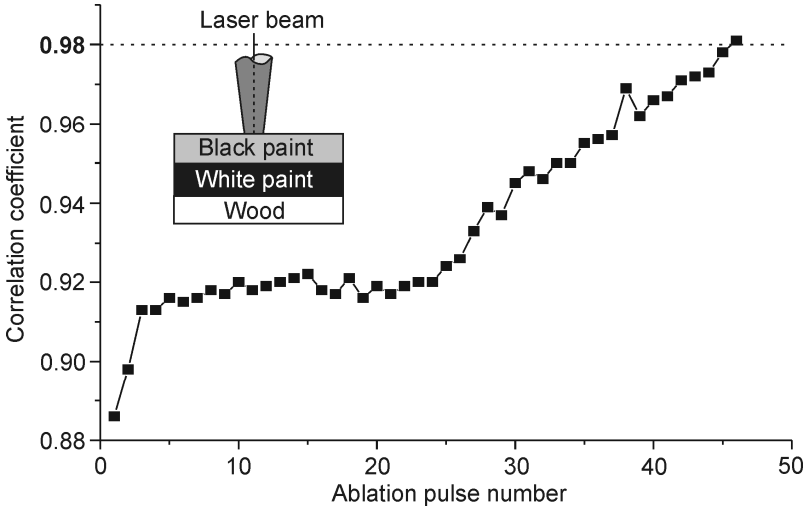

Fig. 8.40 Variation of the correlation coefficient versus ablation pulse number (spot 1) calculated during automatic laser cleaning of the black paint on white paint sample (compare criterion 0.98)

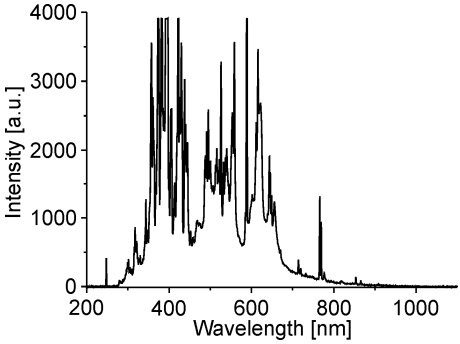

Fig. 8.41 LIB-spectrum of the black paint layer (pulse 5, spot 1, compare criterion 0.98)

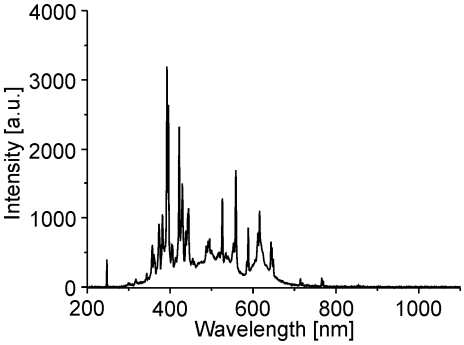

Fig. 8.42 LIB-spectrum when reaching the white paint layer (pulse 45, spot 1, compare criterion 0.98)

Black painted modern glass

The black painted modern glass sample (Fig. 8.43) was unsuitable for automatic laser cleaning since the glass substrate was affected. The paint layer was not ablated homogeneously whereby parts of the glass were early in time exposed to laser radiation. Due to the single irradiation, spots were clearly visible (Fig. 8.44).

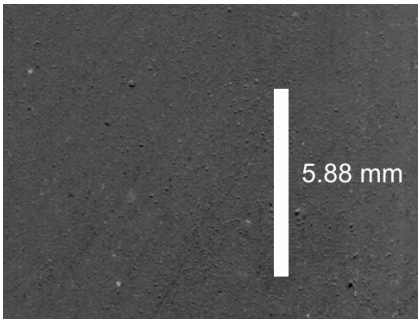

Fig. 8.43 Black paint on modern glass sample before laser cleaning

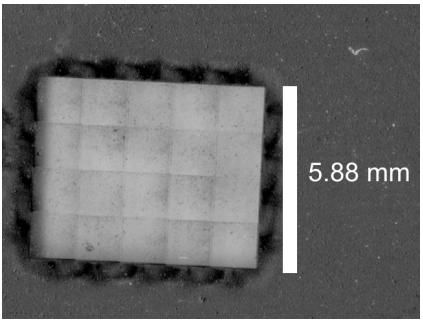

Fig. 8.44 Black paint on modern glass sample with automatic laser cleaned area

8.1.4 Conclusions and side effects

The experiments on the (artificial) artwork samples have already shown that a laser cleaning process can be controlled by low resolution plasma analysis based on correlation analysis. In case the plasma emission of the different

layers was too identical, controlling the laser cleaning process by correlation analysis was not possible (e.g. marble gravestone sample). In some cases the degree of purification could be regulated by adjusting the comparing criterion (e.g. black paint on white paint). In the event of cleaning without plasma emission the in this thesis described method can not be applied.

Side by side positioning of the ablation spots caused in some cases the visibility of the spot array which can be a serious drawback (e.g. artificial encrusted model glass and rusty modern steel). This problem can sometimes be reduced by post treatment e.g. wiping with an in solvent soaked wiping cloth over the treated area (the samples in this chapter were not post treated). The visibility of footprints of the single laser pulses is less on samples with a macroscopic-granular pollution structure (e.g. encrusted smalt).

As result of the spectrometer integration time, data transfer time, correlation coefficient calculation time and the LabView processing time the maximum working frequency of the applied set-up was practical limited to 10 Hz. This can be extended by using proper components e.g. faster computer, other software and electronics.

8.2 Nd:Yag system with articulated arm

The optical set-up of the Nd:YAG cleaning laser is equipped with a manual articulated mirror arm. The advantage of the spatial manual maneuverability can be as well a disadvantage, since the exact irradiation position is unknown and the beam cannot be manipulated automatically. Therefore, cleaning systems with manual articulated beam delivery are generally not adapted for closed-loop cleaning. However, during laser cleaning the coordinates of each laser pulse on the artwork can be obtained by a camera above the sample in combination with image processing (Fig. 8.45 and Fig. 8.46).

In first attempts this method was applied to obtain the corresponding coordinates of LIB-spectra measurements whilst laser cleaning. The position of the interaction area of each pulse was achieved shortly after the laser pulse and plasma emission by analyzing the position of a coaxial HeNe laser spot on the sample. The HeNe laser spot was used since the Nd:YAG laser pulse and the plasma emission saturated the CCD of the webcam.

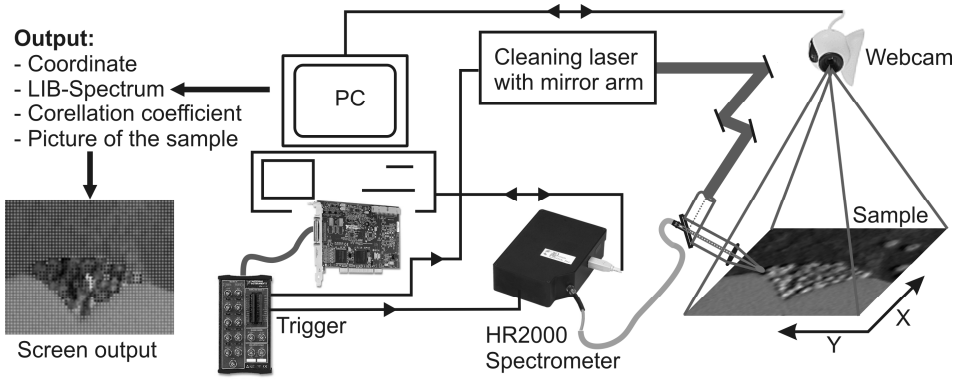

Fig. 8.45 Schematic of the webcam-LIBS set-up applied to measure LIB-spectra and the accompanied interaction area coordinates. The right picture shows the sample with ablation spots while the left picture shows the same picture with transparent overlay. The sample in the figure is iron covered with a thin rust layer

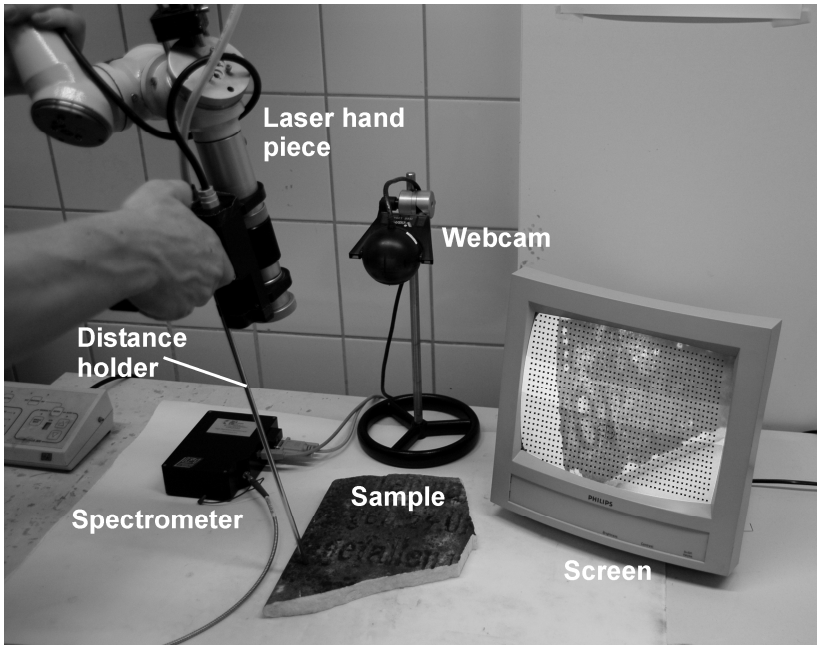

Fig. 8.46 Photograph of the webcam-LIBS set-up

Since the positions of the laser pulses are known the results of the corresponding LIBS-measurements can be displayed as a transparent overlay

with discreet color variations on top of the picture of the artwork. The color value corresponds to the result obtained at that coordinate. In this way any kind of single value result can be displayed in a picture e.g. element line intensity, intensity ratio, linear correlation coefficient, etc.

In this thesis the linear correlation results, calculated by correlating the current measured spectrum with a pre-stored reference spectrum, were displayed by a corresponding color in a picture of the sample. On-line visualization of the artwork with a current measurement-overlay on a (computer) screen during laser cleaning can be used to monitor/control the process. By means of the color values the restorer can recognize the parts of the artworks that are sufficiently cleaned to avoid over-cleaning.

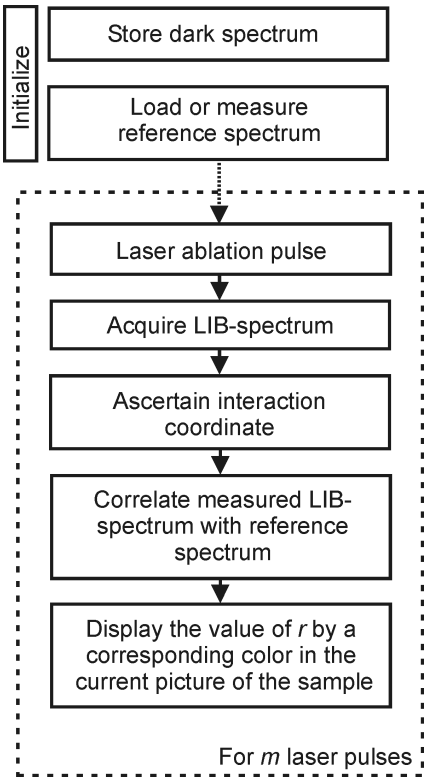

Fig. 8.47 Flow diagram of the webcam and LIBS based laser cleaning monitoring

8.2.1 Experimental set-up

The experimental set-up is shown in Fig. 8.45 and Fig. 8.46. The applied laser and spectrometer are described in section 3.1.2 and in section 3.2.1. Since the output beam was not parallel but converging a distance holder was applied to secure a constant energy density on the object surface (Fig. 8.46). The used camera is a FireWire 1394 Webcam with 640 x 480 VGA resolution. The timing between attaining the coordinate, firing the laser and acquiring a LIB-spectrum was arranged in the LabView program in combination with the DAQ-card. The standard LabView 7.1 software was extended with the LabView Vision Development Module which enables image processing. The sequence of the software for monitored laser cleaning with manual articulated beam delivery is shown in Fig. 8.47.

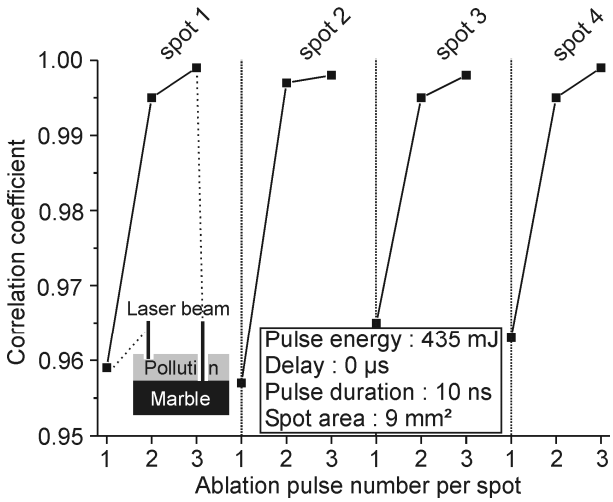

Fig. 8.48 Variation of the correlation coefficient versus ablation pulse number per spot calculated during first trials with the webcam Nd:YAG cleaning laser monitoring set-up (constant experimental parameters)

8.2.2 Results and side effects

First trials of this method applied to 3 different samples (black on white paint, polluted marble gravestone and rusty steel) showed the basic workability. It was possible to acquire LIB-spectra and the position of the measurements after the webcam and image processing settings were optimized per sample. The image

processing settings which could be changed were e.g. detection threshold, sharpness, saturation, brightness and post processing image filter. The results were repeatable at different sample positions on condition that the experimental (LIBS) parameters retain constant. This was achieved by applying a distance holder and constant irradiation angle. Fig. 8.48 shows the trend of the correlation coefficients obtained with the polluted marble sample at constant experimental parameters (the results of the remaining two samples are not displayed as they featured the same trend).

In praxis, experimental parameters like lens object distance, spot size and irradiation angle can vary from pulse to pulse when the beam is manipulated manually. This influences the form and intensity of the acquired spectra and therewith the distribution of correlation coefficients of the different layers (see chapter 5 and chapter 7). If the correlation coefficients distributions of the different layers barely overlap when using a distance holder and a constant irradiation angle, this method cannot be applied to identify layers when cleaning with complete manual articulated beam delivery. The standard deviation will increase which results in a spread of the single distributions. This means that the acquired spectra, corresponding to the different layers have to provide a higher difference in comparison to cleaning with constant experimental parameters (e.g. KrF-excimer set-up). This was the limiting effect during the experiments with the low resolution spectrometer and articulated beam delivery. The differences between the correlation coefficients corresponding to the second and third pulse at spot 1 to 4 in Fig. 8.48 were < 0.005 at constant experimental condition. This was too low for in-process identifying during cleaning without distance holder.

The results of section 7.3.3 show that an object hand piece distance variation will not significantly change the form of the acquired spectra. If the output beam is parallel, a perpendicular object hand piece distance change will not change the energy density. With these pre-conditions in-process identifying during cleaning without distance holder with the applied set-up should be possible.

9 Conclusions and discussion

In this thesis the applicability of low resolution plasma spectroscopy to automatically control laser cleaning processes of artworks has been investigated. Experiments on (artificial) artworks have shown that a laser cleaning process can be controlled or monitored by linear correlation analysis and a low cost fibre optic spectrometer. An advantage of the applied linear correlation method is the operability by non spectroscopic educated restorers.

The experimental investigations showed that an ablation process can be stopped at a pre-defined level by in-process identification of layers / materials by the weight of correlation on condition that: there is a recordable plasma emission during the complete process, the spectra of the different layers or materials vary in form and intensity and the distributions of correlation coefficients corresponding to layers to be distinguished between show no overlap. The reference spectra were generally recorded at the transition pollution layer and layer to be preserved. In case of a selective sample assortment the spectral bandwidth of the spectrometer can be optimized, this can lead to an increase of the differentiation capability.

Experiments showed that the signal to noise ratio (S/N) has a significant influence on the reproducibility of measured spectra with a low intensity. With increasing S/N the reproducibility increases. The spectrometer process parameter settings for most reproducible spectra are: no delay between the laser pulse and recording the plasma emission, long integration time and low

spectrometer resolution. However, these parameter settings can lead to a decrease of the distinguishability between the spectra of different materials.

The process has been automated (laser wit translation stage) by connecting all single modules to a controller PC running an in LabView written software. This closed loop system was able to clean predefined areas automatically. The (artificial) artwork samples that were used for the experiments are: encrusted color pigment smalt on sandstone, polluted 18th century parchment, polluted marble gravestone, artificial encrusted model glass, rusty modern steel, varnish on black paint, black paint on white paint and black painted modern glass. The best visual results were obtained on samples with a macroscopic-granular pollution structure. In the event of almost identical acquired spectra of the different layers an automatic cleaning of the samples was not possible (encrusted marble gravestone). In some cases the degree of purification could be regulated by adjusting the comparing criterion (black paint on white paint).

In a first trial the LIBS-correlation method has been used to monitor laser cleaning with a manual articulated mirror arm. Therefore, a webcam was placed above the sample to ascertain the irradiation position. The obtained correlation coefficients were visualized in a current picture of the sample by color marks representing the progress of the cleaning. The obtained results for the tested samples (black on white paint, polluted marble gravestone and rusty steel) were repeatable, provided that the experimental parameters retain constant. This was achieved by applying a distance holder and constant irradiation angle. It was feasible to acquire LIB-spectra and the position of the measurements after the webcam and image processing settings were optimized per sample.

Recommendation

The bandwidth of the applied spectrometer was chosen 200 – 1100 nm since it had to be applicable for a great sample assortment. However, the best response of the CCD used in this miniature spectrometer as well as the highest efficiency of the applied optical fibre, proved to be in the range 300 – 800 nm. This can clearly been seen at the acquired LIB-spectra, there is almost no (acquired) spectral information in the intervals 200 – 300 nm and 800 – 1100 nm. Decreasing the bandwidth to 300 – 800 nm increases the efficiency and the resolution of the system and therewith the differentiation capability, without losing applicability.

References

[1] J.F. Asmus, C.G. Murphy and W.H. Munk, *Studies on the interacion of laser radiation with art artifacts.* Proceedings of SPIE, 1973. **41**: p. 19-27.

[2] K. Dickmann, C. Fotakis and J.F. Asmus, eds. *Lasers in the Conservation of Artworks, Proc. of the International Conference LACONA V*. Springer Proceedings in Physics. Vol. 100. 2005.

[3] W. Kautek and E. König, eds. *Proc. of the First International Conference LACONA I - Lasers in the Conservation of Artworks*. Restauratorenblätter, Sonderband - Lacona I. 1997, Mayer & Comp.

[4] R. Salimbeni and G. Bonsanti, eds. *Proc. of the International Conference LACONA III - Lasers in the Conservation of Artworks*. Journal of Cultural Heritage. Vol. 1, Suppl. 1. 2000.

[5] V. Vergès-Belmin, ed. *Proc. of the International Conference LACONA IV - Lasers in the Conservation of Artworks*. Journal of Cultural Heritage. Vol. 4, Suppl. 1. 2003.

[6] R. Teule, H. Scholten, O.F.v. Brink, R.M.A. Heeren, V. Zafiropulus, R. Hesterman, M. Castillejo, M. Martin, U. Ullenius, I. Larsson, F. Guerra-Librero, A. Silva, H. Gouveia and M.B. Albuquerque, *Controlled UV laser cleaning of painted artworks: a systematic effect study on egg tempera paint samples.* Journal of Cultural Heritage, 2003. **4**: p. 209-215.

[7] J.H. Scholten, J.M. Teule, V. Zafiropulos and R.M.A. Heeren, *Controlled laser cleaning of painted artworks using accurate beam manipulation and on-line LIBS-detection.* Journal of Cultural Heritage, 2000. **1**: p. 215-220.

[8] M. Cooper, *Laser Cleaning in conservation, an introduction*. 1998: Butterworth-Heinemann.

[9] C. Baracchini, R. Pini, F. Fabiani, M. Ciafaloni, S. Siano, R. Salimbeni, G. Sabatini, M. Giamello, M. Franzini, M. Lezzerini, M. Spampinato, F. Gravina and F. Andreazzoli, *The Pilot Restoration Yard of the Church of San Frediano in Pisa: Results of a Multidisciplinary Study*. Laser in the Conservation of Artworks, Springer Proceedings in Physics, ed. K. Dickmann, C. Fotakis and J.F. Asmus. Vol. 100. 2005: Springer. 191-197.

[10] C. Weeks, *The Conservation of the Portail de la Mère Dieu, Amiens Cathedral, France*. Proc. of the First International Conference LACONA I - Lasers in the Conservation of Artworks, Restauratorenblätter, Sonderband - Lacona I, ed. W. Kautek and E. König. 1997: Mayer & Comp. 25-29.

[11] G. Calcagno, M. Koller and H. Nimmrichter, *Laserbased Cleaning on Stonework at St. Stephan's Cathedral, Vienna*. Proc. of the First International Conference LACONA I - Lasers in the Conservation of Artworks, Restauratorenblätter, Sonderband - Lacona I, ed. W. Kautek and E. König. 1997: Mayer & Comp. 39-43.

[12] H. Siedel and G. Wiedemann, eds. *Laserstrahlreinigen von Naturstein*. 2002, Fraunhofer IRB Verlag.

[13] V. Zafiropulos and C. Fotakis, eds. *Lasers in the conservation of painted artworks*. Laser Cleaning in conservation, an introduction, ed. M. Cooper. 1998, Butterworth-Heinemann. 79-90.

[14] V. Zafiropulos, *Laser ablation in cleaning of artworks*, in *Laser Cleaning*, B. Luk`yanchuk, Editor. 2002, Butterworth-Heinemann. p. 343-392.

[15] J. Hildenhagen, M. Chappé and K. Dickmann, *Reaction of Historical Colours and their Components Irradiated at Different Nd:YAG Laser Wavelengths (ω, 2ω, 3ω, 4ω)*. Laser in the Conservation of Artworks, Springer Proceedings in Physics, ed. K. Dickmann, C. Fotakis and J.F. Asmus. Vol. 100. 2005: Springer. 297-301.

[16] H. Scholten, P. van Dalen, S. Corr, P. Rudolph, J.B.G.A. Havermans, H.A. Aziz and F.J. Ligterink, *Laser Cleaning of Pressure Sensitive Tapes on Paper*. Laser in the Conservation of Artworks, Springer Proceedings in Physics, ed. K. Dickmann, C. Fotakis and J.F. Asmus. Vol. 100. 2005: Springer. 43-49.

[17] H. Scholten, D. Schipper, F.J. Ligterink, J.L. Pedersoli Jr., P. Rudolph, W. Kautek, J.B.G.A. Havermans, H.A. Aziz, B. van Beek, M. Kraan, P. van Dalen, V. Quillet, S. Corr and H.Y. Hua-Ströfer, *Laser Cleaning Investigations of Paper Models and Original Objects with Nd:YAG and KrF Laser Systems*. Laser in the Conservation of Artworks, Springer Proceedings in Physics, ed. K. Dickmann, C. Fotakis and J.F. Asmus. Vol. 100. 2005: Springer. 11-18.

[18] W. Kautek and S. Pentzien, *Laser Cleaning System for Automated Paper and Parchment Cleaning*. Laser in the Conservation of Artworks, Springer Proceedings in Physics, ed. K. Dickmann, C. Fotakis and J.F. Asmus. Vol. 100. 2005: Springer. 403-410.

[19] K. Dickmann, J. Hildenhagen, J. Studer and E. Müsch, *Archaeological Ironwork: Removal of Corrosion Layers by Nd:YAG-Laser*. Laser in the Conservation of Artworks, Springer Proceedings in Physics, ed. K. Dickmann, C. Fotakis and J.F. Asmus. Vol. 100. 2005: Springer. 71-77.

[20] S. Batishche, A. Kouzmouk, H. Tatur, T. Gorovets, U. Pilipenka and V. Ukhau, *1320 nm Range Nd:YAG-Laser in Restoration of Artworks Made of Bronze and Other Metals*. Laser in the Conservation of Artworks, Springer Proceedings in Physics, ed. K. Dickmann, C. Fotakis and J.F. Asmus. Vol. 100. 2005: Springer. 87-93.

[21] T. Burmester, M. Meier, H. Haferkamp, S. Barcikowski, J. Bunte and A. Ostendorf, *Femtosecond Laser Cleaning of Metallic Cultural Heritage and Antique Artworks*. Laser in the Conservation of Artworks, Springer Proceedings in Physics, ed. K. Dickmann, C. Fotakis and J.F. Asmus. Vol. 100. 2005: Springer. 61-69.

[22] S. Siano, *Principles of laser cleaning in conservation*, in *Handbook on the Use of Lasers in Conservation and Conservation Science*, M. Schreiner and M. Strlic, Editors. 2006, http://www.science4heritage.org/COSTG7/booklet/.

[23] M. Dirscherl, *Ultrakurzpulslaser - Grundlagen und Anwendungen*. 2005: BLZ, Erlangen.

[24] K.G. Watkins, *Laser Cleaning*, in *Laser Material Processing*, W.M. Steen, Editor. 1998, Springer.

[25] K.G. Watkins, *A Review of Materials Interaction During Laser Cleaning in Art Restoration*. Proc. of the First International Conference LACONA I - Lasers in the Conservation of Artworks, Restauratorenblätter, Sonderband - Lacona I, ed. W. Kautek and E. König. 1997: Mayer & Comp. 7-15.

[26] J. Meijer, *Laser Micromachining*, in *Micromachining of Engineering Materials*, J.A. McGeough, Editor. 2001, CRC. p. 203.

[27] S. Klein, T. Stratoudaki, V. Zafiropulos, J. Hildenhagen, K. Dickmann and T. Lehmkuhl, *Laser-induced breakdown spectroscopy for on-line control of laser cleaning of sandstone and stained glass.* Applied Physics A, 1999. **69**: p. 441-444.

[28] S. Klein, J. Hildenhagen, K. Dickmann, T. Stratoudaki and V. Zafiropulos, *LIBS spectroscopy for monitoring and control of the laser cleaning process of stone and medieval glass.* Journal of Cultural Heritage, 2000. **1**: p. 287-292.

[29] I. Gobernado-Mitre, A.C. Prieto, V. Zafiropulos, Y. Spetsidou and C. Fotakis, *On-Line Monitoring of Laser Cleaning of Limestone by Laser-Induced Breakdown Spectroscopy and Laser-Induced Fluorescence.* Applied Spectroscopy, 1997. **51**(8): p. 1125-1129.

[30] D. Anglos, S. Couris, A. Mavromanolakis, I. Zergioto, M. Solomidou, W.-Q. Liu, T.G. Papazoglou, C. Fotakis, M. Doulgeridis and A. Fostiridou, *Artworks Diagnostics Laser Induced Breakdown Spectroscopy (LIBS) and Laser Induced Fluorescence (LIF) Spectroscopy*, in *Lasers in the Conservation of Artworks, Restauratorenblätter, Sonderband - LACONA I*, E. König and W. Kautek, Editors. 1995, Mayer & Comp. p. 113-118.

[31] N. Chaoui, J. Solis, C.N. Afonso, T. Fourrier, T. Muehlberge, G. Schrems, M. Mosbacher, D. Bäuerle, M. Bertsch and P. Leiderer, *A high-sensitivity in situ optical diagnostic technique for laser cleaning of transparent substrates.* Applied Physics A, 2003. **76**(5): p. 767-771.

[32] J. Hildenhagen and K. Dickmann, *Low-cost sensor system for online monitoring during laser cleaning.* Journal of Cultural Heritage, 2003. **4**: p. 343-346.

[33] M. Lentjes, D. Klomp and K. Dickmann, *Sensor Concept for Controlled Laser Cleaning via Photodiode*. Laser in the Conservation of Artworks, Springer Proceedings in Physics, ed. K. Dickmann, C. Fotakis and J.F. Asmus. Vol. 100. 2005: Springer. 427-433.

[34] J.M. Lee and K.G. Watkins, *In-process monitoring techniques for laser cleaning.* Optics and Lasers in Engineering, 2000. **34**: p. 429-442.

[35] J.M. Lee and W.M. Steen, *In-Process Surface Monitoring for Laser Cleaning Processes using a Chromatic Modulation Technique.* The International Journal of Advanced Manufacturing Technology, 2001. **17**: p. 281-287.

[36] M. Jankowska and G. Sliwinski, *Acoustic monitoring for the laser cleaning of sandstone.* Journal of Cultural Heritage, 2003. **4**: p. 65-71.

[37] E. Tognoni, V. Palleschi, M. Corsi and G. Cristoforetti, *Quantitative micro-analysis by laser-induced breakdown spectroscopy: a review of the experimental approaches.* Spectrochimica Acta Part B, 2002. **57**: p. 1115-1130.

[38] K. Song, Y.-I. Lee and J. Sneddon, *Recent developments in instrumentation for laser induced breakdown spectroscopy.* Applied Spectroscopy Reviews, 2002. **37**(1): p. 89-117.

[39] J. Sneddon and Y.-I. Lee, *Novel and recent applications of elemental determination by laser-induced breakdown spectrometry.* Analytical Letters, 1999. **32**(11): p. 2143-2162.

[40] D.A. Rusak, B.C. Castle, B.W. Smith and J.D. Winefordner, *Fundementals and Applications of Laser-Induced Breakdown Spectroscopy.* Critical Reviews in Analytical Chemistry, 1997. **27**(4): p. 257-290.

[41] L.J. Radziemski, *From LASER to LIBS, the path of technology development.* Spectrochimica Acta Part B, 2002. **57**(7): p. 1109-1113.

[42] W.-B. Lee, J. Wu, Y.-I. Lee and J. Sneddon, *Recent Applications of Laser-Induced Breakdown Spectrometry: A Review of Material Approaches.* Applied Spectroscopy Reviews, 2004. **39**(1): p. 27-97.

[43] D. James, J.D. Winefordner, I.B. Gornushkin, T. Correll, E. Gibb, B.W. Smith and N. Omenetto, *Comparing several atomic spectrometric methods to the super stars: special emphasis on laser induced breakdown spectrometry, LIBS, a future super star.* Journal of analytical atomic spectrometry, 2004. **19**: p. 1061-1083.

[44] D. Anglos, *Laser-Induced Breakdown Spectroscopy in Art and Archaeology.* Applied Spectroscopy, 2001. **55**(6): p. 186-205.

[45] R.S. Adrian and J. Watson, *Laser microspectral analysis: a review of principles and applications.* Journal of Physics D, 1984. **17**: p. 1915-1940.

[46] J.M. Vadillo and J.J. Laserna, *Laser-induced plasma spectrometry: truly a surface analytical tool.* Spectrochimica Acta Part B, 2004. **59**: p. 147-161.

[47] A.W. Miziolek, V. Palleschi and I. Schechter, eds. *Laser-Induced Breakdown Spectroscopy (LIBS)*. 2006, Cambridge.

[48] Y.-I. Lee, K. Song and J. Sneddon, eds. *Laser-Induced Breakdown Spectroscopy (LIBS)*. 2000, NOVA Science Publishers.

[49] D.A. Cremers and L.J. Radziemski, *Handbook of Laser-Induced Breakdown Spectroscopy*. 2006: Wiley.

[50] H. Balzer, M. Hoehne, V. Sturm and R. Noll, *Online coating thickness measurement and depth profiling of zinc coated sheet steel by laser-induced breakdown spectroscopy.* Spectrochimica Acta Part B, 2005. **60**: p. 1172-1178.

[51] S. Morel, N. Leone, P. Adam and J. Amouroux, *Detection of bacteria by time-resolved laser-induced breakdown spectroscopy.* Applied Optics, 2003. **42**(30): p. 6184-6191.

[52] J.D. Hybl, G.A. Lithgow and S.G. Buckley, *Laser-Induced Breakdown Spectroscopy Detection and Clasification of Biological Aerosols.* Applied Spectroscopy, 2003. **57**(10): p. 1207-1215.

[53] T.M. Moskal and D.W. Hahn, *On-Line Sorting of Wood Treated with Chromated Copper Arsenate Using Laser-Induced Breakdown Spectroscopy.* Applied Spectroscopy, 2002. **56**(10): p. 1337-1344.

[54] R. Noll, H. Bette, A. Brysch, M. Kraushaar, I. Monch, L. Peter and V. Sturm, *Laser-induced breakdown spectrometry -- applications for production control and quality assurance in the steel industry.* Spectrochimica Acta Part B, 2001. **56**(6): p. 637-649.

[55] A.K. Rai, F.Y. Yueh, J.P. Singh and H. Zhang, *High temperature fiber optic laser-induced breakdown spectroscopy sensor for analysis of molten alloy constituents.* Review of Scientific Instruments, 2002. **73**(10): p. 3589-3599.

[56] M. Bicchieri, M. Nardone, P.A. Russo, A. Sodo, M. Corsi, G. Cristoforetti, V. Palleschi, A. Salvetti and E. Tognoni, *Characterization of azurite and lazurite based pigments by laser induced breakdown spectroscopy and micro-Raman spectroscopy.* Spectrochimica Acta Part B, 2001. **56**: p. 915-922.

[57] D. Anglos, S. Couris and C. Fotakis, *Laser Daignostics of Painted Artworks: Laser-Induced Breakdown Spectroscopy in Pigment Identification.* Applied Spectroscopy, 1997. **51**(7): p. 1025-1030.

[58] V. Lazic, F. Colao, R. Fantoni, A. Palucci, V. Spizzichino, I. Borgia, B.G. Brunetti and A. Sgamelloti, *Characterisation of lustre and pigment composition in ancient pottery by laser induced fluorescence end breakdown spectroscopy.* Journal of Cultural Heritage, 2003. **4**: p. 303-308.

[59] L. Burgio, K. Melessanaki, M. Doulgeridis, R.J.H. Clark and D. Anglos, *Pigment identification in paintings employing laser induced breakdown spectroscopy and Raman microscopy.* Spectrochimica Acta Part B, 2001. **56**(6): p. 905-913.

[60] K. Ochocinska, M. Sawczak, M. Martin, J. Bredal-Jorgensen, A. Kaminska and G. Sliwinski, *LIPS spectroscopy for the contamination analysis and laser cleaning diagnostics of historical paper documents.* Radiation Physics and Chemistry, 2003. **68**: p. 227-232.

[61] F. Colao, R. Fantoni, V. Lazic, A. Morone, A. Santagata and A. Giardini, *LIBS used as a diagnostic tool during the laser cleaning of ancient marble from Mediterranean areas.* Applied Physics A, 2004. **79**: p. 213-219.

[62] P.V. Maravelaki, V. Zafiropulos, V. Kilikoglou, M. Kalaitzaki and C. Fotakis, *Laser-induced breakdown spectroscopy as a diagnostic technique for the laser cleaning of marble.* Spectrochimica Acta Part B, 1997. **52**: p. 41-53.

[63] M. Jankowska and G. Sliwinski, *Spectroscopic and surface analysis of the laser ablation of crust on historic sandstone elements.* Radiation Physics and Chemistry, 2003. **68**: p. 147-152.

[64] N. Carmona, M. Oujja, E. Rebollar, H. Romich and M. Castillejo, *Analysis of corroded glasses by laser induced breakdown spectroscopy.* Spectrochimica Acta Part B, 2005. **60**: p. 1155-1162.

[65] F.J. Fortes, M. Cortés, M.D. Simón, L.M. Cabalín and J.J. Laserna, *Chronocultural sorting of archaeological bronze objects using laser-induced breakdown spectrometry.* Analytica Chimica Acta, 2006. **554**: p. 136-143.

[66] V. Lazic, F. Colao, R. Fantoni and V. Spizzicchino, *Recognition of archeological materials underwater by laser induced breakdown spectroscopy.* Spectrochimica Acta Part B: Atomic Spectroscopy, 2005. **60**: p. 1014-1024.

[67] I.B. Gornushkin, B.W. Smith, H. Nasajpour and J.D. Winefordner, *Identification of Solid Materials by Correlation Analysis Using a Microscopic Laser-Induced Plasma Spectrometer.* Analytical Chemistry, 1999. **71**(22): p. 5157-5164.

[68] I.B. Gornushkin, A. Ruiz-Medina, J.M. Anzano, B.W. Smith and J.D. Winefordner, *Identification of particulate materials by correlation analysis using a microscopic laser induced breakdown spectrometer.* Journal of analytical atomic spectrometry, 2000. **15**: p. 581-586.

[69] J.M. Anzano, M.A. Villoria, I.B. Gornushkin, B.W. Smith and J.D. Winefordner, *Laser-Induced Plasma Spectroscopy for Characterization of Archaeological Material.* Canadian Journal of Analytical Sciences and Spectroscopy, 2002. **47**(5): p. 134-140.

[70] J.M. Anzano, I.B. Gornushkin, B.W. Smith and J.D. Winefordner, *Laser-Induced Plasma Spectroscopy for Plastic Identification.* Polymer engineering & science, 2000. **40**: p. 2423-2429.

[71] A. Jurado-López and M.D. Luque de Castro, *Rank correlation of laser-induced breakdown spectroscopic data for the identification of alloys used in jewelry manufacture.* Spectrochimica Acta Part B, 2003. **58**: p. 1291-1299.

[72] V. Detalle, R. Heon, M. Sabsabi and L. St-Onge, *An evaluation of a commercial Echelle spectrometer with intensified charge-coupled device detector for materials analysis by laser-induced plasma spectroscopy.* Spectrochimica Acta Part B, 2001. **56**(6): p. 1011-1025.

[73] J.E. Carranza, E. Gibb, B.W. Smith, D.W. Hahn and J.D. Winefordner, *Comparison of nonintensified and intensified CCD detectors for laser-induced breakdown spectroscopy.* Applied Optics, 2003. **42**(30): p. 6016-6021.

[74] J. Thomason, *Spectroscopy Takes Security into the Field.* Photonics spectra, 2004(April): p. 83-86.

[75] M. Sabsabi, R. Heon, V. Detalle, L. St-Onge and A. Hamel, *Comparison between intensified CCD and non-intensified gated CCD detectors for LIPS analysis of solid samples, Laser Induced Plasma Spectroscopy and Applications*. OSA Trends in Optics and Photonics Series. Vol. 81. 2002: OSA, Washington D.C. 128-130.

[76] M. Sabsabi, R. Heon and L. St-Onge, *Critical evaluation of gated CCD detectors for laser-induced breakdown spectroscopy analysis.* Spectrochimica Acta Part B, 2005. **60**: p. 1211-1216.

[77] A.L. Edwards, *An Introduction to Linear Regression and Correlation*. 2nd ed. A series of books in psychology, ed. R.C. Atkinson, G. Lindzey and R.F. Thompson. 1984.

[78] J.L. Rodgers and W.A. Nicewander, *Thirteen Ways to Look at the Correlation Coefficient.* The American Statistican, 1988. **42**(1): p. 59-66.

[79] T. Tong, J. Li and J.P. Longtin, *Real-time control of ultrafast laser micromachining by laser-induced breakdown spectroscopy.* Applied Optics, 2004. **43**(9): p. 1971-1980.

[80] B.C. Castle, K. Talabardon, B.W. Smith and J.D. Winefordner, *Variables Influencing the Precision of Laser-Induced Breakdown Spectroscopy Measurements.* Applied Spectroscopy, 1998. **52**(5): p. 649-657.

[81] B.C. Castle, K. Visser, B.W. Smith and J.D. Winefordner, *Spatial and Temporal Dependence of Lead Emission in Laser-Induced Breakdown Spectroscopy.* Applied Spectroscopy, 1997. **51**: p. 1017-1024.

[82] R.A. Multari and D.A. Cremers, *A Time-Resolved Imaging Study of Cr (I) Emissions from a Laser Plasma Formed on a Sample at Nonnormal Incidence.* IEEE Transactions on Plasma Science, 1996. **24**(1): p. 39-40.

[83] N.L. Johnson, S. Kotz and N. Balakrishnan, *Continuous univariate distributions*. 2nd ed. Wiley series in probability and mathematical statistics. Applied probability and statistics. Vol. 2. 1994.

[84] A. Buijs, *Statistiek om mee te werken*. 2nd ed. 1998: EPN.

Appendix A: Influence of a linear variation on the linear correlation coefficient

One advantage of the linear correlation coefficient is its resistance for a linear variation. With other words, the linear correlation coefficient is not sensitive for a multiplication of all x_i-values with a constant factor α or adding a constant A to all x_i-values, $\left(X_i = \alpha \cdot x_i + A\right)$. This means that an offset (A) or an increasing of the intensity of all pixels with a factor (α) will not influence the correlation coefficient r.

In this appendix a mathematical proof will be given for the above described statement. Therefore the influence of a linear variation on the mean $\left(\overline{x}\right)$, variance $\left(s^2\right)$ and standard deviation $\left(s\right)$ will be presented first.

Influence of *A* on the mean, variance and standard deviation

Adding a constant A to all x_i-values will change the x-set in:
$x_1+A,\ x_2+A,\ \ldots.,x_m+A$

Mean:

$$\overline{X} = \frac{\sum_{i=1}^{m}\left(x_i + A\right)}{m} = \frac{x_1+A + x_2 + A + \ldots. + x_m + A}{m} = \frac{\sum_{i=1}^{m} x_i + m \cdot A}{m} = \overline{x} + A$$

$\overline{X} = \overline{x} + A$, the mean also increases with A when adding the constant A to all x_i-values.

Variance / standard deviation:

$$S^2 = \frac{\sum_{i=1}^{m}\left(x_i + A - \left(\bar{x} + A\right)\right)^2}{m-1} = \frac{\sum_{i=1}^{m}\left(x_i - \bar{x}\right)^2}{m-1} = s^2$$

$S^2 = s^2$, adding a constant A to all x_i-values has no influence on the variance and the standard deviation.

Influence of α on the mean, variance and standard deviation

Multiplication of all x_i-values with the constant α results in the new x-set:

$\alpha x_1,\ \alpha x_2,\ \ldots,\alpha x_m$

Mean:

$$\bar{X} = \frac{\sum_{i=1}^{m}\left(\alpha \cdot x_i\right)}{m} = \frac{\alpha \cdot x_1 + \alpha \cdot x_2 + \ldots + \alpha \cdot x_m}{m} = \frac{\alpha \cdot \sum_{i=1}^{m} x_i}{m} = \alpha \cdot \bar{x}$$

$\bar{X} = \alpha \cdot \bar{x}$, multiplication of all x_i-values with the constant factor α results in an increase of the mean with the same factor.

Variance / standard deviation:

$$S^2 = \frac{\sum_{i=1}^{m}\left(\alpha \cdot x_i - \alpha \cdot \bar{x}\right)^2}{m-1} = \frac{\sum_{i=1}^{m}\alpha^2\left(x_i - \bar{x}\right)^2}{m-1}\alpha^2 \cdot s^2$$

$S^2 = \alpha^2 \cdot s^2$, $S = \sqrt{\alpha^2 \cdot s^2} = \left|\alpha\right| \cdot s$, multiplication of all x_i-values with the constant factor α results in an increase of the variance with a factor α^2 and an increase of the standard deviation with the factor $\left|\alpha\right|$.

Influence of *A* on the linear correlation coefficient

$$R = \frac{\sum_{i=1}^{m}\left(x_i + A - \bar{x} + A\right)\left(y_i - \bar{y}\right)}{\sqrt{\sum_{i=1}^{m}\left(x_i + A - \bar{x} + A\right)^2}\sqrt{\sum_{i=1}^{m}\left(y_i - \bar{y}\right)^2}} = \frac{\sum_{i=1}^{m}\left(x_i + \cancel{A} - \bar{x} + \cancel{A}\right)\left(y_i - \bar{y}\right)}{\sqrt{\sum_{i=1}^{m}\left(x_i + \cancel{A} - \bar{x} + \cancel{A}\right)^2}\sqrt{\sum_{i=1}^{m}\left(y_i - \bar{y}\right)^2}} = r$$

$R = r$, the linear correlation coefficient is not sensitive for adding a constant A to all x_i-values.

Influence of α on the linear correlation coefficient

$$R = \frac{\sum_{i=1}^{m}\left(\alpha \cdot x_i - \alpha \cdot \bar{x}\right)\left(y_i - \bar{y}\right)}{\sqrt{\sum_{i=1}^{m}\left(\alpha \cdot x_i - \alpha \cdot \bar{x}\right)^2}\sqrt{\sum_{i=1}^{m}\left(y_i - \bar{y}\right)^2}} = \frac{\sum_{i=1}^{m}\cancel{\alpha} \cdot \left(x_i - \bar{x}\right)\left(y_i - \bar{y}\right)}{\cancel{\alpha}\sqrt{\sum_{i=1}^{m}\left(x_i - \bar{x}\right)^2}\sqrt{\sum_{i=1}^{m}\left(y_i - \bar{y}\right)^2}} = r$$

$R = r$, the linear correlation coefficient is not sensitive for a multiplication of all x_i-values with a constant factor α.

Appendix B: Refraction indexes and focal lengths

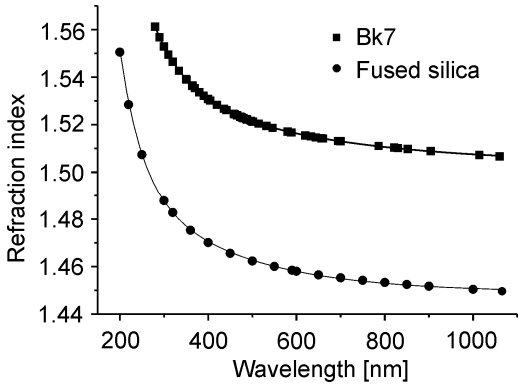

Fig. B.1 Refraction index BK7 and Fused silica versus wavelength. The values are obtained from datasheets of Heraeus and Melles Griot. Both fitted lines are of the type; second order exponential decay.

The wavelength dependent focal length of a lens in air can be calculated with the well known equation:

$$\frac{1}{f(\lambda)} = \left(n(\lambda) - 1\right)\left(\frac{1}{R_1} - \frac{1}{R_2}\right) \tag{B.1}$$

where n is de wavelength dependent refraction index of the lens, R_1 the first radius of the lens and R_2 the second radius of the lens (form left to right).

Projection lens excimer laser (fused silica, R_1 = 61.34 mm, R_2 = ∞)

λ [nm]	n	f [mm]
248	1.5082	120.7
300	1.4875	125.8
400	1.4704	130.4
500	1.4626	132.6
700	1.4550	134.8
900	1.4518	135.8

Negative lens Nd:YAG laser (BK7, R_1 = -51.2 mm, R_2 = ∞)

λ [nm]	n	f [mm]
300	1.5529	-92.6
400	1.5308	-96.5
500	1.5214	-98.2
700	1.5131	-99.8
900	1.509	-100.6
1064	1.5067	-101.0

Positive lens Nd:YAG laser (fused silica, R_1 = 46 mm, R_2 = ∞)

λ [nm]	n	f [mm]
300	1.4875	94.4
400	1.4704	97.8
500	1.4626	99.4
700	1.4550	101.1
900	1.4518	101.8
1064	1.4496	102.3

Summary

In this thesis a system has been developed to prevent polluted artworks for over-cleaning during laser cleaning. One method to monitor the laser cleaning process in-situ is spectroscopic analyzing of the in-process induced plasma emission. The characteristic plasma emission spectrum depends on the elemental constitution of the plasma plume which represents the ablated layer. In this thesis a (low cost) fibre optic spectrometer with a large bandwidth and low resolution was applied. This spectrometer is easy to handle and applicable to different polluted artworks. The advantage of the developed system is that it can be operated by restorers without much previous knowledge about plasma spectroscopy.

By correlating the current spectrum with a pre-stored reference spectrum the current ablated layer could be identified in-process. Online monitoring of the cleaning process was enabled by permanent calculating of the linear correlation coefficient. This method was successfully implemented into a KrF-excimer laser system with translation stage and into a Nd:YAG cleaning laser system with an articulated mirror arm.

In case of closed loop laser cleaning the ablation process continued until the correlation coefficient exceeded a pre-defined value, subsequently the ablation process was automatically stopped and resumed on a new position by translating the sample automatically. In the event of cleaning with manual articulated beam delivery the obtained correlation coefficients can be used to support a human decision. Therefore, a webcam was positioned above the sample to ascertain the irradiation position by image processing. On a screen a

current picture of the sample was visible with color marks on the irradiated positions. These color marks represented the progress of the cleaning.

The experiments on multiple (artificial) artwork samples have shown that laser cleaning processes can be monitored or controlled by low resolution plasma spectroscopy based on linear correlation analysis, on condition that there is plasma emission and the spectra of the different layers vary. The best visual results were obtained with samples with a macroscopic-granular pollution structure.

Samenvatting

In dit proefschrift is een systeem ontwikkeld om over-reiniging tijdens het laser reinigen van vervuilde kunstwerken te voorkomen. Een methode om tijdens het laser reinigen het proces te observeren is het spectroscopisch analyseren van tijdens het proces geïnduceerde plasma straling. Het karakteristieke plasma emissie spectrum is afhankelijk van de elementaire samenstelling van het plasma en deze representeert wederom de samenstelling van de verwijderde laag. In dit onderzoek is een robuuste (low cost) optische fiber spectrometer met een grote bandbreedte en lage resolutie toegepast. Deze spectrometer is gemakkelijk te bedienen en kan worden toegepast voor verschillende vervuilde kunstwerken. Het voordeel van het ontwikkelde systeem is dat het bediend kan worden door restauratoren met weinig voorkennis over plasma spectroscopie.

Door het actuele spectrum te correleren met een van te voren opgenomen referentie spectrum kan de actueel verwijderde laag tijdens het proces worden geïdentificeerd. Het bewaken van het reinigingsproces is gebaseerd op het permanent berekenen van de lineaire correlatie coëfficiënt. Deze methode is met succes geïmplementeerd in een KrF-excimer laser systeem met x-y tafel en in een Nd:YAG reinigingslaser met beweegbare spiegelarm.

Bij het reinigen met de gesloten regelkring ging het reinigingsproces door totdat de correlatie coëfficiënt een van te voren vastgelegde waarde overschreed. Daarna is het proces automatisch gestopt en hervat op een nieuwe positie door het object automatisch te verplaatsen. In het geval van het reinigen met een beweegbare spiegelarm kunnen de verkregen correlatie coëfficiënten worden gebruikt om een menselijke beslissing te ondersteunen.

Om dit te realiseren is een webcam boven het te behandelen object geplaatst waarmee door middel van image processing de bestraalde positie kon worden bepaald. Op een monitor was een actuele foto van het object zichtbaar met op de bestraalde posities een kleurwaarde. De kleur representeerde de staat van de reiniging.

De experimenten op verschillende (artificiële) kunstwerken hebben laten zien dat laser reinigingsprocessen kunnen worden gecontroleerd door middel van lage resolutie plasma spectroscopie gebaseerd op lineaire correlatie analyse, op de voorwaarde dat er plasma emissie is en de spectra van de verschillende lagen zich onderscheiden. De beste visuele resultaten zijn verkregen op samples met een korrelige vervuiling.

Acknowledgment

For me the time in Münster and at the Laser Center of the Münster University of Applied Sciences was full of educational and social experiences. During this time I have met a lot of different people, had to speak and write three different languages, worked with high-end equipment, had nice working colleagues and…. By this means, I want to thank everybody who helped me with the realization of this thesis. Some of them I would like to thank by name.

First of all I want to thank Prof. dr. Dickmann and Prof. dr. Meijer who made it possible for me to do a doctorate by collaboration between the Laser Center of the Münster University of Applied Sciences, the Laboratory of Applied Laser Technology of the University of Twente and the Dutch research school IPV. They advised and supported me during my research activities, by writing scientific publications and by finishing this thesis.

I want to thank my direct colleagues Marc Baumeister, Elke Engelhardt, Jürgen Gröninger and Jens Hildenhagen for creating a nice working atmosphere, especially Jens who had to sit more than five years with me in one office. Special thanks to Petra Welp for the technical discussions and for proofreading this thesis. I also would like to thank my friend Marcel v. Mil for proofreading and the students Dolf Klomp, Carmen Panneman and Bart Sasbrink who helped me with their practical work to realize this project.

Last but not least I want to thank my lovely Kerstin and my family for supporting and motivating me.

Marco Lentjes, December 2007

About the author

Marco Lentjes was born on March 24th, 1979 in Schiedam, the Netherlands. He finished his Lower General Secondary Education (MAVO) in 1995. From 1995 till 1998 he studied electrical engineering with the major electronics at the Albeda College in Schiedam, Polytechnic School (MTS). After graduation he studied Engineering Physics at the Rijswijk University of Professional Technical Education from 1998 till 2002. In 2002 he graduated with a specialization in photonics. His thesis title was: "Low cost sensor system for online plasma monitoring during laser cleaning". From 2002 till 2007 he worked full-time as a scientific engineer at the Laser Center of the Münster University of Applied sciences. In 2003 he started as an extern PhD-student of the Laboratory of Mechanical Automation and Mechatronics (WA) which is a section of the faculty Engineering Technology (CTW) of the University of Twente. From 2003 till 2007 he was also a member of the Dutch research school of Integrated Manufacturing (IPV).

During his time as a scientific engineer at the Laser Center he worked not only at the subjects described in this thesis but also on: laser micro material processing with excimer laser, laser marking, laser cleaning of stamp ink from real artworks on paper, laser cutting of sapphire and laser inside marking of transparent materials.

List of publications

- M. Lentjes, K. Dickmann, P. v. Dalen, *Laser Reduction of stamps from paper to avoid migration to the recto side, case study based on illustrations from Jan Heesters (NL)*, Lasers in the Conservation of Artworks, Proc. LACONA VII, 17-21 September 2007, In Process

- J. Hildenhagen, M. Lentjes, K. Dickmann, B. Geller, *Systematic case study on common cleaning problems on paper and parchment by using Nd:YAG-Laser (ω, 2ω, 3ω)*, Lasers in the Conservation of Artworks, Proc. LACONA VII, 17-21 September 2007, In Process

- M. Lentjes, J. Hildenhagen, K.Dickmann, *Laser ablation- and LIBS-ranging by webcam and image processing during laser cleaning*, Lasers in the Conservation of Artworks, Proc. LACONA VII, 17-21 September 2007, In Process

- M. Lentjes, M. de Block, P. v. Dalen, K. Dickmann, *Stempels verwijderen van papieren draggers m.b.v. laserstraling ter voorkoming van migratie naar de recto zijde,* Cr; interdisciplinair tijdschrift voor conservering en restauratie, 2007, No. 4, In Press

- M. Lentjes, M. de Block, P. v. Dalen, K. Dickmann, *Reduzierung von Stempeltinte auf Papierträger mittels Laserstrahlung*, Restauro, 2007, No. 8, In Press

- M. Lentjes, K.Dickmann, J. Meijer, *Low Resolution LIBS for Online-Monitoring During Laser Cleaning Based on Correlation with Reference Spectra*, Lasers in the Conservation of Artworks, Springer Proceedings in Physics Vol. 116, Proc. LACONA VI, Ed. by: J. Nimmrichter, W. Kautek, M. Schreiner, 2007, pp. 437, ISBN: 978-3-540-72129-1

- M. Lentjes, K.Dickmann, J. Meijer, *Influence of process parameters on the distribution of single shot correlation coefficients obtained by correlating LIB-Spectra*, Applied Physics A, 2007, Vol. 88, pp. 661-666

- M. Lentjes, K. Dickmann, J. Meijer, *Calculation and optimization of sample identification by laser induced breakdown spectroscopy via correlation analysis*, Spectrochimica Acta Part B, Vol. 62, 2007, pp 56-62

- M. Lentjes, K. Dickmann, J. Meijer, *Kontrollierter Mikroabtrag an Schichtsystemen mittels Laserstrahlung und online Plasma Spektroskopie (LIPS)*, Journal of the University of Applied Sciences Mittweida, No. 5, 2006, pp. 87-91

- M. Lentjes, K. Dickmann, J. Meijer, *Controlled Laser Cleaning of Artworks via Low Resolution LIBS and Linear Correlation Analysis*, ICALEO 2005 Congress Proceedings, Laser Microfabrication Conference, CD-ROM Paper #M603, pp. 286-292

- K. Dickmann, M. Lentjes, J. Meijer, *Online diagnostics for laser cleaning of artworks*, Europhysics Conference Abstracts Volume 29B, 2005, CD-ROM, CSI-4-THU

- D. Knapp, M. Lentjes K. Dickmann, H. Dyck, N. Munser, *Herstellung von Freiformflächen aus transparenten Materialien mit Nd:YAG-Laserstrahlung*, Laser Magazin, No. 6, 2005, pp. 7-10

- M. Lentjes, K. Dickmann, J. Meijer, *Prozesskontrolle bei der Laserreinigung durch Plasmaanalyse mittels niedrig auflösendem Spektrometer*, Photonik, No. 3, 2005, pp. 84-87

- M. Lentjes, K. Dickmann, J. Meijer, *Prozessüberwachung beim Laserreinigen und Laserschichtabtrag durch Anwendung der Plasmaanalyse mittels "low resolution" Spektrometer*, Aktuelle Methoden der Laser- und Medizinphysik, Proc. 2. Remagener Physiktage 2004, Ed. by: U. Hartmann, M. Kohl-Bareis, P. Hering, G. Lonsdale, J. Bongartz, T.M. Buzug, 2005, pp. 288-293, ISBN: 3-8007-2838-9

- M. Lentjes, D. Klomp, K.Dickmann, *Sensor concept for controlled laser cleaning via photodiode*, Lasers in the Conservation of Artworks, Springer Proceedings in Physics Vol. 100, Proc. LACONA V, Ed. by: K. Dickmann, C. Fotakis, J.F. Asmus, 2005, pp. 427-433, ISBN: 3-540-22996-5

- M. Lentjes, K. Dickmann, J. Meijer, *Controlled laser cleaning and ablation by laser induced plasma emission analysis via miniature spectrometer*, Laser Assisted Net Shape Engineering 4, Proc. of the LANE 2004, Ed. by: M. Geiger, A. Otto, Vol. 2, 2004, pp 803-810, ISBN: 3-87525-202-0

- H. Dyck, N. Munser, M. Lentjes, K. Dickmann, *Laser-Präzisionsbearbeitung von Saphir,* Laser Technik Journal, No. 1, 2004, pp. 21-22

- M. Lentjes, K. Dickmann, *Sensor-System für Echtzeitkontrolle bei der Laserreinigung*, Journal of the University of Applied Sciences Mittweida, No. 1, 2003, pp. 68-71

- M. Lentjes, K. Dickmann, H. Dyck, N. Munser, *Laser-Präzisionsbearbeitung von Saphir für medizintechnische Anwendungen*, Journal of the University of Applied Sciences Mittweida, No. 1, 2003, pp. 113-116

- M. Lentjes, D. Klomp, K.Dickmann, *Sensor concept for controlled laser cleaning via photodiode*, abstract book LACONA V, 5th International Conference on Lasers in the Conservation of Artworks, Osnabrück, Germany, September 15-18, 2003, pp. 193-195